A Nanoscale Probe of the Quasiparticle Band Structure
for Two Dimensional Electron Systems

by

Anjan Soumyanarayanan

Submitted to the Department of Physics
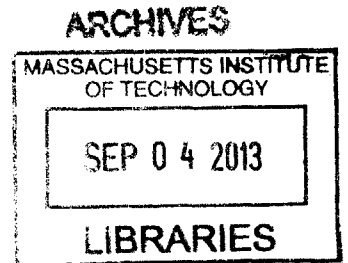in partial fulfillment of the requirements for the degree of
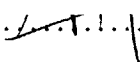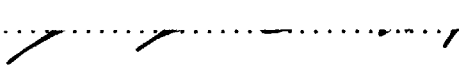
Doctor of Philosophy
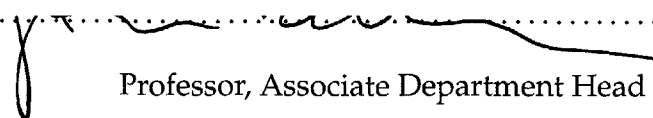
at the

MASSACHUSETTS INSTITUTE OF TECHNOLOGY

June 2013

Author . . . .
Department of Physics
May 24, 2013

Certified by . . . .
Jennifer E. Hoffman
Associate Professor
Thesis Supervisor

Certified by . . . .
Young S. Lee
Professor
Thesis Supervisor

Accepted by . . . .
John Belcher
Professor, Associate Department Head for Education

A Nanoscale Probe of the Quasiparticle Band Structure

for Two Dimensional Electron Systems

by

Anjan Soumyanarayanan

Abstract

The advent of a broad class of two-dimensional (2D) electronic materials has provided avenues to create and study designer electronic quantum phases. The coexistence of superconductivity, magnetism, density waves, and other ordered phases on the surfaces and interfaces of these 2D materials are governed by interactions which can be experimentally tuned with increasing precision. This motivates the need to develop spectroscopic probes that are sensitive to these tuning parameters, with the objective of studying the electronic properties and emergence of order in these materials.

In the first part of this thesis, we report on spectroscopic studies of the topological semimetal antimony (Sb). Our simultaneous observation of Landau quantization and quasiparticle interference phenomena on this material enables their quantitative reconciliation - after two decades of their study on various materials. We use these observations to establish momentum-resolved scanning tunneling microscopy (MR-STM) as a robust nanoscale band structure probe, and reconstruct the multi-component dispersion of Sb(111) surface states. We quantify surface state parameters relevant to spintronics applications, and clarify the relationship between bulk conductivity and surface state robustness. At low momentum, we find a crossover in the single particle behavior from massless Dirac to massive Rashba character – a unique signature of topological surface states.

In the second part of this thesis, we report on the spectroscopic study of charge density wave (CDW) order in the dichalcogenide $2H$-NbSe$_2$ – a model system for understanding the interplay of coexisting CDW and superconducting phases. We detail the observation of a previously unknown unidirectional (stripe) CDW smoothly interfacing with the familiar triangular CDW on this material. Our low temperature measurements rule out thermal fluctuations and point to local strain as the tuning parameter for this quantum phase transition. The distinct wavelengths and tunneling spectra of the two CDWs, in conjunction with band structure calculations, enable us to resolve two longstanding debates about the anomalous spectroscopic gap and the role of Fermi surface nesting in the CDW phase of NbSe$_2$. Our observations motivate further spectroscopic studies of the phase evolution of the CDW, and of NbSe$_2$ as a prototypical strong coupling density wave system in the vicinity of a quantum critical point.

Thesis Supervisor: Jennifer E. Hoffman
Title: Associate Professor

Thesis Supervisor: Young S. Lee
Title: Professor

Acknowledgements

Probably the biggest advantage of having access to resources at both MIT and Harvard as a graduate student has been the vast reservoir of scientific and technical expertise that I have been able to learn from and work with. It has enabled me to forge numerous collaborations and professional relationships that will undoubtedly transcend the time I have spent at these institutions.

First and foremost, I would like to express my sincere gratitude to my advisor, Prof. Jenny Hoffman. Over the past four years, Jenny has provided me with numerous opportunities that are rarely available to graduate students – writing a grant proposal, refereeing papers, forming collaborations with theorists and experimentalists, and independently taking projects from ideas to results. Jenny has patiently taught me how to look at experimental data in a critical and unbiased manner, to extract meaningful conclusions, and to convey these results to a scientific audience by constructing convincing arguments. For these opportunities and many more, I thank Jenny.

It is unlikely that I would have been unable to get here without the invaluable academic and scientific guidance offered by Prof. Eric Hudson over the past seven years. Eric has been a great mentor – as an academic advisor, a teacher, an STM expert, and an experienced collaborator. His boundless optimism and unending enthusiasm were instrumental in getting us through the tough times. Despite now being at Penn State, he has continued to be generous with his time and advice, and I look forward to continue working with him.

The experimental results detailed in this thesis have been acquired by the STM1 team over 2011-12, comprising Michael Yee, Yang He, and myself. I am grateful to Mike, who joined the team in 2010, and persevered through the experimental mishaps that plagued us for over a year. For all the hours spent in fixing the dewar, wiring the fridge, brazing, checking for leaks; and for selflessly taking charge in Fall 2011, when the STM was producing results and I had teaching commitments. And to Yang, who joined us in 2011, for bringing great enthusiasm to learn and create physics; for his uncanny ability to land on 1D structures on any material; and for teaching me much about BSCCO. To Yi Yin, Martin Zech, and Heon-Ick Ha for constructing the instrument, and to Tess Williams and Yi Yin for teaching me how to operate it. To the central machine shops at MIT and Harvard (SEAS), whose help in reviving our instrument in 2010 cannot be overstated.

On the NbSe$_2$ project, I am extremely thankful to our external collaborators, who played a vital role in developing our experimental findings into an interesting story. Particularly to Jasper van Wezel for working tirelessly on the project, for his patience with theoretical avenues that didn't immediately yield results, and for being readily available to discuss physics outside the project. To Dr. Mike Norman for patiently guiding the project towards completion, and for anticipating the dead ends, all despite his busy schedule. And to Dr. Kai Rossnagel, for his insightful realization of the correspondence between STM and ARPES data. On the antimony project, I am thankful to Hsin Lin, who made vital contributions to formulating the story with his insightful realizations. To Dillon Gardner and Prof. Young Lee, for their continued patience in working with us despite the down time of our instrument, and for providing truly unique samples. I would like to acknowledge useful discussions with several others that helped shape our scientific ideas: Profs.

Patrick Lee and Steve Kivelson for NbSe$_2$, and Profs. Liang Fu, Joel Moore, and Vidya Madhavan for antimony. In addition, several theorists at Harvard – Jay Sau, Anton Akhmerov, Prof. Bert Halperin, and Dr. Emmanuel Rashba, have contributed to the interpretation of these results.

MIT has an outstanding tradition in graduate physics education, and I am fortunate to have benefited tremendously from this. I am grateful in particular to Prof. Patrick Lee, who has taught me much of what I know about condensed matter physics. Prof. Lee's patience with my incessant questions throughout the two-term sequence, his insights in simplifying seemingly complex phenomena, and interest in discussing and interpreting our experimental findings – has been a vital part of my graduate education. To Wing-Ho Ko, who, as a teacher, endured me for over three terms, and offered new and accessible perspectives on condensed matter problems. To Prof. Mehran Kardar, whose two-term sequence on statistical mechanics delivered with an inimitable style was a treat, even for an experimentalist. To Profs. Young Lee, my co-advisor, and Pablo Jarillo-Herrero, my academic advisor, who took an active interest in my education and academic progress and were generous with their time; and to Prof. Nuh Gedik, who graciously served on my thesis committee.

Pursuing a successful PhD in condensed matter experiment is contingent on developing the requisite laboratory skills in design, construction and debugging. I am grateful to have worked with several experienced experimentalists who have contributed greatly to my technical education. To Oliver Dial, Eric Lin, and Lu Li, for helping me find my feet as a low temperature experimentalist. To Prof. Paul Horowitz, Tom Hayes, and Jim Macarthur, for teaching me the elements of good circuit design. To Stan Cotreau and Mark Belanger, for teaching me valuable machining, brazing and mechanical design skills.

The Hoffman Lab has provided a great atmosphere to learn the science and art of STM. In particular, I am grateful to Ilija Zeljkovic for generously sharing his experience with fixing tips, analyzing data, and most importantly for teaching me the distinction between perfection and practicality in experimental physics. To Tess Williams, Elizabeth Main, Adam Pivonka, and Jeehoon Kim for their generous help and advice during the repair and refurbishment of our instrument. To Nick Litombe, for his enthusiasm to learn and discuss physics; to Can-Li Song for his encyclopedic knowledge of topological insulators; and to Dennis Huang and Cun Ye for putting up with my physics (and non-physics) monologues. Outside the lab, I am also grateful to Hadar Steinberg, Justin Song, and Jayson Paulose for insightful physics conversations.

Finally, on a personal note, I would like to express my sincere gratitude to my immediate and extended family. In particular, to my parents and my sister, for their unwavering support and encouragement through all these years, and to my wife Pavitra, for her steadfast patience and understanding through the highs and lows of our graduate education.

Thank you all.

Contents

9

List of Figures

12

List of Tables

Chapter 1

Two Dimensional Electronic Materials

In our everyday life, we see various manifestations of phase transitions. The condensation of water vapor into water and the freezing of water to ice are examples of structural phase transitions. Loosely speaking, condensed matter physics involves the study of phase transitions and understanding 'interesting' phases of matter.

The basic properties of electronic systems can be understood using an analogous picture of electronic phases. In 1900, it was demonstrated that at room temperature, the behavior of electrons in a metal can be described rather well by considering it to be an 'ideal gas' - a collection of classical charged particles[1]. As the metal is cooled, the electrons start to interact, and this description breaks down. However, Landau's insightful Fermi liquid theory showed that even in the presence of interactions, the low energy properties of the system could be understood within a noninteracting picture by defining the concept of a *quasiparticle*[2].

When a system of electrons is examined in isolation from its environment, the novelty in electronic properties and diversity in ordered states is limited. However, the rich physics of electronic phases that are studied today unfold from the interaction of the electrons with the underlying crystal lattice. Notably, the last decade has witnessed the emergence of several classes of two-dimensional electronic materials, which display unusual electronic properties and provide much promise towards the creation of designer electronic phases. This chapter describes some of the properties encompassing these diverse set of materials, and examines the pros and cons of conventional electronic probes in studying them.

1.1 The Advent of 2D Electronic Materials

Over the past few years, several materials that exhibit two dimensional electronic properties have been realized. The 2D electron systems in these materials are either formed at the interface or surface of 3D materials, as in the case of oxide interfaces and various topological materials; or are
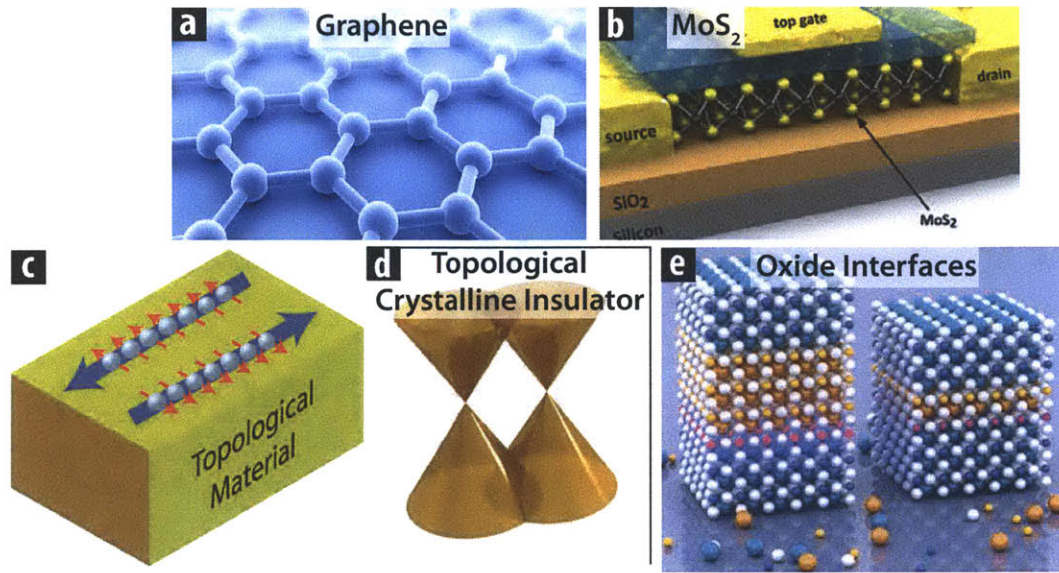
Figure 1-1: Examples of 2D Electronic Materials. (a) The honeycomb atomic lattice of graphene, which gives rise to its remarkable Dirac fermion properties (© BBC). **(b)** A field-effect transistor device made out of thin flakes of the transition metal dichalcogenide MoS_2 (© Nature Nanotechnology). **(c)** A schematic representation of counterpropagating spin-polarized surface states on a topological insulator. **(d)** The double Dirac cone band structure of a typical topological crystalline insulator (© Osaka University). **(e)** A schematic depiction of the crystal structure of transition metal oxide heterostructures, with metallic 2D systems at their interfaces (© Science Magazine).

thin systems, e.g. graphene, silicene, and transition metal dichalcogenides; or epitaxially grown thin film materials. Several of these systems display great promise towards realizing novel physics and applications - with high mobility, tunable carrier density and ambipolar transport properties.

A defining characteristic of several of these materials is the influence of the crystalline lattice in determining the electronic properties. This leads to marked changes in the energy-momentum relationship, or band structure, of the electronic quasiparticles, and in some cases, to the emergence of ordered phases.

The most fundamental way in which a lattice interacts with the electron system is through the introduction of translational and rotational symmetries. This can have a marked effect on the band structure of the electron system, giving rise to fundamentally new kinds of physics. For example, the honeycomb lattice structure of graphene (Fig. 1-1a) directly leads to its remarkable Dirac fermion-like properties[3], and the crystalline mirror symmetry in rock salt structures leads to the presence of robust surface states in topological crystalline insulators (Fig. 1-1d)[4]. Another way in which the lattice can markedly influence electronic properties is through the intrinsic properties of the lattice ions. If the ions have a static magnetic moment, this can lead to ordered magnetic phases. The symmetry, size and extent of atomic orbitals of the lattice ions can also lead to a crossover between itinerant and local physics, as in the case of several correlated materials.
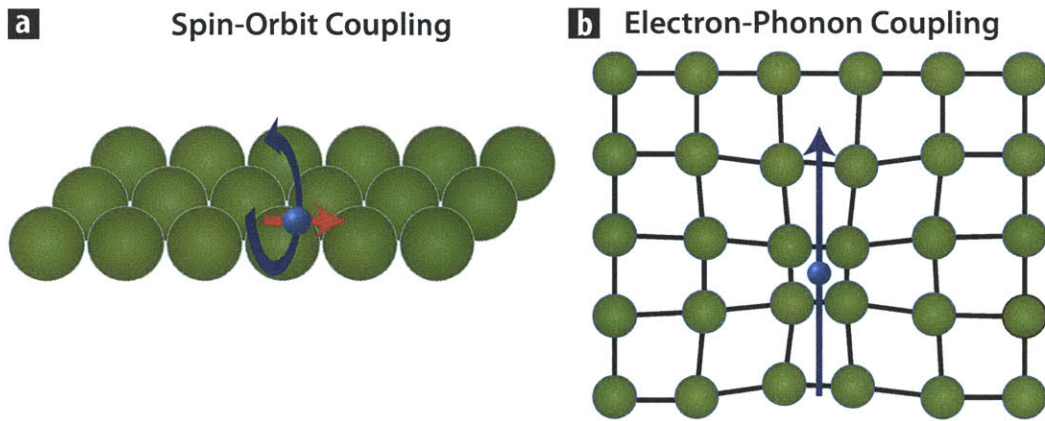
Figure 1-2: Cartoon Representation of Spin-Orbit Coupling and Electron-Phonon Coupling Effects. (a) A schematic depiction of the interaction between spin and orbital degrees of freedom of an electron in a crystalline lattice with heavy atoms, known as spin-orbit coupling. **(b)** Schematic depiction of the interaction between a traveling electron and vibrations of ions in the crystal, known as electron-phonon coupling.

The effects of the lattice on the electron systems examined in this thesis are in a different category from the above, and involve dynamic interactions.

In crystalline lattices with heavy ions, the electric field experienced by a traveling electron translates to a magnetic field proportional to its velocity in the rest frame of the electron. The dipolar interaction of the electron spin with this effective magnetic field is therefore equivalent to the coupling of the electronic spin and orbital degrees of freedom (Fig. 1-2a), known as spin-orbit coupling (SOC)[5]. SOC can split the degeneracy of electronic bands with finite angular momentum (p, d, f-bands, e.g. Fig. 3-3a), modifying the band structure of several semiconducting materials. If the SOC is strong enough, the induced splitting can be so large as to invert the electronic band structure, leading to the existence of topologically ordered phases. The surface states arising from such a topological phase are examined in the first part of this thesis.

Electrons traveling through a crystalline lattice can also interact with the vibrations of the lattice ions, known as phonons, as shown in Fig. 1-2b. This electron-phonon coupling (EPC) can renormalize the electronic band structure[1], and is sensitive to substrate properties in several 2D materials[6]. At low temperatures, sufficiently strong EPC can lead to the formation of ordered phases such as superconductors and density waves. The latter is the topic of the second part of this thesis.

1.2 Tunability of 2D Materials

The excitement surrounding the realization of several classes of 2D electronic materials is, to a great extent, due to the degree of control one has in determining the properties of the system. Various parameters of 2D systems that are realized through epitaxial growth or mechanical exfo-

liation can be tuned, enabling controlled and reversible access to diverse set of quantum phases. Importantly, these properties can be modified after the growth process, offering the experimenter unprecedented control over the system of interest. Here we outline some of the experimental tools which enable the tuning of the electronic properties of these materials.

1.2.1 Electric Field Effect
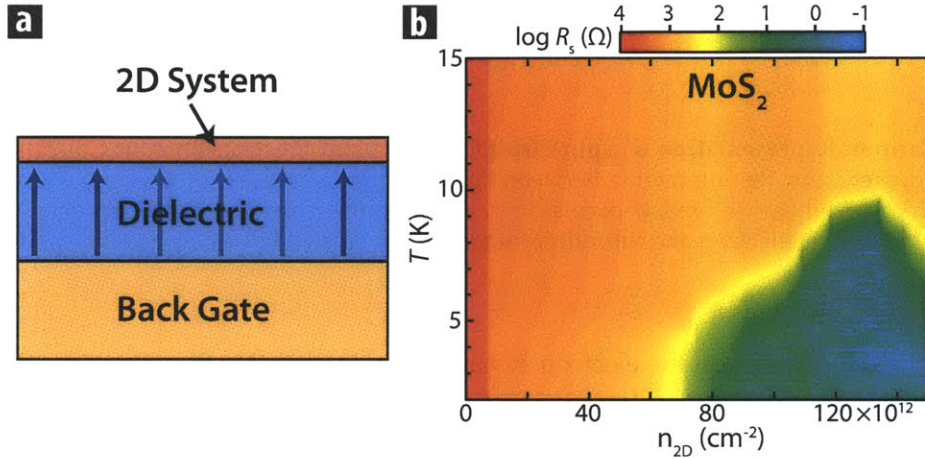
Figure 1-3: Electric Field Effect Tuning of Electron Density. (a) A schematic representation of electric field effect control of electron density. A metallic electrode gate, used to apply the electric field, is separated from the 2D system by a dielectric spacer. **(b)** A resistance color plot on MoS_2 as a function of carrier density (controlled by electric field effect) and temperature, showing a quantum phase transition from a band insulator at low density to a dome-shaped superconductor at high densities (adapted from [7]).

It has been known for some time that the application of an electric field through capacitive techniques can be used to control the electron density in a 2D system, and this forms the basis of the MOSFET technology used in modern transistors[8]. Typically, the 2D system of interest is placed on a dielectric material, which lies on a metallic electrode, known as the gate, as shown in Fig. 1-3a. When a voltage is applied on the gate electrode relative to the 2D system, capacitive effects cause a change in the electron density of the 2D system. In a so called field-effect transistor, one can deplete and enhance the carrier density by varying the gate voltage, and therefore tune the 2D system through insulating and conducting behaviors[8]. While in principle doping the system with charge carriers could be used to control the carrier density, this has the undesirable effect of also introducing disorder. Therefore, gating is viewed as a cleaner tuning parameter for this purpose.

Recent advancements in materials chemistry, synthesis, and fabrication techniques have tremendously increased the available range of electron densities within a single sample[9]. Several clean 2D systems now exist that can be gate-tuned to produce ambipolar transport[10–12]. The development of new dielectrics such as HfO_2 and $SrTiO_3$ with high breakdown voltages has enabled the application of large electric fields, offering greater control over the carrier density[9, 11]. Further-

more, the recent emergence of electrochemical gating as a means to vary electron densities over 2-3 orders of magnitude has generated much excitement[13]. These advancements have enabled the tuning of several 2D systems through quantum phase transitions from insulating to superconducting behavior, as shown in Fig. 1-3b for MoS_2[7].

1.2.2 Strain
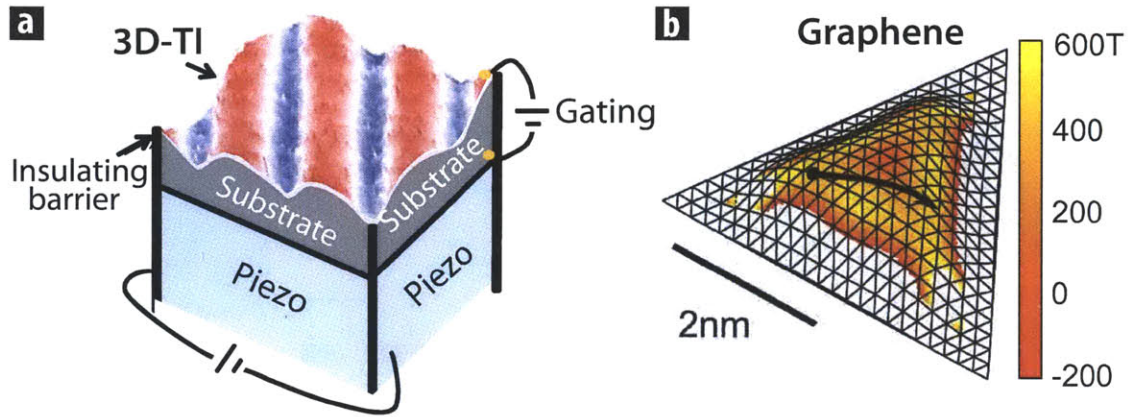
Figure 1-4: Nanoscale Strain Induced Electric and Magnetic Fields. (a) The observation of smooth modulations in chemical potential induced by surface rippling of the topological insulator Bi_2Te_3 by Okada *et. al.* has led to proposals of controlled straining of these materials using piezoelectric devices (adapted from [14]). **(b)** The observed modification of the electronic properties of graphene by substrate-induced strain, corresponding to the existence of pseudo-magnetic fields above 300 T (adapted from [15]).

The introduction of strain has emerged as a novel route towards the engineering of electronic properties of several 2D materials[16]. Strain can be introduced in these materials by changing (or removing) the substrate that the material is grown or placed on, by introducing adatoms on the substrate surface, or by using piezoelectric devices to control the substrate.

Strain can modify the phononic properties of the lattice, and can also tune the strength of electron-phonon coupling. This can lead to a change in electronic dispersion[6] or introduce a band gap[17]. We will show later on that the interplay of strain and electron-phonon coupling can have remarkable consequences on density wave order in the strong coupling limit[18].

Other remarkable effects of strain have been observed in recent years that have led to increased efforts towards strain engineering. For example, Okada *et. al.* found that surface rippling on the topological insulator Bi_2Te_3 introduces a smooth spatial modulation of the chemical potential(Fig. 1-4b), which likely arises from strain-induced electric fields[14]. The electric field effect produced by moderate amounts of strain was found to be an order of magnitude larger than the corresponding effects of spatially modulated doping[14]. Meanwhile, Levy *et. al.*, in their studies of graphene grown on Pt(111) substrate reported the formation of 'bubbles' on the nanometer lengthscale[15]. In these highly strained regions, they noted a substantial modification of elec-

tronic behavior, corresponding to the existence of magnetic fields up to several hundred Tesla (Fig. 1-4b) - an order of magnitude above the highest achievable magnetic fields in a laboratory setting. The observation of these strain-induced electric and magnetic fields therefore have generated several proposals for controlled strain modification of these materials, using, for example, piezoelectric devices[14].

1.2.3   Doping, Inhomogeneity and Coexisting Orders
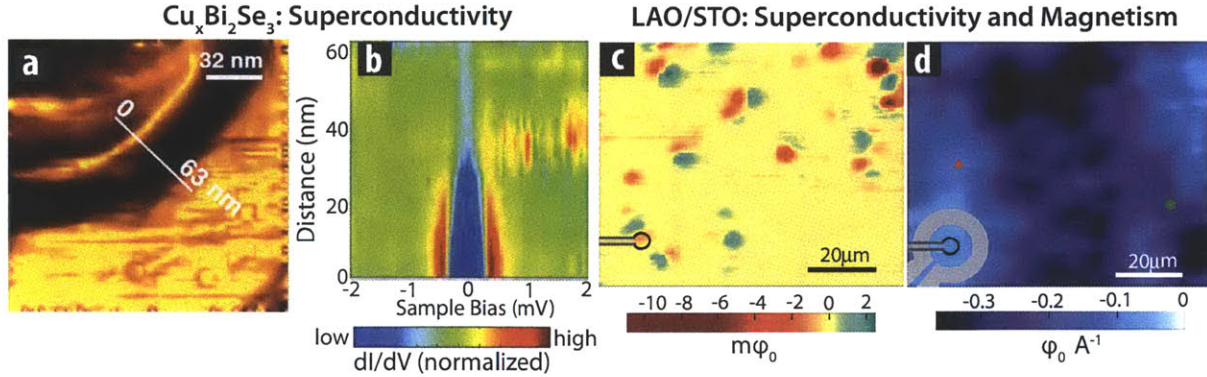
Figure 1-5: Nanoscale Variation and Spatial Coexistence of Ordered Phases. (a-b) STM studies of the superconducting order parameter in the doped topological insulator $Cu_xBi_2Se_3$ (adapted from [19]). The spectroscopic linecut in (b), taken along the white line in the topograph (a), shows marked variation in the superconducting gap. **(c-d)** Scanning SQUID mapping of coexisting ferromagnetic and superconducting orders at the LAO/STO interface (adapted from [20]). (c) shows a SQUID magnetometry image, with spatial variations indicative of ferromagnetic order. (d) shows a SQUID susceptometry image, mapping the superfluid density with position.

The properties of several of these 2D materials are inhomogeneous on the nanoscale. For example, it has been shown in single-layer graphene that the chemical potential[21] and the Fermi velocity[22] vary on the nanoscale due to disorder effects, and similar reports have emerged from studies of Bismuth-based topological insulators[23].

More remarkably, electronic order also shows nanoscale variations in these materials. In the doped topological insulator $Cu_xBi_2Se_3$, which undergoes a superconducting transition at ~ 3.7 K[24], the superconducting order parameter shows marked spatial variations (Fig. 1-5a-b), likely due to local variations in the doping[19]. In the heterostructure interface system LAO/STO, superconducting and ferromagnetic orders are reported to coexist on the nanoscale (Fig. 1-5c-d, [20]). The ability to grow several of these materials epitaxially, and to systematically introduce dopants offers promising routes to generate and study the interplay of various quantum phases.

1.3   Conventional Band Structure Probes

The existence of several tuning parameters to control the properties of these 2D materials therefore motivates the utility of tools that can utilize this large parameter space, measure the electronic

properties, and detect the emergence of ordered phases in these materials. Here we briefly examine the pros and cons of the most commonly used band structure probes in the context of studying these 2D materials.

1.3.1 Quantum Oscillations

The detection of oscillations in transport and thermodynamic properties as a function of applied magnetic field is the oldest and most established technique of measuring the Fermi surface of electronic systems[25]. As detailed in § 2.3.1, an external magnetic field quantizes the electronic band structure into Landau levels (LLs), and the Fermi energy, ε_F can be tuned through LL maxima and minima by varying the magnetic field (or the carrier density). The resulting modulation in the density of states at ε_F manifests as oscillations in the measured transport and thermodynamic properties, e.g. electrical and thermal conductivity, susceptibility, heat capacity etc. The periodicity of the oscillations with inverse magnetic field is a direct measure of the associated closed Fermi surface contour, and the temperature dependence of the oscillation amplitude can be used to extract the quasiparticle mass.

Quantum oscillation studies and related techniques are tremendously useful in measuring the properties of the Fermi surface, and are sensitive to several of the parameters detailed in § 1.2. However, the inability to probe the physics of electronic states away from ε_F is a major limitation in understanding the properties of these materials. To gain more information about electronic states away from ε_F, we turn to spectroscopic probes.

1.3.2 Angle-Resolved Photoemission Spectroscopy

Angle-resolved photoemission spectroscopy, commonly known as ARPES, has emerged as the standard band structure probe of 2D materials in the past two decades[26]. A photon beam incident on the material of interest leads to the emission of photoelectrons from the surface, and by measuring the energy and momentum of the ejected photoelectrons, their energy and in-plane crystal momentum can be deduced, leading to a near-direct measurement of the 2D band structure, $\varepsilon(k_x, k_y)$, for filled states[27]. Steady progress in the generation of high fidelity photon beams and in the measurement of photoelectrons has enabled ARPES to achieve $\sim$ few meV energy resolution and < 0.01 Å^{-1} momentum resolution[26]. More recently, ARPES systems with a base temperature of 1 K have been constructed to study ordered phases that emerge at low temperatures.

The ability to directly measure filled state band structure makes ARPES a vital probe for studying 2D systems. However, despite its many advantages, ARPES is faced with some limitations - chiefly the inability to measure the band structure of empty states[1], a base temperature of 1 K, and

---

[1]Inverse photoemission, an ARPES-like probe designed for this purpose, has limited utility, and low energy and momentum resolution

the inability to apply magnetic field. In the context of the tunable parameters discussed in § 1.2, we note the inability to perform simultaneous ARPES measurements.

1.3.3 The Need for a Complementary Band Structure Probe

In order to fully explore the fascinating avenues created by the discovery of these myriad classes of 2D electronic materials, we need to complement existing band structure probes. For example, to study the emergence of ordered phases below 1 K in several of these materials, we need a probe that can operate at dilution fridge temperatures, with temperature-limited energy resolution. To study field-induced ordered phases, the probe should be able to measure electronic properties in the presence of a magnetic field. To study the physics of ordered states with particle-hole aysmmetry, the probe should be sensitive to empty states.

Moreover, to explore the parameter space of these 2D materials, it would be desirable to include the ability to gate-tune the carrier density, controllably strain the sample, and perform epitaxial growth and doping in conjuction with the spectroscopic measurements. Crucially, in order to study the nanoscale variation in electronic properties and ordered phases, the probe should have spatial resolution.

These requirements naturally motivate the use of spectroscopic scanning tunneling microscopy (STM) to study these materials. In the following chapter, we will examine the potential of STM towards the spectroscopic study of 2D materials and discuss the limitations it faces currently, which we will resolve in the first part of this thesis.

Chapter 2

The Scanning Tunneling Microscope: A Nanoscale Spectroscopic Probe

The scanning tunneling microscope (STM) has proved to be an incredibly useful tool to study the structural and electronic properties of condensed matter systems on the atomic scale. Here, we detail the phenomenon of quantum tunneling, the underlying principle of STM, and detail the construction and data acquisition modes of our STM instrument. We describe the origin of Landau quantization and quasiparticle interference – two phenomena that enable momentum resolution with spectroscopic STM, and highlight the quantitative limitations faced by STM currently – as a band structure probe of 2D materials.

2.1 Quantum Tunneling and the STM

The underlying principle of the scanning tunneling microscope (STM), which enables the atomically resolved study of sample surfaces, is that of quantum tunneling. In its simplest incarnation, one can think of the STM as comprising of a sharp tip, say a piece of wire with a single atom dangling at the end, held a distance z (typically a few angstroms) away from an atomically flat surface, called the sample (Fig. 2-1a). A bias voltage, V, is applied to the sample, and the current, I, is measured at the tip.

In a classical picture, no current is expected to flow between the tip and sample due to the circuit break corresponding to the nonzero tip-sample separation. However, quantum phenomena govern the physics at atomic length scales, and a finite current is observed, arising from electron tunneling between the conducting tip and sample. In a simplistic picture, one can consider the problem to be equivalent to tunneling across a barrier of finite height, $\bar{\phi} = (\phi_t + \phi_s)/2$, the average work function of the tip and the sample; and finite width, z (Fig. 2-1b). Therefore, for small voltages ($eV \ll \bar{\phi}$), the tunneling current, proportional to the tunneling probability, is given by the
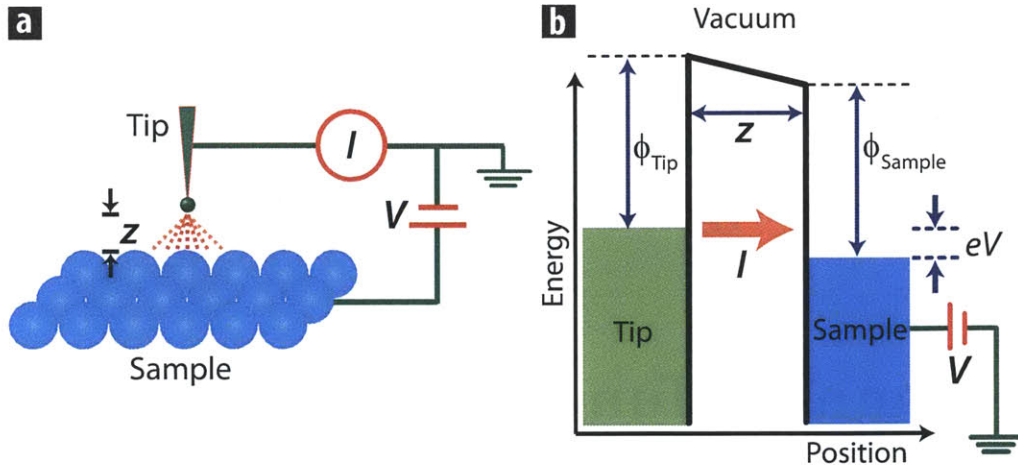
Figure 2-1: Electron Tunneling on the Atomic Scale. (a) A schematic representation of electron tunneling between an atomically sharp tip and an atomically flat sample surface separated by a vertical distance z. **(b)** Spectroscopic depiction of the tunneling process, modeled as quantum tunneling across a finite barrier of width z[28], with the barrier height corresponding to the work functions of the tip and sample, ϕ_{tip} and ϕ_{sample} respectively.

following expression under the WKB approximation[29, 30]:

$$I_{\text{F}}(z) \sim I_0 \, \exp\left(-2z \, \frac{\sqrt{2m_e\bar{\phi}}}{\hbar}\right) \equiv I_0 \, \exp\left(-2\kappa z\right) \tag{2.1}$$

The tunneling parameter, κ is of order 1 Å^{-1} for typical metals (corresponding to $\phi \sim 4-5$ eV). Therefore, a 1 Å change in z corresponds to an order of magnitude change in current - which gives the STM its extraordinary sensitivity to sample corrugations. Under typical circumstances for our instrument, the $\mathcal{O}(\text{pA})$ limits for detecting the tunneling current corresponds to ~ 500 fm limits on determining the z-corrugation.

The precise determination of z, together with the ability to control the movement of the STM tip with picometer precision, allow the STM to measure the sample topography on the atomic length scale[31]. A more detailed schematic of an STM measurement is shown in Fig. 2-2a. The x, y, z positions of the STM tip relative to the sample (with x, y directions defined to be in the plane of the sample) are controlled by mounting the tip on a piezoelectric tube. By applying voltages to the 'piezo', the tip is manipulated in these three directions. While recording the sample topography, the tip is typically held in constant current feedback, i.e. the tip is rastered on the surface while using analog feedback to maintain a constant current by moving the tip in the z direction, and the resulting z-position is recorded as a function of x and y.

The STM head that has been used to perform the experiments described in this thesis is shown in Fig. 2-2b. The tip-sample configuration, annotated in the figure, is flipped in the microscope,
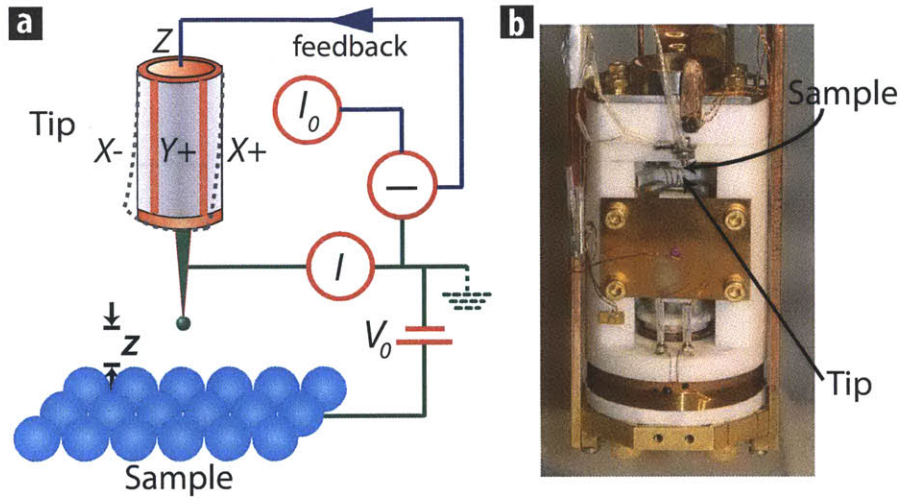
Figure 2-2: The Scanning Tunneling Microscope. (a) A schematic representation of an STM tip held in feedback above an atomically flat sample surface. The STM tip is mounted on a piezoelectric tube, and the voltages applied on the tube $(X_{\pm}, Y_{\pm}, Z)$ move the tip in the respective directions. Constant tip-sample separation is maintained while rastering the tip over the surface using the constant current feedback loop. **(b)** A picture of the STM head used to perform the experiments described in this thesis. Note that the tip-sample configuration is inverted in comparison to the schematic in (a).

as compared to the schematic in Fig. 2-2a. The tip is brought in close proximity to the STM using a Pan-style vertical coarse positioner[32]. The design of the STM allows for maximal rigidity, reducing vibrations, and allowing the study of the same sample region over long durations. With the addition of a cryopumped 1 K stage, the instrument can be operated over 2-50 K and in magnetic fields of up to 9 T. The majority of the experimental results reported in this thesis, unless stated otherwise, were acquired at temperatures between 4–9 K, with no measurable temperature dependence over this range.

2.2 STM: Topography and Spectroscopy

A constant current topograph acquired on the topological material $Bi_2Se_3As_x$ is shown in Fig. 2-3a. The topograph shows an atomically resolved hexagonal lattice. In addition, extended triangular features - both bright and dark - are observed, which correspond to single-atom impurities - lattice vacancies and substitutions. That single atom impurities (size $\sim a_0$, where a_0 is the lattice constant) appear as extended features with a well-defined shape and symmetry that is associated with the lattice – suggests that the origin of such features is electronic, not topographic.

2.2.1 Spectroscopic Sensitivity of the STM

The sensitivity of the STM to electronic information can be understood by going beyond the simplistic model in Eqn. 2.1 and considering the tunneling process for fermions, following the work of Bardeen[33]. Using Fermi's golden rule, the tunneling current between two metallic electrodes
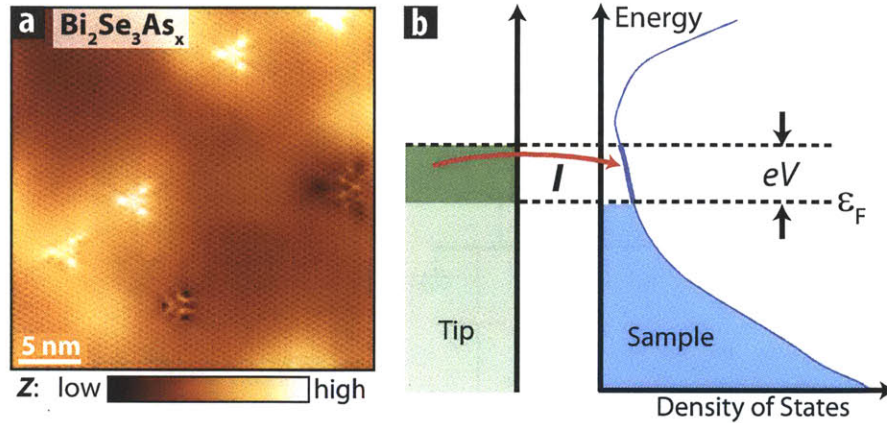
Figure 2-3: STM Topography and Spectroscopic Information. (a) A prototypical STM topograph acquired on $Bi_2Se_3As_x$, showing an atomically resolved hexagonal lattice and three different kinds of triangular single-atom impurities. The extended manifestation of these single-atom impurities corresponds to the spectroscopic sensitivity of the topographic mode of STM. Setpoint parameters: sample bias, $V_0 = -300$ mV, junction resistance, $R_J = 1$ GΩ. **(b)** Schematic illustration of the spectroscopic sensitivity of STM to the local density of states (LDOS) of the sample, integrated over the applied bias, eV and the Fermi energy, ε_F. The measured tunneling conductance, dI/dV, is therefore representative of the sample LDOS at energy eV.

with an applied voltage V between them, corresponding to the tip and the sample, across a vacuum barrier of width z, can be expressed as

$$I_T(z) \sim \int_{-eV}^{0} d\varepsilon \; |M(z, eV)|^2 \; D_t(\varepsilon) \, D_s(\varepsilon + eV) \; (f(\varepsilon) - f(\varepsilon + eV)) \tag{2.2}$$

Here $D_t(\varepsilon)$ and $D_s(\varepsilon)$ correspond to the density of states (DOS) of the tip and sample, $f(\varepsilon)$ is the Fermi-Dirac distribution function, and M is the matrix element for tunneling across the barrier. Physically, this expression is straightforward to understand from the schematic in Fig. 2-2b. At zero temperature, a tunneling current can arise only from the displacement of the Fermi levels of the tip and sample. With an applied voltage V, the Fermi levels are displaced by eV, and the elastic tunneling of electrons would correspond to the range of energies, eV, encompassed by the displaced Fermi levels (dotted lines in Fig. 2-2b). The integral represents the number of available filled (tip) and empty (sample) levels respectively for the tunneling process.

Next, we can choose a tip that has a relatively uniform DOS over the energy range of interest, so that $D_t(\varepsilon)$ can be taken outside the integral. Several metals are suitable for this purpose, and we use the alloy PtIr for our experiments.

The matrix element, M, representative of the tunneling process itself, can be described as an energy-independent square barrier under the WKB approximation (Eqn. 2.1) for $eV \ll \bar{\phi}$.

Finally at finite temperatures, $T > 0$, the spectral distribution of electrons, described by the

density of states, $D(\varepsilon)$, is convolved with the Fermi-Dirac distribution function:

$$f(\varepsilon, T) = \frac{1}{1 + \exp\left((\varepsilon - \varepsilon_{\mathrm{F}})/k_{\mathrm{B}}T\right)} \tag{2.3}$$

Eqn. 2.3 is equivalent to a thermal smearing of the DOS by $\sim 3.4\, k_{\mathrm{B}}T$[34], corresponding to 1.2 mV at the liquid helium temperatures used in our experiments. Apart from the spectroscopic comparisons between data acquired at very different temperatures (§ 8.6.1), where the spectral convolution with the Fermi function needs to be explicitly accounted for[35], we can ignore the $\mathcal{O}(1\,\mathrm{mV})$ smearing effects of the Fermi function. With these approximations, Eqn. 2.2 reduces to

$$I_{\mathrm{T}}(z) \sim \exp\left(-2\kappa z\right) \int_0^{eV} d\varepsilon\, D_{\mathrm{s}}(\varepsilon) \tag{2.4}$$

Therefore, the tunneling current between the tip and sample is exponentially sensitive to the tip-sample separation, z, and linearly sensitive to the integral of the density of states over energies from the Fermi level to the applied bias, eV_0.

2.2.2 The Data Acquisition Modes of an STM
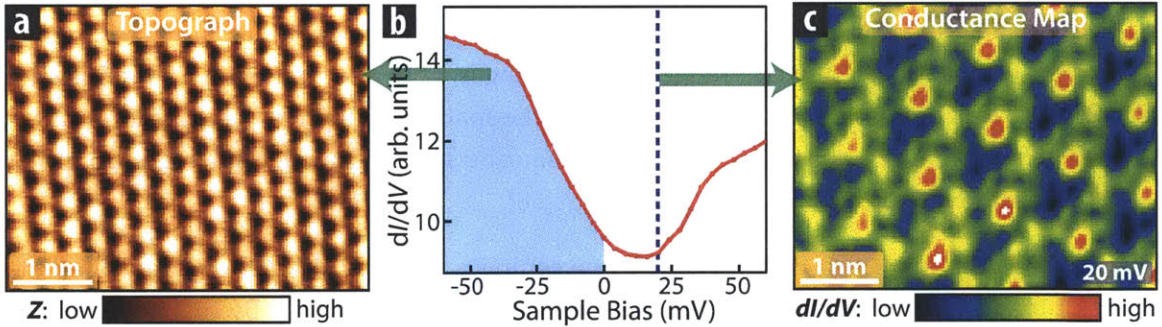
Figure 2-4: The Simultaneous Data Acquisition Modes of STM. (a) An STM topograph acquired on $2H$-NbSe$_2$, showing a $\sim 3a_0$ periodic charge density wave (CDW) modulation $V_0 = $ -60 mV; $R_{\mathrm{J}} = 1$ GΩ. **(b)** A dI/dV spectrum averaged over the field-of-view in (a). Shaded cyan region corresponds to the LDOS integral resulting the CDW modulation in (a), and the dashed blue line corresponds to the bias voltage for (c). **(c)** dI/dV map at +20 mV over the field-of-view in (a), acquired simultaneously with (a) and (b). (b-c): $V_0 = $ -60 mV; $R_{\mathrm{J}} = 0.2$ GΩ; $V_{\mathrm{mod}} = 3$ mV.

Following Eqn. 2.4, the STM is typically used to acquire topographic and spectroscopic data in three modes, shown in Fig. 2-4.

First, the constant current topographic mode, detailed previously, involves rastering the tip over the surface, with lateral tip position $\vec{r} \equiv (x, y)$, while maintaining a constant current I_0 with bias setpoint V_0. The measured topographic elevation $z_{\mathrm{STM}}(\vec{r}, V_0, I_0)$ can be given by

$$z_{\text{STM}}(\vec{r}, V_0, I_0) \simeq z_{\text{T}}(\vec{r}) + \frac{1}{\kappa(\vec{r})} \cdot \ln \left(\frac{I_0}{\int_0^{V_0} dV \, eD_s(\vec{r}, eV)} \right) \tag{2.5}$$

Here $z_{\text{T}}(\vec{r})$ is the true topographic corrugation of the sample, $\kappa(\vec{r})$ is a measure of the local tunnel barrier height (LBH), and $D_s(\vec{r}, eV)$ is the local density of states (LDOS) of the sample at energy eV. Such a topograph is shown in Fig. 2-4a.

Second, upon differentiating Eqn. 2.4, we find that the STM can also be used to directly acquire local spectroscopic information.

$$\frac{dI}{dV}(\vec{r}, V) \sim D_s(\vec{r}, eV) \tag{2.6}$$

Experimentally this is accomplished by initially fixing the x, y, z position of the tip in feedback (I_0, V_0: Fig. 2-2a). The feedback is then switched off, and the bias V is swept over the energy range of interest, and the differential conductance dI/dV is recorded using a lock-in technique - producing a spectrum as shown in Fig. 2-4b. As an aside, we caution that a prefactor on the right hand side of Eqn. 2.6 (not shown for simplicity) can vary spatially in some electronically inhomogeneous materials, complicating the absolute comparison of spectra acquired at different spatial locations[36, 37].

Third, by rastering the tip on the surface and acquiring spectra over the field of view, spatial dI/dV maps can be acquired over a range of bias voltages, with a representative example shown in Fig. 2-4c. To first order, these maps correspond to the spatial variation of the DOS, as in Eqn. 2.6. In principle, such maps, when acquired over the requisite spectral range, can be used to measure the spatial variation of electronic order parameters[38].

Lastly, we note that from Eqn. 2.4 that by sweeping z over 1–2 Å and recording the out-of-feedback tunneling current, one can measure the local barrier height[34]. By repeating this measurement as a function of position, the spatial variation in the local barrier height can also be measured[36, 39]. This last technique is not used to acquire any results for the experiments described in this thesis.

2.3 Spectroscopic STM and Momentum Resolution

The atomic scale spatial resolution of STM, in conjunction with its ability to spectroscopically measure the single particle DOS has resulted in its extensive use in discerning various electronic phenomena that manifest in the LDOS of numerous materials[34, 40]. For example, spectroscopic STM has enabled the visualization of spectral resonances associated with single-atom impurities in various metals and superconductors[41–43], electronic inhomogeneity associated with spa-

tially varying order parameters[38], the core structure of vortices and their spatial order in several superconductors[44–48], and atomic-scale translational and rotational symmetry breaking states in various materials[37, 49–51]. The ability to combine spectroscopic STM with epitaxial growth techniques has further enabled the investigation of superconducting order in laterally[52] and vertically[53] confined structures on the atomic scale. Moreover, the unique spectral sensitivity of STM to empty states (above ε_F) has been successfully used to study various phenomena that exhibit particle-hole asymmetry[42].

In addition to its spectroscopic and spatial sensitivity, STM has also been shown to provide momentum resolved information through quantitative measurements of two phenomena – Landau quantization of the DOS in the presence of a magnetic field, and the scattering of electron waves from single-atom impurities that results in quasiparticle interference patterns.

In a two dimensional system, electrons correspond to well-defined states in momentum space, known as Bloch states[1]. They can be described by the the energy-momentum relationship, or dispersion, $\varepsilon(\vec{k})$, where $\vec{k} = (k_x, k_y)$ is the in-plane momentum. For conventional electrons, also known as *free fermions*, the dispersion is parabolic – $\varepsilon(k) = k^2/2m_e$ (Fig. 2-5a). In contrast, for *Dirac fermions* (massless electrons), the dispersion is linear – $\varepsilon(k) = \hbar v_F k$ (Fig. 2-5d).

In the following sections, we describe the origin of these two phenomena in the context of 2D electron systems (2DES), and discuss how they enable spectroscopic STM to access k-space information.

2.3.1 Landau Quantization

In the presence of a perpendicular magnetic field B, classical electrons moving with speed v_e experience a Lorentz force $\vec{F}_e = -e\vec{v} \times \vec{B}$ perpendicular to their direction of motion. As a result, they describe circular (cyclotron) orbits with radius $R_c = m_e v_e/eB$, where v_e is the magnitude of the in-plane velocity of the electron[54]. In the semiclassical picture, the circumference of these cyclotron orbits is quantized to an integer number of electron wavelengths ($2\pi R_c = N\lambda_e$), with the electron wavelength given by the de Broglie relation $\lambda_e = h/mv_e$. The energy-momentum relationship of the electrons can therefore be used to deduce the semiclassical quantization of these cyclotron orbits - known as Landau levels (LLs).

It is found, by solving the Schrödinger equation in the presence of a magnetic field, that for free fermions, the LL energies disperse with quantization index N, in the following form

$$\varepsilon_{N,\text{free}} = \varepsilon_0 + (N + 1/2)\,\hbar\omega_c \tag{2.7}$$

Here ε_0 is the bottom edge of the electron band and $\omega_c = eB/m_e$ is the cyclotron frequency. That free fermion LLs in 2D are equally spaced, separated by the cyclotron energy, $\hbar\omega_c$ (Fig. 2-
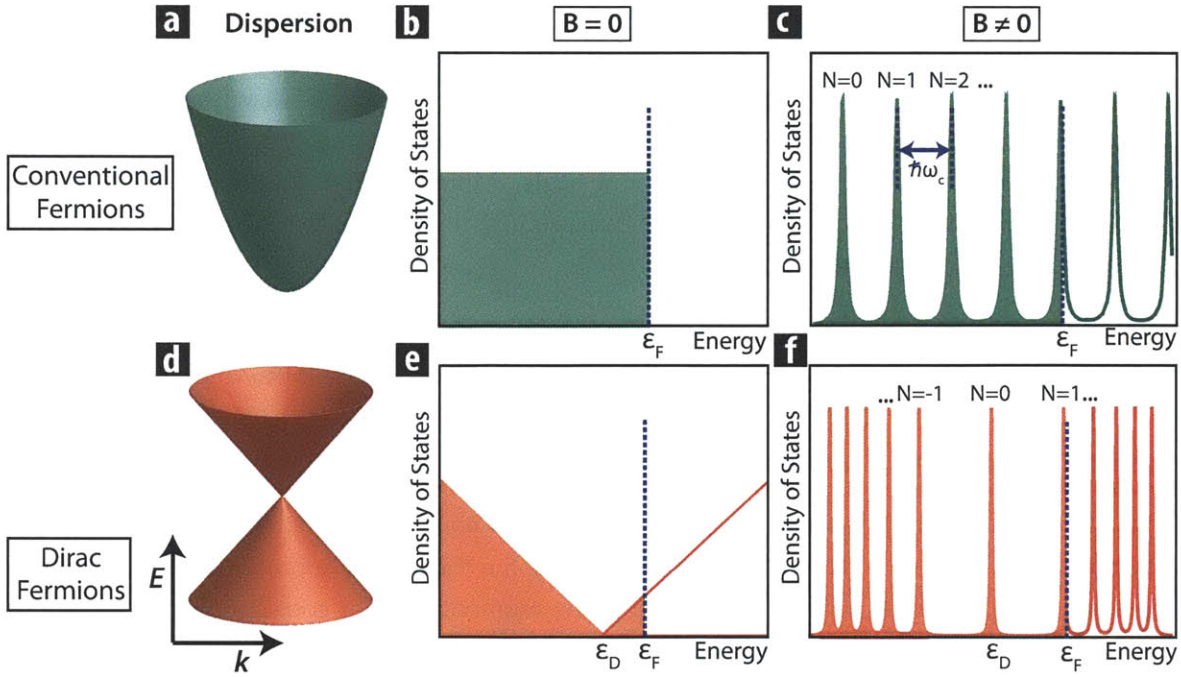
Figure 2-5: Landau Quantization of Two Dimensional Electron Systems. Illustrating the manifestation of Landau quantization of massive and massless fermions in two-dimensional systems. A schematic picture of the 2D band structure of **(a)** massive (parabolic) and **(d)** massless (linear, or Dirac) is shown. This results in a DOS spectrum that is spectrally **(b)** flat and **(e)** linear respectively. The application of a magnetic field results in Landau quantization, with **(c)** equally spaced and **(f)** unequally spaced Landau levels for these cases.

5c), can be understood in the following manner. The density of states (DOS) of free fermions at zero field, $D_{\mathrm{free}}(\varepsilon)$, corresponding to the k-space integral over the parabolic band, is uniform in energy: $D_{\mathrm{free}}(\varepsilon) = m_e/\pi\hbar^2$ (Fig. 2-5b). In the presence of a magnetic field, the DOS is quantized into LLs, and each LL has an identical degeneracy, corresponding to the number of flux quanta, $B/\phi_0 \equiv eB/h$[55]. Therefore, the quantization of a flat DOS into levels of identical degeneracy results in equally spaced LLs, separated by $\hbar\omega_c$, as shown in Fig. 2-5c.

In contrast, for Dirac fermions in two dimensions, the linear dispersion (Fig. 2-5c) results in a linear DOS away from the Dirac point, ε_D, i.e. $D_{\mathrm{Dirac}}(\varepsilon) = (A/\pi v_F^2) \cdot |\varepsilon - \varepsilon_D|$ (Fig. 2-5e)[3]. The degeneracy of LLs being the same as for free fermions, the linear DOS is split into LLs now spaced unequally, with

$$\varepsilon_{N,\mathrm{Dirac}} = \varepsilon_D + v_F\sqrt{2e\hbar NB} \tag{2.8}$$

In this case, the $N = 0$ LL, located at the Dirac point, does not disperse with magnetic field[1][3].

---

[1]The $N = 0$ LL does exhibit a small dispersion due to the Zeeman term associated with the electron g-factor, which we neglect for simplicity.

The dispersion of higher LLs on either side of the Dirac point therefore scales with $\sqrt{NB}$, a distinguishing feature of Dirac fermion LLs (Fig. 2-5f).

While an infinite number of LLs can exist in principle at all magnetic fields and temperatures, they are not always experimentally accessible due to broadening effects. The spatial extent of the LL wavefunctions, equivalent in principle to the radius of the cyclotron orbits, is given by[55]

$$R_N = \sqrt{(2N + 1)\hbar/eB} \equiv \sqrt{2N + 1}\, l_B \qquad (2.9)$$

The spatial extent of the LLs can therefore be described in terms of the LL index, N, and the magnetic length $l_B = \sqrt{\hbar/eB}$, $\sim$ 8.5 nm in a 9 T magnetic field. The presence of disorder in the 2DES and finite temperatures results in scattering of the Landau quantized quasiparticles, broadening the LLs from the ideal δ-functions (Fig. 2-5c, f). When the disorder in the 2DES is low enough such that the mean free path, l_F, is greater than the spatial extent of the LL, R_N, the corresponding LLs are observable. Equivalently, LLs are observable when the electron is allowed to complete a full orbit (circumference πR_N) without scattering, i.e. for $R_N \lesssim l_F$.

As discussed in § 1.3, transport and thermodynamic measurements are sensitive probes of the Fermi level DOS, $D(\varepsilon_F)$. In the presence of a magnetic field, Landau quantization corresponds to oscillations in the DOS(Fig. 2-5c, f). Depending on the experimental conditions, the Fermi energy ε_F could in principle be pinned within a LL, or in between two LLs, corresponding to a maximum or minimum in $D(\varepsilon_F)$ respectively. By varying the magnetic field B, or equivalently the electron density n_e, one can sweep ε_F through LLs, producing oscillations in $D(\varepsilon_F)$, and consequently in the measured transport and thermodynamic properties. These *quantum oscillation* measurements can therefore probe the Fermi level physics of LLs.

Spectroscopic STM has access not only to $D(\varepsilon_F)$, but also to the DOS of filled and empty states. Therefore STM can, in principle, measure the LL dispersion directly, with the LLs manifesting as oscillations in the dI/dV spectra (analogous to Fig. 2-5c, f). Additional field-dependent or density-dependent measurements can enable access to the quasiparticle band structure[56] and interaction effects[22] respectively. Here we focus on the former - the correspondence between Landau quantization and the band structure.

LLs correspond to quantized orbits in real space, as well as in k-space. At a given magnetic field and energy, LL quasiparticles describe closed orbits along constant energy contours (CECs) in k-space. Therefore LLs at a given magnetic field correspond to CEC slices in k-space, as shown for the case of graphene in Fig. 2-6a. In the semiclassical limit (large LL index, N), the Bohr-Sommerfeld quantization relation gives the area in k-space for the Nth LL to be[56]:

$$A_N = \pi q_N^2 = \frac{2\pi e}{\hbar} \cdot (N + \gamma) B \qquad (2.10)$$
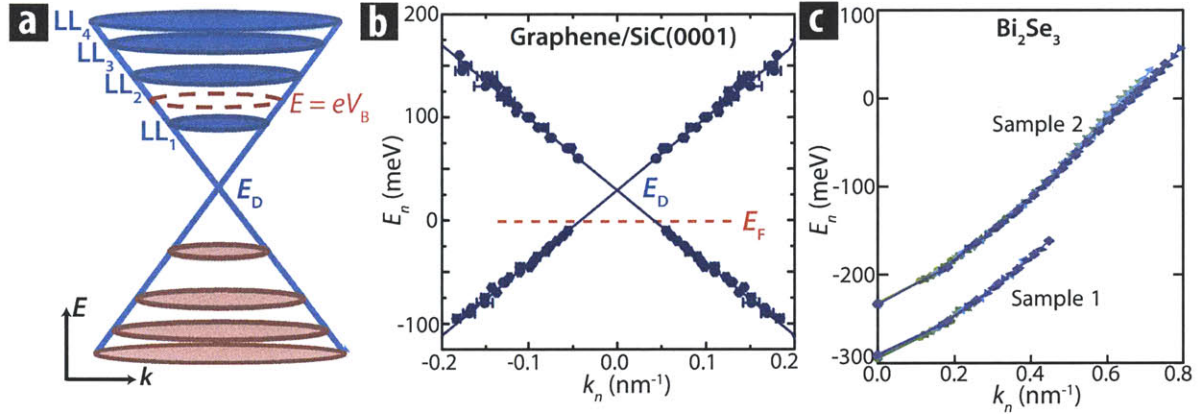
Figure 2-6: Landau Level Spectroscopy and Band Structure Extraction. Illustration of how STM LL spectra can be used to measure a 2D band structure. **(a)** Quantized LLs at a given magnetic field correspond to closed contours of constant energy (CECs) in momentum space, as shown for graphene (adapted from [57]). **(b-c)** Semiclassical quantization, with the LL index, n and magnetic field, B can be used to obtain the momentum q_n of the LL, and determine the $\varepsilon_n(q_n)$ LL mode dispersion (adapted from [57] and [56] respectively).

The phase factor γ, determined by the Berry phase of the quasiparticle, is $1/2$ for a free electron and 0 for a Dirac fermion[56]. Therefore, field-dependent LL spectra can be used to identify N and γ, and therefore extract the momenta q_N. Furthermore, the $\varepsilon_N(q_N)$ dispersion can be used to determine the quasiparticle band structure corresponding to Landau quantized portion of the Fermi surface (FS). In the case of 2D materials with a single band, this can be used to directly extract the band structure, as shown in Fig. 2-6b-c for graphene[57] and Bi_2Se_3[56] respectively.

This technique, from the perspective of a band structure tool, offers the following advantages: (a) temperature-limited energy resolution, (b) nanoscale spatial resolution at the order of the magnetic length, $l_B = \sqrt{\hbar/eB}$, (c) sensitivity to many-body interactions due to its immunity to limitations imposed by Kohn's theorem[58], and (d) sensitivity to disorder and other broadening mechanisms.

The existence of quantized LLs in STM spectra was reported first by Wildöer *et al.*[59], and subsequently by Morgenstern *et al.*[60] – both on 2DES on InAs. While LL spectroscopy in several of these systems can be sensitive to the shape of the STM tip and associated induced electric fields[57, 60], it has been useful for understanding several qualitatively new phenomena. For example, it has been used to visualize the existence of nanoscale chemical potential fluctuations[22, 61], to demonstrate the existence of new broken symmetry states[62], and to study the effect of electron-electron interactions[22] and disorder-induced localization[63, 64] in various 2D systems.
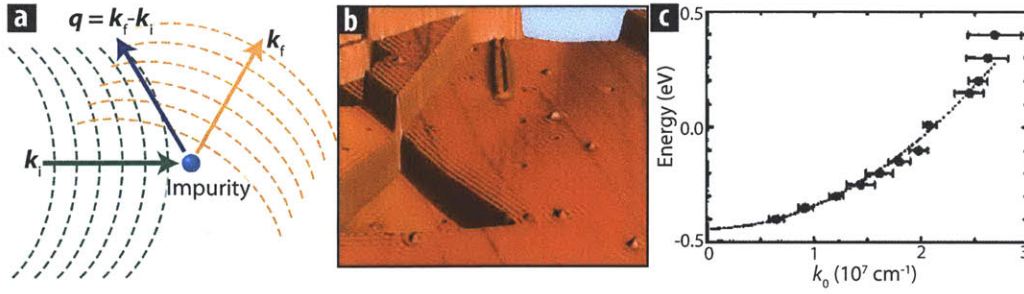
Figure 2-7: Impurities, Scattering and Quasiparticle Interference. (a) A cartoon illustration of quasiparticle interference from a single impurity. An incoming electron wave with wavevector $\vec{k}_i$ is elastically scattered to wavevector $\vec{k}_f$. This forms standing wave interference patterns with wavevector $\vec{q} = \vec{k}_f - \vec{k}_i$. **(b-c)** Standing wave patterns formed due to quasiparticle scattering from atomic steps and impurities, as seen in a constant current STM topograph (b). Corresponding conductance ($dI/dV(\vec{r}, V)$) maps can be analyzed in Fourier space to extract the quasiparticle dispersion, $q(\varepsilon)$, corresponding to the parabolic dispersion of free fermions (c). Adapted from [65].

2.3.2 Quasiparticle Interference

While the presence of impurities on the surface of 2D materials can limit the observation of LLs, it can result in the emergence of another phenomenon affording k-space information to STM, known as quasiparticle inference (QPI). QPI arises due to the elastic scattering of electronic quasiparticles from a point impurity, and manifests as a 'standing wave pattern', corresponding to the interference between incoming and outgoing 'waves' associated with quasiparticle states (Fig. 2-7a).

The real space wavefunction associated with a 2D electron gas is expected to be of the Bloch form, $\psi_{\vec{k}}(\vec{r}) = u_{\vec{k}}(\vec{r}) \exp\left(i\vec{k} \cdot \vec{r}\right)$. The STM conductance $dI/dV(\vec{r}, eV)$, sensitive to the spatial variation in LDOS, $D(\vec{r}, \varepsilon)$, corresponds to the square of the wavefunction, $\left|\psi_{\vec{k}}(\vec{r})\right|^2$, the spatial variation of which derives entirely from $u_{\vec{k}}(\vec{r})$, corresponding to atomic periodicity. This, however, holds only for perfect translational invariance, which is broken by impurities. In this case, mixed states are allowed to exist, corresponding to linear combinations of Bloch states with the same energy. The mixing of Bloch states, e.g. corresponding to momenta $\vec{k}_i$ and $\vec{k}_f$, results in spatial variations in the form of interference patterns, with periodicity $\lambda_{\mathrm{int}} \equiv 2\pi/|\vec{q}_{\mathrm{int}}|$, with $\vec{q}_{\mathrm{int}}(\varepsilon) = \vec{k}_f(\varepsilon) - \vec{k}_i(\varepsilon)$.

In the case of an isotropic band, as in Fig. 2-5a, the CECs are circular, and therefore isotropic. It was shown for this case by Friedel that density modulations introduced by impurity scattering would be peaked in reciprocal space at k_F and $2k_F$, where k_F is the Fermi wavevector[66]. More generally, the joint density of states (JDOS), equivalent to the autocorrelation of the single-particle spectral function, $A(\vec{k}, \varepsilon)$, is a good measure of the momentum space scattering intensity. The JDOS is given by

$$D_{\text{JDOS}}(\varepsilon, \vec{q}) = \int_{\text{CEC}} d^2\vec{k}\, A(\vec{k}, \varepsilon)\, A(\vec{k} + \vec{q}, \varepsilon) \tag{2.11}$$

For an isotropic dispersion (Fig. 2-5a), $D_{\text{JDOS}}(\varepsilon, \vec{q})$ peaks at $q = 2k_{\text{rad}}(\varepsilon)$, where $k_{\text{rad}}(\varepsilon)$ is the CEC radius at energy ε. For example, at the Fermi energy, this corresponds to a peak at $2k_{\text{F}}$. Therefore, the magnitude of the scattering vector, q_{QPI}, maps directly to the CEC radius as $q_{\text{QPI}} = 2k_{\text{rad}}$.

The LDOS oscillations produced by impurities (and steps) can be directly visualized in STM conductance maps, by imaging standing wave patterns – as shown in Fig. 2-7b for the surface of Cu(111)[65]. By varying the bias voltage, one can measure the dispersion of the oscillation periodicity with energy, i.e. $q_{\text{QPI}}(\varepsilon)$. The mapping from q_{QPI} to k_{rad} allows a quantitative determination of the band structure if the CEC shape is known (Fig. 2-7c, [65]). This technique can be extended to 2D materials with anisotropic band structures, where the JDOS has a well-defined q-space structure[67].

The temperature-limited energy resolution and field-of-view limited momentum resolution offered by QPI, in addition to spatial sensitivity, makes it an ideal complement to ARPES as a band structure probe. Indeed the presence or absence of various scattering modes in QPI studies have been used to understand the interplay of symmetries with electronic properties in several 2D materials. The absence of a $2k_{\text{F}}$ (backscattering) wavevector in QPI patterns of surface states has been used to explicitly confirm time reversal symmetry in topological materials (TMs)[68, 69]. Conversely, the observation of the $2k_{\text{F}}$ wavevector has been used to illustrate the breaking of time reversal symmetry in magnetically doped TMs[70] and the absence of pseudospin protection in graphene[21, 71]. The utility of QPI in understanding the role of time-reversal symmetry in topological materials is detailed in § 3. Furthermore, QPI has also been used to visualize nanoscale chemical potential fluctuations in these materials[14, 21, 23]. In addition to its utility in studying 2D materials, QPI has proven to be a remarkably useful probe of 2D band structures in strongly correlated materials, specifically towards studying Bogoliubov quasiparticles, and identifying pairing symmetry and coherence factors in various high-T_c superconductors[56, 72–76], and studying hybridization in heavy fermion systems[77].

2.3.3 Landau Quantization and QPI in Graphene: An Apparent Conflict?

While there is great promise towards establishing a quantitative nanoscale band structure probe through the two complementary techniques of Landau quantization and QPI, we are currently faced with certain limitations. First, LLs and QPI have never been observed over the same energy range in the same material, and therefore their quantitative equivalence in measuring the quasiparticle band structure has yet to be established. More concerningly, independent reports of QPI and LLs in single-layer graphene on SiO_2(Fig. 2-8), which should have yielded the same dispersion value, show discrepancies of up to 40%[21, 78]. The origin of discrepancies has been attributed to local gating due to the STM tip and to collective modes, but these are yet to be quantified[21, 22].
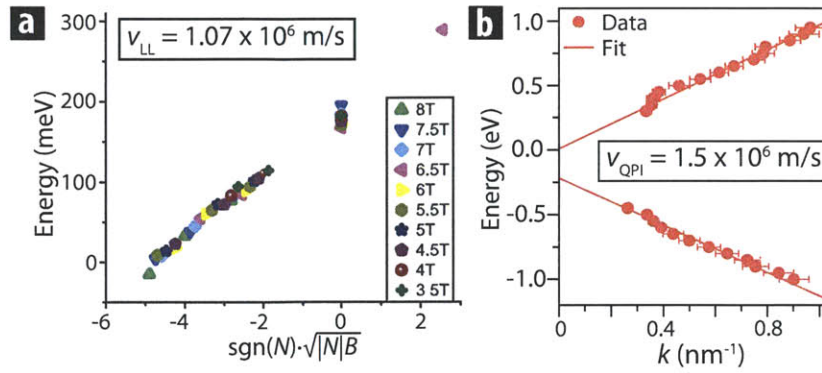
Figure 2-8: Spectroscopic STM on Single-Layer Graphene: Comparing Landau Quantization and Quasiparticle Interference. A comparison of the 'Dirac cone dispersion' extracted from independent measurements of Landau quantization and QPI measurements on single layer graphene (SLG) on SiO_2. (a) Field dependent Landau quantization measurements give a linear dispersion with $v_{LL} = 1.07 \times 10^6$ m/s (adapted from [78]). **(b)** Quasiparticle inteference patterns in spatial conductance maps give a linear dispersion with $v_{QPI} = 1.5 \times 10^6$ m/s. Both the dispersions reported in (a) and (b) correspond to a nominally identical Dirac cone, with a 40% discrepancy in the measured dispersion.

From an experimental standpoint, this discrepancy calls into question the complementary use of LLs and QPI in determining the band structure of 2D materials. Importantly, the determination of a non-trivial band structure using both these techniques has yet to be performed, in order to quantitatively establish the momentum resolution of spectrosopic STM. This motivates the work reported in the first part of this thesis.

Part I

Momentum-Resolved STM on Topological Materials

In this part of the thesis, we describe our momentum-resolved spectroscopic studies of the topological semimetal antimony (Sb).

We begin by motivating the origin of topological order from spin-orbit coupling driven band inversion, necessiating the presence of robust surface states. We then understand the nature of these surface states from a phenomenological $k \cdot p$ model. After reviewing previous spectroscopic work on topological materials, we outline the key issues that surface-sensitive spectroscopic probes need to address on these materials, and motivate the need for a momentum-resolved probe of the topological surface state band structure.

We focus on the (111) surface of the topological semimetal Sb. After describing our characterization the homogeneity of the surface topography and preliminary spectroscopy, we move on to discuss momentum-resolved measurements. First, we examine Landau quantization of the surface states in the presence of a magnetic field, which display Dirac behavior far from the Dirac point, but deviate markedly from this behavior close to the Fermi energy. We then look at spatial conductance maps that demonstrate quasiparticle interference.

Noting that these two phenomena overlap over a 300 meV energy range, we identify their momentum space origin, and combine them to reconstruct the surface state band structure of Sb(111). We thus establish momentum-resolve scanning tunneling microscopy (MR-STM) as a band structure probe, and demonstrate its nanoscale spatial sensitivity. We use the measured band structure to then understand the deviant behavior of Landau levels close to the Dirac point, in terms of a spin-split Rashba picture, and reveal the true origin of Dirac fermion Landau levels in topological materials.

Finally, we use our MR-STM studies to establish Sb(111) as a platform to study the effects of perturbations on topological surface states, and discuss the broader implications of our results towards device applications and band structure engineering.

The STM experiments reported in this work were done in collaboration with Michael M. Yee, Yang He, and Jennifer E. Hoffman at Harvard University. The samples used in the work - single crystals of Sb - were prepared by Dillon R. Gardner and Young S. Lee at MIT. The band structure calculations were peformed by Hsin Lin and Arun Bansil at Northeastern University.

The results detailed in this part of the thesis have been been submitted for publication.

Chapter 3

Topological Materials: A Brief Introduction

The connection between symmetry breaking, phase transitions, and the emergence of order is a central concept in condensed matter physics[79]. For example, structural translations, most commonly encountered in everyday life, are associated with broken translational symmetry; while magnetic phase transitions are associated with broken rotational symmetry[80]. The biggest triumph in condensed matter physics involves the explanation of the superconducting phase transition, which breaks gauge symmetry[81]. Each of these broken symmetries is associated with an order parameter below a transition temperature T_c, which can typically be described in the Landau-Ginzburg framework[81]. It was therefore very surprising when the quantum Hall (QH) state was understood in terms of a new phase that does not spontaneously break any symmetries[82, 83]. A simple understanding of this state, imperative to the physics of topological materials, can be developed using band theory.

3.1 Band Insulators and the Quantum Hall State

The electronic properties of conventional crystalline solids are remarkably well understood within the band theoretical description[1]. Each band corresponds to a set of extended states, described by the quantum numbers of crystal momentum, $\vec{k}$, and spin, σ. Bands are filled sequentially until the last electron has been accommodated. If this configuration corresponds to fully filled bands, then the Fermi energy (ε_F) lies in the band gap, and the material is an insulator. If on the other hand, the most energetic electron, and therefore ε_F, lie in a partially filled band, the material is a metal. The availability of low-energy excitations around ε_F in the the latter case is a marked contrast from the former. The emergence of myriad alternative ground states for a metal, such as superconductors, density waves, and electronic crystals - are understood to arise from the near-ε_F band structure[1]. Due to the absence of alternative ground states, the electronic properties of
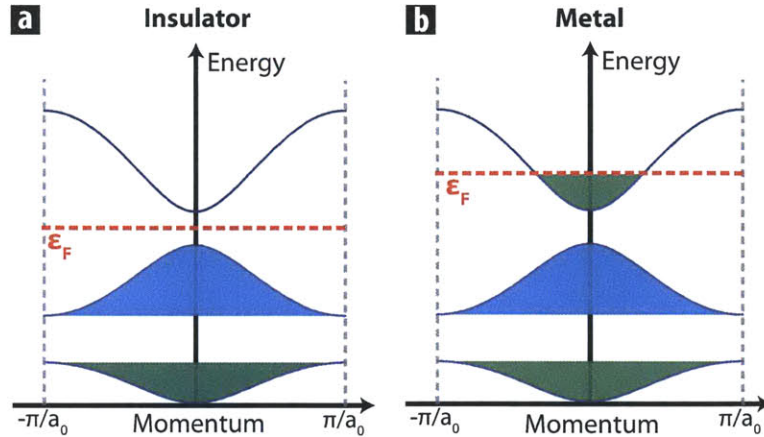
Figure 3-1: Band Picture of Solids. A schematic band structure description of a metal and insulator (lattice constant a_0). Shaded regions indicated filled states, and the dashed red line corresponds to the Fermi energy, ε_F. **(a)** Filled bands, with ε_F in the band gap, would correspond to an insulator. **(b)** A partially filled band, with ε_F in the band, would correspond to a metal.

insulators, on the other hand, have been viewed as being less interesting. It is the latter case that is understood to give rise to the QH state.

In conventional metallic systems, the transverse or Hall resistance is found to be linear with magnetic field, B, and used to determine the density and sign of charge carriers[1]. It was later found that sufficiently large magnetic fields can cause electrons to describe quantized cyclotron orbits, known as Landau levels (LLs). Such Landau quantization results in oscillations of longitudinal resistance R_{xx}, periodic in $1/B$[25]. In two dimensions, the peaks and troughs of R_{xx} (Fig. 3-2b) correspond to metallic and insulating states respectively. It was therefore quite surprising when *in the insulating state*, mesoscale devices fabricated on two-dimensional electron gas (2DEG) systems (e.g. Fig. 3-2a), showed R_H to be quantized ($R_H = h/\nu e^2$ for integer ν) with measurement-limited precision, independent of geometric details and mobility (Fig. 3-2b).

This quantization of Hall conductance ($\sigma_H = R_H^{-1} = \nu e^2/h$) corresponds the presence of ballistic metallic states on the edge of the bulk insulator[82, 85]. In the insulating state, ε_F is pinned within the 'band gap' between LLs in the bulk (Fig. 3-2c). However, at the edge, ε_F is pinned to the LL modes, and the edge is therefore conducting(Fig. 3-2c). What is more surprising, however, is the robust dissipationless nature of the quantization and its insensitivity to deformations and disorder, indicating a topological origin of the quantization.

A detailed understanding of the topological nature of the QH phase was developed by Thouless *et al.*[86], who established a fundamental distinction between classes of insulators with gapped band structures. The distinction between these classes of insulators is insensitive to smooth deformations and is derived from the total curvature (Berry phase) of the band structure across the Brillouin zone (BZ). This distinction is quantified in terms of a topological invariant (Chern num-
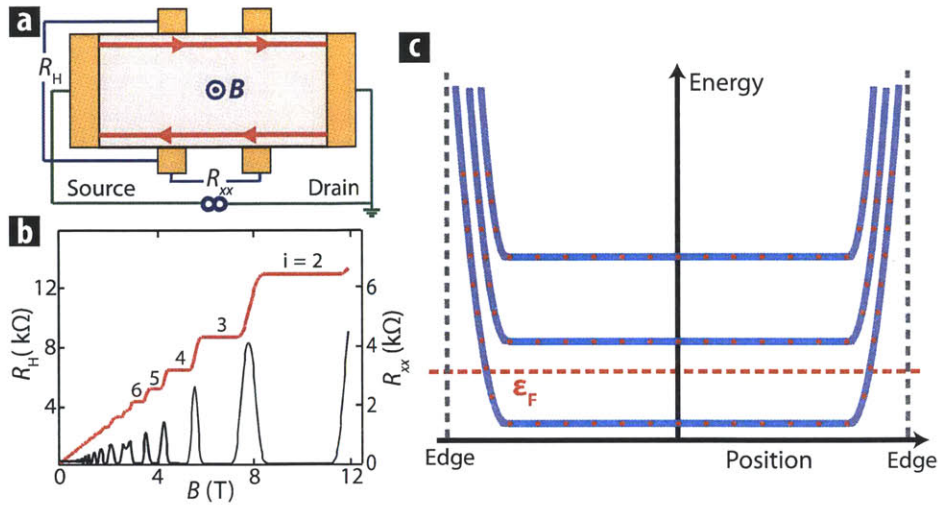
Figure 3-2: Edge States and the Quantum Hall Effect. (a) A schematic representation of the device geometry of a Hall bar patterned on a 2DEG, with the electron current flowing from the source to the drain. The magnetic field points out of the plane, and quantized Hall resistance (in (b)), arises from edge states, indicated in red. **(b)** Transport measurements on such a Hall bar device (adapted from [84]), showing plateaus in the Hall resistance, $R_{\rm H}$ (red curve), at magnetic fields corresponding to zeros in the longitudinal resistance R_{xx} (black curve). **(c)** The edge state picture of the QH state. While in the bulk, $\varepsilon_{\rm F}$ is between two LLs (cyan), corresponding to an insulating state, on the edge, it is pinned to a metallic mode (blue), which corresponds to the observed QH plateaus.

ber), $n_{\rm C}$, and it was shown that $n_{\rm C} = \nu$ for the quantum Hall insulator, and 0 for a trivial insulator, and thus that there is a topological transition between these two states[86, 87]. Therefore, it was established that the 2D insulating state generated by an applied magnetic field could have a nontrivial topology. However, the zero field analog of such a topological state remained in oblivion for over two decades.

3.2 Spin-Orbit Coupling and the Quantum Spin Hall Effect

The 2D honeycomb lattice model was the first theoretical playground for studying topological band structures. It was initially suggested that locally broken time-reversal symmetry (TRS), changing sign with lattice periodicity, could produce a topological QH state ($\sigma_{xy} = e^2/h$)[88]. When a 2D honeycomb lattice was experimentally realized in the form of single-layer graphene, Kane and Mele realized that the coupling of spin and orbital degrees of freedom could create nontrivial band topologies while preserving TRS[89]. They quantified the topology of the band structure in terms of a $\mathbb{Z}_2$ invariant. The change in this invariant between topologically distinct phases results in the existence of a nontrivial edge mode at the interface[90]. However, the small magnitude of spin-orbit coupling (SOC) in graphene meant that this was difficult to realize in practice, rather, it directed investigations of materials with strong spin-orbit coupling.

In the atomic orbital picture of band theory, SOC splits the degeneracy of the p band (Fig. 3-3a,
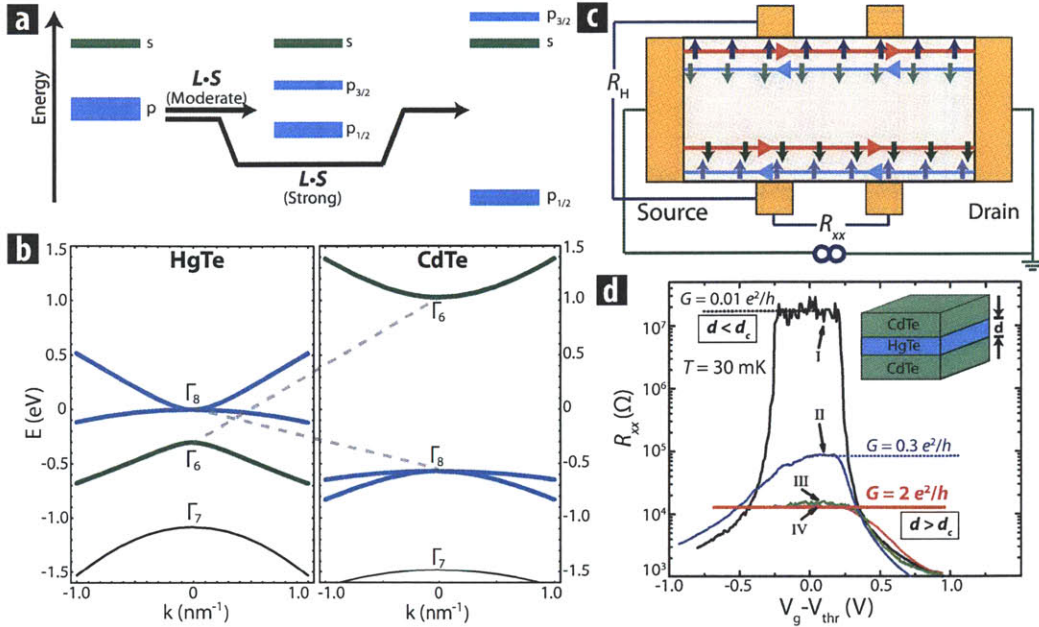
Figure 3-3: Band Inversion and the Quantum Spin Hall Effect. (a) A cartoon illustration of spin-orbit coupling (SOC) effects on band structure. Moderate SOC splits the p band, while strong SOC can invert the s and p bands. (b) SOC-induced inversion of valence and conduction bands in HgTe (left), compared with CdTe (right) (adapted from [91]). The inversion of the Γ_6 and Γ_8 bands (dashed grey lines) introduces a nontrivial band topology in HgTe. (c) Schematic of a transport measurement device on HgTe quantum well heterostructures. Ballistic conduction (red lines) is expected from spin-polarized edge states. (d) Transport measurements on quantum wells heterostructures of HgTe/CdTe, showing ballistic conduction ($\sigma_{xx} = 2e^2/h$) for devices with quantum well thickness $d > d_c$ ($d_c \simeq 6.5$ nm), in agreement with theory (adapted from [92]). Inset shows a schematic of the heterostructure.

center). Typically this splitting is much smaller than that between the s and p bands. However, in materials with heavy elements, the ensuing strong SOC can split the p-band by a large enough magnitude to invert the s-p band structure (Fig. 3-3a, right). Bernevig *et al.* found that such an SOC-induced inversion occurs between the 2D band structures of the semiconductors CdTe and HgTe (Fig. 3-3b, [91, 93]). The change in parity associated with the inversion in HgTe corresponds to a topological phase transition. Bernevig *et al.* further suggested that a heterostructure consisting of a HgTe quantum well of thickness d sandwiched between CdTe layers (Fig. 3-3d, inset) would have topological edge modes for $d > d_c$ ($d_c \simeq 6.5$ nm)[91].

This was experimentally verified by König *et al.*, who performed longitudinal transport measurements on devices fabricated on HgTe/CdTe heterostructures (Fig. 3-3d, inset). While devices with $d < d_c$ were found to be insulating, corresponding devices with $d > d_c$ showed ballistic conductance with $\sigma_{xx} = 2e^2/h$ (Fig. 3-3d). Bernevig *et al.* had predicted the existence of such dissipationless edge states, analogous to the QH edge states. In this case, the SOC introduces opposite chiralities for up and down spins, resulting in two counterpropagating modes (Fig. 3-3c). The modes are dissipationless so long as TRS is preserved, as spin-flip backscattering, which can

mix these modes, would be forbidden[93]. With an applied source-drain bias, the two modes with opposite spin on each edge (Fig. 3-3c) produce a net charge current corresponding to $\sigma_{xx} = 2e^2/h$. Subsequent nonlocal transport measurements have verified the presence of these dissipationless edge modes[94], providing potential avenues to control and manipulate these modes.

3.3 Band Inversion and Topological Surface States

Following the work of Kane and Mele[90], and Bernevig *et al.*[91] for two dimensional systems, the generalization of a state with nontrivial $\mathbb{Z}_2$ invariants to three dimensions was formulated independently by the groups of Fu, Kane and Mele[95]; Moore and Balents[96]; and Roy[97], thereby defining the concept of a *topological insulator*.

3.3.1 Bulk-Boundary Correspondence
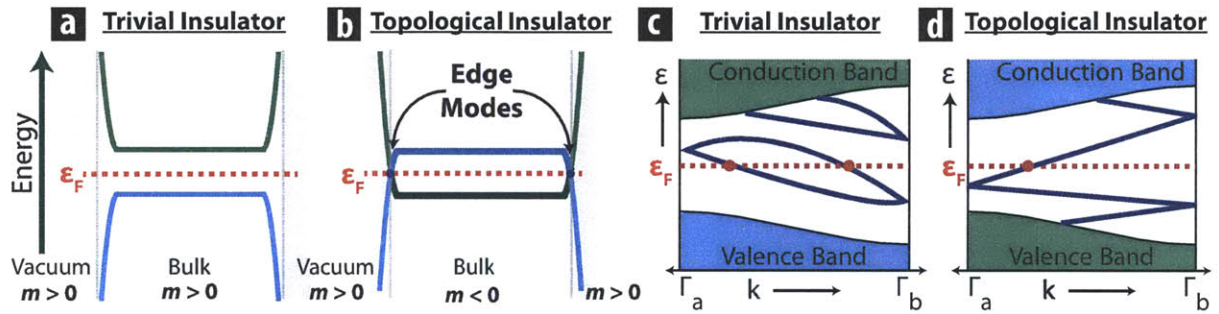
Figure 3-4: Band Inversion and Topological Surface States. (a, b) Schematic illustration of the emergence of metallic modes at the edge of an insulator. SOC-induced bulk band inversion and the bulk-boundary correspondence necessitate the existence of edge modes in (b) (c.f. (a)). **(c, d)** Schematic illustrations of the SS band structure (blue) spanning the bulk gap for trivial and topologically protected states (partly adapted from [87]). SSs are required to connect at time reversal invariant (TRI) momenta, and can either do so in a pairwise fashion (c), or can rigidly connect the valence and conduction bands (d).

It was realized that in an insulator with an SOC inverted band structure, additional parity considerations could lead to a topological band structure, with the $\mathbb{Z}_2$ invariant, $\nu_0 = 1$[95]. At the interface of a topological insulator with a trivial insulator, such as vacuum, the change in the topological invariant is associated with the bulk band gap going smoothly to zero and changing sign (Fig. 3-4b). The bulk boundary correspondence necessiates the presence of metallic edge modes (surface states for a 3D material) at the interface, associated with the change in sign of the band gap[87]. Therefore, there is a direct correspondence between an insulating band structure with the $\mathbb{Z}_2$ invariant, $\nu_0 = 1$, and the existence of protected, metallic states on the surface of such an insulator[95].

Fu and Kane went further to provide a recipe for determining ν_0 for a given material based on the the band structure[95]. For a spin-1/2 system that preserves TRS, Kramers theorem requires the existence of two-fold degenerate eigenstates, corresponding to the two values of spin. SOC

breaks this spin degeneracy at all momenta except at time reversal invariant (TRI) points, e.g. $k = 0$, $\pm\pi/a$ (a is the lattice constant). The requirement of twofold degeneracy at TRI momenta can be accomplished by either connecting these points pairwise (Fig. 3-4c), resulting in trivial edge states that can be gapped out depending on the choice of ε_F, or in a manner as to rigidly connect the valence and conduction bands (Fig. 3-4d), which cannot be gapped out for any choice of ε_F. Note that for the former case (Fig. 3-4c), an even number of states cross ε_F between two TRI momenta, while for the latter case of topological *surface states* (SS), an odd number of states cross ε_F - for any choice of ε_F. Importantly, the crossing of these states at TRI momenta is protected by Kramers degeneracy - the crossing cannot be gapped out if TRS is preserved. Fu and Kane also found that for crystals with inversion symmetry, additional parity considerations can be used to easily identify the $\mathbb{Z}_2$ invariant[98]. Using this technique, they predicted the binary compound $Bi_{1-x}Sb_x$ to be a topological insulator for $x > 0.07$[98].

3.3.2 Topological Protection of Surface States
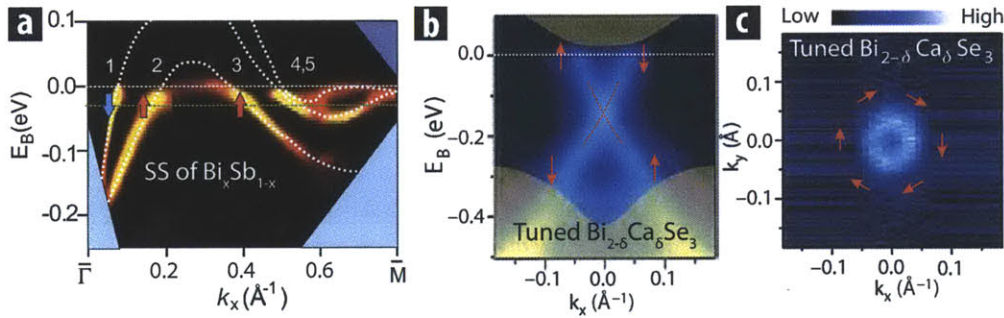
Figure 3-5: ARPES Measurements of Topological Surface States. (a) ARPES dispersion of SSs of $Bi_{1-x}Sb_x$ ($x = 0.1$). The SSs are spin-polarized (indicated by red arrows), and cross ε_F five times between TRI momenta $\bar{\Gamma}$ and $\bar{M}$, indicating their topological nature (adapted from [99]). **(b, c)** ARPES measurements of SSs of Ca-doped Bi_2Se_3, doped to tune ε_F into the bulk band gap (adapted from [100]). The linearly dispersing SSs cross at Γ to form a single Dirac cone (b), with a prototypical circular Fermi surface (c), and spin polarization indicated by red arrows.

Following the prediction by Fu and Kane, angle-resolved photoemission (ARPES) measurements by Hsieh *et al.* confirmed the topological nature of the $Bi_{1-x}Sb_x$ band structure by (1) showing that the SS cross ε_F five times between TRI momenta - an odd number of crossings (analogous toFig. 3-4d)[101], and (2) measuring the spin polarization of the SS, and showing it to be consistent with theoretical predictions[99]. These measurements of the topological SSs, shown in Fig. 3-5a, laid the foundation for the experimental investigation of these materials.

A topological insulator, or in general, a *topological material* (TM), is defined to be a material with a bulk band structure corresponding to a nontrivial $\mathbb{Z}_2$ topological invariant. As a consequence of the bulk boundary correspondence, the surface of a TM is required to host dissipationless metallic modes. These modes are spin-polarized, with spins pointing in the plane of the surface (Fig. 3-6a). Notably, the spin and momentum of the SSs are locked to each other.
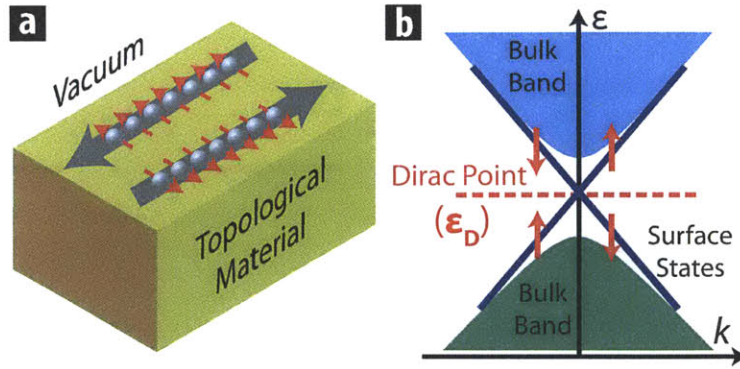
Figure 3-6: Schematic Representation of a Topological Surface States. **(a)** A cartoon illustration of a topological material (TM), with the bulk band structure resulting in protected, counterpropagating states at the surface. The SSs are spin-polarized, with locked spin (red) and momentum (blue) degrees of freedom. **(b)** Schematic band structure of a prototypical TM, with protected, SSs (blue), corresponding to helical Dirac fermions, spanning the bulk band gap. Their crossing at the Dirac point (ε_D) is protected due to TRS.

Therefore, for a fixed energy, a given direction of momentum corresponds to a unique in-plane direction of spin, and vice versa (Fig. 3-6b) - a property known as helicity. This expected helicity, coupled with the fact that the SS dispersion would be linear from the TRI point, associates these SSs with *helical Dirac fermions* - following an analogy from high energy physics. This association has led to a fascinating set of predictions towards realizing analogs of high energy phenomena in TMs, including axions and dyons[87, 93, 102]. The suggestion of using interfaces of TMs with superconductors to generate and control Majorana fermions also serves as a motivation towards topologically protected quantum computing applications[87, 93, 103].

The observation of spin textures in $Bi_{1-x}Sb_x$ consistent with theoretical predictions was therefore strongly indicative of the helical Dirac nature of these SSs. However, a complicating factor in $Bi_{1-x}Sb_x$ is the spectral coexistence of several SSs, only some of which correspond to Fig. 3-4d. Furthermore, the small band gap of $Bi_{1-x}Sb_x$ did not offer sufficient promise towards transport detection of SSs, which would be dominated by bulk states. This prompted a search for materials with a large bulk band gap and simple SS band structure. Therefore, the experimental discovery of Bi_2Se_3 as a single Dirac cone TM with a ~ 300 mV gap[104], confirmed by band structure calculations[105] was very well received. Further work by Hsieh *et al.* [100], demonstrating chemical potential tuning via chemical doping (Fig. 3-5b), and the existence of a simple, Dirac cone with spin-momentum locking (Fig. 3-5c), generated much excitement in the transport community. The theoretical prediction[105] and experimental observation of other TMs in the binary chalcogenide class - Bi_2Te_3[106, 107] and Sb_2Te_3[107] - opened the doors for developing TMs and studying their properties using various experimental and theoretical techniques.

An important consequence of the helical Dirac nature of the SSs is manifested in its scattering signature. For a simple 2D system with a circular FS in the absence of spin texture, the electronic DC susceptibility, $\chi(q, \omega = 0)$, peaks at $q = 2k_F$, and therefore the mobility of typical 2D systems
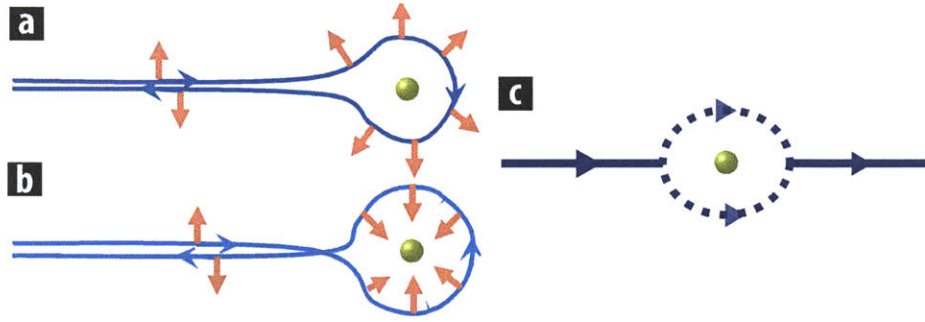
Figure 3-7: Suppression of Backscattering of Topological SSs. (a-c) Illustration of the interaction between a topological SS and a nonmagnetic impurity (partly adapted from [93]). Elastic backscattering of the SS is required to flip the spin by 180° due to spin-momentum locking, accomplished either by rotating the spin by $-\pi$ (a) or $+\pi$ (b). The destructive interference between (a) and (b), results in the suppression of backscattering, and therefore forward transmission (c).

is typically limited by $2k_F$ scattering, also known as backscattering. In TMs, the locking of spin and momentum degrees of freedom means that a momentum flip, corresponding to $2k_F$ scattering, is also required to flip the spin. As shown in Fig. 3-7a-b, this spin flip can be achieved in two distinct ways, corresponding to rotating the spin by $\pm\pi$ respectively. Note however that the spin degree of freedom for a spin-1/2 fermion needs to be rotated by 4π to bring it back onto itself, and hence the relative rotation of 2π between the scattered configurations of (a) and (b) corresponds to a phase difference of π for scattering from nonmagnetic impurities. Therefore, these configurations interfere destructively, resulting in the complete suppression of backscattering. The absence of backscattering, detectable using STM measurements, was shown to hold for $Bi_{1-x}Sb_x$ by Roushan *et al.*[68] and for Bi_2Te_3 by Zhang *et al.*[69] and Alpichshev *et al.*[108]. Note that this suppression only holds while the impurities preserve TRS. Magnetic impurities can change the phase difference between incident and scattered electrons, and therefore induce backscattering, as demonstrated by Okada *et. al.*[70]. The absence of backscattering makes the spin-polarized SSs of TMs viable candidates for spintronics applications.

3.4 Phenomenological $k \cdot p$ Model of Topological Surface States

In the presence of TRS, SSs at a given energy form Kramers doublets $(\vec{k}_\uparrow, -\vec{k}_\downarrow)$. The Dirac cone is thus helical, and spin $\vec{\sigma}$ and momentum $\vec{k}$ are locked in the $x - y$ plane. For a mirror plane surface state, the Hamiltonian reads[87]:

$$\mathcal{H}_{SS} \propto v_F \left(\vec{k} \times \vec{\sigma} \right) \tag{3.1}$$

The spin-resolved ARPES measurements on Bi_2Se_3 indeeed show an isotropic (circular) FS, which is spin-polarized, in agreement with Eqn. 3.1, leading to a geometric Berry's phase of π[100]. Note that this ideal single Dirac cone band structure corresponding to linear dispersion ($\varepsilon(k) =$
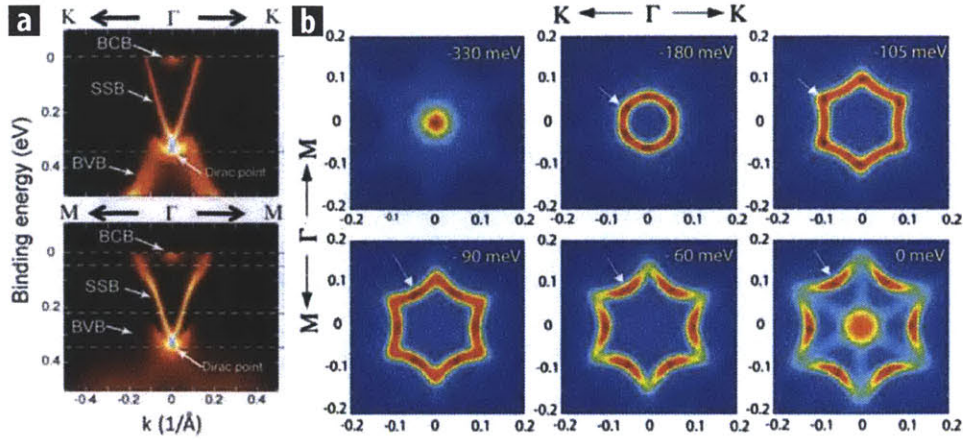
Figure 3-8: ARPES on Bi$_2$Te$_3$: Hexagonal Warping. (a) ARPES measurements of the SS dispersion on the TM Bi$_2$Te$_3$ (adapted from [106]). Note the slight difference between the $\Gamma - K$ (top) and $\Gamma - M$ (bottom) dispersions, the latter noticeably deviating from linearity away from the Dirac point (DP). (b) ARPES measurements of the CECs of the TM Bi$_2$Te$_3$ at energies increasingly away from the DP ($\varepsilon_D = -330$ mV) (adapted from [108]). The CECs evolve gradually from being isotropic (circular), to a hexagon, and subsequently to a hexagram, or snowflake shape for $\varepsilon - \varepsilon_D > 200$ mV.

$\hbar v_F k$)[100], is similar to the case of single-layer graphene[109].

In contrast, corresponding measurements of the SS band structure of Bi$_2$Te$_3$ (Fig. 3-8a) yielded slightly different results. Chen *et al.*[106, 108] found that at energies ε significantly above the Dirac point (DP) ε_D, the constant energy contours (CECs) of Bi$_2$Te$_3$ are no longer circular. The CECs warp to become hexagonal at intermediate energies ($\varepsilon - \varepsilon_D > 150$ mV) and hexagram, or snowflake like ($\varepsilon - \varepsilon_D > 200$ mV), at even higher energies (Fig. 3-8b). This hexagonal warping was further proposed as the explanation for the scattering modes observed in the spectroscopic STM measurements on Bi$_2$Te$_3$[69, 108].

The FS deformation was explained by Liang Fu using a phenomenological $k \cdot p$ approximation[1] about the Γ-point, with addition of a warping term to the SS Hamiltonian[110] that introduces $x-y$ anistropy. The isotropic SS Hamiltonian in Eqn. 3.1, the starting point for the model, can be written as

$$\mathcal{H}_0 \propto v_F \left(k_x \sigma_y - k_y \sigma_x \right) \tag{3.2}$$

Noting that the topological SS Hamiltonian still has to obey the $\mathbb{C}_3$ crystal symmetry and TRS, the next order terms correspond to a correction of the Dirac velocity, $v(k) = v_F \left(1 + \alpha' k^2 \right)$; a mass term to introduce particle-hole anisotropy, $\mathcal{H}_m = k^2/2m$; and a warping term, $\mathcal{H}_w = \lambda_w (k_+^3 + k_-^3) \sigma_z$[110]. This introduces the following material parameters: α', corresponding to the Rashba

---

[1]$k \cdot p$ theory is a perturbative low momentum approximation used to calculate the band structure of semiconducting materials[55].

SOC interaction; m, the band mass; and λ_w, the warping strength. Note that the corrections stated above are cubic in $k_{x,y,z}$ in accordance with TRS, apart from the k^2 term, which does not break TRS either. Furthermore, the warping term, $\mathcal{H}_w$, has the underlying $\mathbb{C}_3$ crystal symmetry, and uniquely introduces the $x - y$ anisotropy that we require. The resulting Hamiltonian, to cubic order, is[110]:

$$\mathcal{H}_{k\cdot p} \equiv \frac{k^2}{2m} + v_F \left(1 + \alpha' k^2\right) \left(k_x \sigma_y - k_y \sigma_x\right) + \lambda_w (k_+^3 + k_-^3)\sigma_z \qquad (3.3)$$

By diagonalizing Eqn. 3.3, the SS dispersion, to cubic order, is found to be[110]:

$$\varepsilon_{\pm}(\vec{k}) \equiv \frac{k^2}{2m} \pm \sqrt{v_F^2 \left(1 + \alpha' k^2\right) k^2 + \lambda_w^2 k^6 \cos^2(3\theta)} \qquad (3.4)$$

Thus the SS dispersion can be thought to form two 'cones' correpsonding to $\varepsilon_{\pm}(k)$, where θ is the angle with respect to the x-axis in k-space ($\Gamma - K$). The band structure has six-fold symmetry, due to the $\mathbb{C}_3$ symmetry of the $\cos^2(3\theta)$ term, and TRS. A contour plot of Eqn. 3.4, shown in Fig. 3-9e, was found to be quantitatively consistent with the CEC evolution of Bi_2Te_3 for $\varepsilon > \varepsilon_D$[110]. Finally, since $\mathcal{H}_w$ couples to σ_z, we expect some out-of-plane spin polarization at large enough energies $(\varepsilon - \varepsilon_D)^2$. This out-of-plane spin texture of Bi_2Se_3 was measured using circular dichroism ARPES[111], following the observation of similar hexagonal deformation of CECs in this TM[112].

The phenomenological $k \cdot p$ model for topological SS developed by Fu originates from a linearly dispersing Dirac cone. However, we can use the same $k \cdot p$ model to visualize the emergence of the SS Dirac cone from conventional electrons in the following manner (Fig. 3-9a-d). We start with a parabolic dispersion, corresponding to free electrons with mass m and degenerate spins: $\varepsilon(k) = k^2/2m$ (Fig. 3-9a). The inversion symmetry of the crystal is broken at the surface, and this would generate Rashba SOC for the two separate spin channels[113], resulting in Rashba-split parabolas, described as:

$$\varepsilon_{\pm}^R(k) \equiv \frac{k^2}{2m} \pm \alpha_R k \qquad (3.5)$$

The Rashba split bands of the form shown in Fig. 3-9b, are observed on the surface of several metals, e.g. Au(111) or Bi(111)[114, 115]. In this case the SS do have spin texture, but are connected in the manner similar to Fig. 3-4c. Topological SSs are simplistically required to connect the valence and conduction bands, and therefore the outer 'cone' in Fig. 3-9b needs to fold down. This can be accomplished by forcing the outer cone to fold down at large momenta (as in Fig. 3-9c), by adding a k^3 correction to the Rashba parameter:

---

[2]The z spin polarization, $\langle \sigma_z \rangle$, has a periodicity of $\cos(3\theta)$ around the CEC.
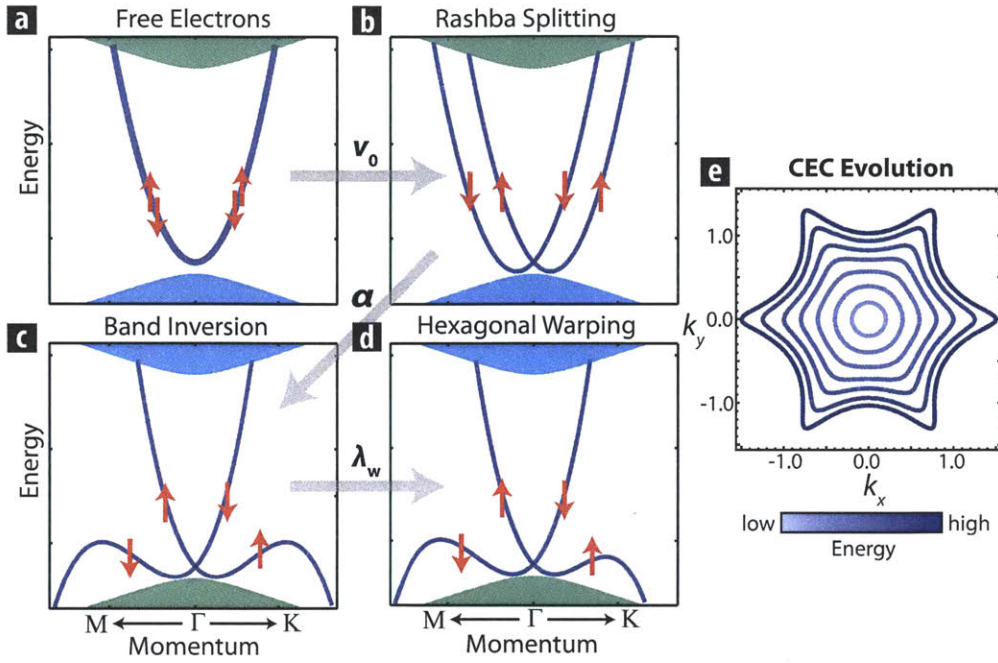
Figure 3-9: $k.p$ **Theory and Surface State Band Structure. (a–d)** A schematic description of the emergence of topological SSs from conventional parabolic dispersion, using the Fu $k \cdot p$ model[110]. The parabolic dispersion in (a) is split by Rashba SOC in (b), with splitting strength v_0. The Rashba SSs on the outer cone can be folded downwards by adding a cubic velocity correction (Eqn. 3.6) (c), with the resulting disperser corresponding in principle to topological SSs. Hexagonal warping can introduce anisotropy between the dispersions along the $\Gamma - K$ and $\Gamma - M$ directions.

$$\varepsilon_{\pm}^{\mathrm{TSS}}(k) \equiv \frac{k^2}{2m} \pm \alpha_{\mathrm{R}} k \sqrt{1 + \alpha' k^2} \tag{3.6}$$

The SS band structure thus generated (Fig. 3-9c) could in principle correspond to topological SS. The addition of a warping term defined by Fu[110] results in a dispersion similar to Eqn. 3.4:

$$\varepsilon_{\pm}^{\mathrm{TSS,W}}(k) \equiv \frac{k^2}{2m} \pm \alpha_{\mathrm{R}} k \sqrt{1 + \alpha' k^2 + \lambda_{\mathrm{w}}^2 k^6 \cos^2(3\theta)} \tag{3.7}$$

We will use this phenomenological $k \cdot p$ description in the following chapters to understand and quantify our STM measurements of the topological SS of Sb(111).

3.5 Towards Better Topological Materials

The Bi_2X_3 (X = Se, Te) class of TMs have been extensively studied over the past few years using numerous experimental and theoretical techniques. The spectroscopic investigation of SS band structure, using ARPES, and scattering signatures, using STM, have been detailed in § 3.3.2–§ 3.4.

Measurements of quantum oscillations in these materials at high magnetic fields do show signatures of SS Landau quantization[116, 117], as do STM measurements of Landau quantization in these materials[56, 61]. Transport techniques have also reported the observation of weak antilocalization[118], conductance fluctuation[119], and ambipolar transport[12] phenomena associated with SSs. Furthermore, transport and spectroscopic measurements using optical techniques have reported the coupling of light polarization with the spin of SS[120, 121]. Substantial progress has also been made with the growth of TM thin films using molecular beam epitaxy (MBE), by demonstrating the thickness limit of TMs[122, 123] and the demonstration of anomalous phenomena associated with topological SS[124–126].

3.5.1 Topological Materials and Growth Issues
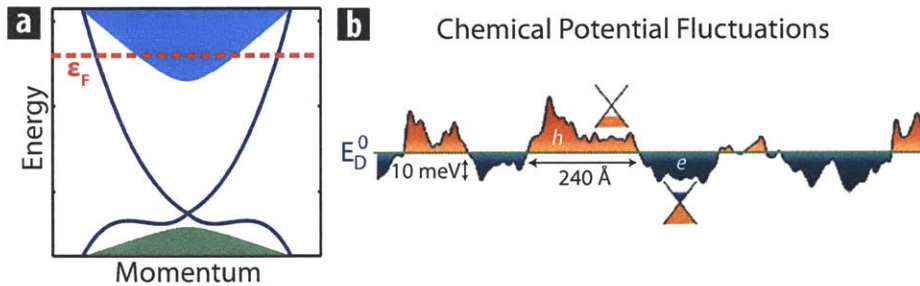
Figure 3-10: Present Limitations of Topological Materials. (a) Band structure schematic of an undoped TM, showing the Fermi energy, ε_F, to be pinned to the valence band, attributed to growth defects. **(b)** The typical chemical potential landscape of the Bi_2X_3 (X = Se, Te) class of TMs, chemically doped (1-3%, substitutional) to pin ε_F in the bulk band gap. The chemical potential fluctuates by tens of mV, and corresponds to a SS mean free path of ~ 25 nm (adapted from [23]).

Despite the progress in the investigation of SSs, the main focus in experimental TM research continues to be towards developing better TMs. The reasons for this are twofold.

First, in undoped Bi_2X_3 TMs, ε_F is typically pinned within the bulk bands (e.g. Fig. 3-10a). As a result, the contribution of SSs to transport measurements is ~ $5 - 10\%$, amidst a strong bulk background[119]. The origin of this phenomenon has been attributed to intrinsic defects and vacancies originating during the growth process. Intensive modification of growth recipes for undoped TMs have not succeeded in substantially increasing the SS contribution to transport measurements[12, 118].

Second, while the chemical potential of Bi_2X_3 can be tuned into the band gap by substitutional doping, e.g. Ca, Cu etc. at the Bi site; or e.g. As at the X site – this introduces a separate set of problems. STM studies by Beidenkopf *et al.* have shown Bi_2X_3 compounds to have poor screening characteristics. The chemical potential landscape created by bulk dopants is unscreened over several nanometers, introducing potential fluctuations of tens of mV on the nanometer length scale[23]. This severely restricts the mean free path in doped TMs to e.g. ~ $20 - 30$ nm[23]. Additional complications are introduced by band bending phenomena found to occur at the surface[100]. These

phenomena result in the spectral coexistence of topological SSs with a Rashba 2DEG created at the surface[127–129], and the interaction between these two 2D systems is still a subject of debate[130].

To circumvent these issues, considerable effort has been devoted to the synthesis of ternary and quarternary TMs, which have shown up to 60% SS contribution to transport measurements[131, 132]. However, these materials are tuned off-stoichiometry to achive bulk insulating behavior. The corresponding effects on the mean free path of SSs continues to be investigated[131].

While the eventual objective of achieving dissipationless SS transport remains achievable, it is clear that local, surface-sensitive spectroscopic tools such as ARPES and STM would play a key role towards understanding SS physics and guiding TM development.

3.5.2 Spintronics Metrics of Topological Materials
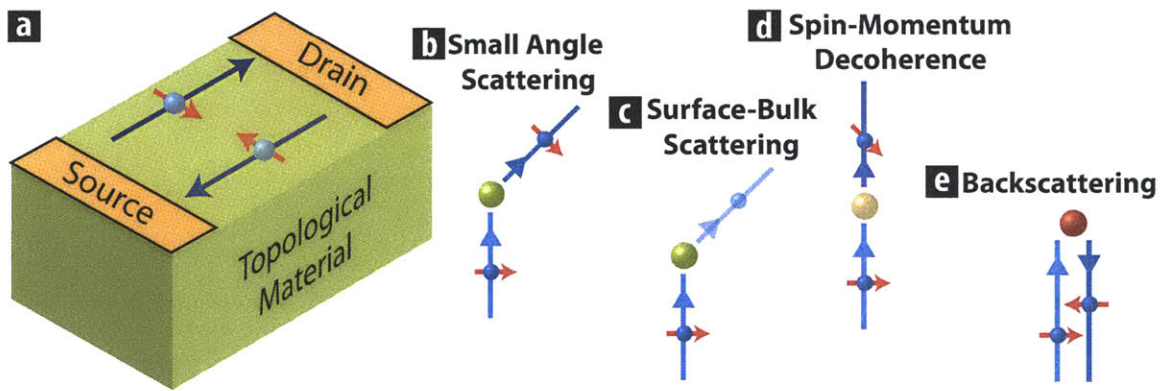
Figure 3-11: Spintronics Metrics for Topological Materials. (a) A cartoon depiction of a spin transport device fabricated on a TM. Counterpropogating SSs could potentially transfer a pure, ballistic spin current from source to drain. **(b-e)** Scattering mechanisms which can limit the efficacy of SSs towards spin transport applications, corresponding to elastic, small angle scattering (b), scattering from the surface to the bulk (c), decoherence of the spin-momentum locking (d) and backscattering from magnetic impurities (e).

As outlined in § 3.3.2–§ 3.4, SSs on TMs are spin-momentum locked, protected from backscattering, and cannot be gapped out by external TRS-preserving perturbations. Notably the spin polarization of the FS has been found to persist up to room temperature in the Bi_2X_3 class[100]. Therefore, these spin-polarized SSs can potentially be used for dissipationless spin transport. A schematic of such a potential device, shown in Fig. 3-11a, would have counterpropagating spin-polarized SSs - with the spin-momentum locking ensuring a pure, ballistic spin current with zero charge current. To develop TMs towards spintronics applications, we look at the various mechanism that can affect the SS spin current, and suggest means to quantify the relevant SS properties.

First, we note that while the spin-textured SSs are not allowed to backscatter, small-angle scattering off non-magnetic impurities is allowed (Fig. 3-11b). Another allowed mechanism is the scattering of SSs into spectrally coexisting bulk states (Fig. 3-11c). In fact, surface-bulk scattering in Bi_2Se_3 has been suggested as the mechanism responsible for static interference patterns below

ε_D - at the onset of the valence band[133], and for the suppression of Landau quantization at the onset of the conduction band[56]. Both these mechanism could cause dissipation and could heat up the spin device. The upper limit of the sum total of these scattering mechanisms can be quantified by the SS *mean free path*, λ_f[3]. Second, the spin current signal could also be diminished by the decoherence of spin-momentum locking (Fig. 3-11d), thereby providing a spurious spin current for a net zero charge current. We note from § 3.4 that the strength of spin-momentum locking is quantified by the Rashba parameter, α_R. Finally, the topological protection of SSs is absent when TRS is broken, e.g. in the presence of magnetic impurities, which can cause backscattering (Fig. 3-11e). In such a scenario, the SS response to the magnetic perturbations is quantified by the g-factor. For strong immunity to magnetic perturbations, a small value of the g-factor is desirable.

Using these metrics as a starting point, we can quantify the utility of TMs for spintronics applications. Further, we will quantify the band structure of Sb(111) using momentum-resolved STM and determine the relevant set of metrics for this material.

---

[3]Strictly speaking, this should be $\lambda_f^{\text{transport}}$, as the mean free path measured from say tunneling could be affected by, for example, collective modes. However, $\lambda_f^{\text{tunneling}}$ does place an upper bound on $\lambda_f^{\text{transport}}$.

Chapter 4

Spectroscopic STM Studies of the Topological Surface States on Sb(111)

Here we report on our spectroscopic STM studies of the cleaved (111) surface of the topological semimetal Sb. We first detail the topographic and spectroscopic characterization of the surface, and subsequently report on the simultaneous observation of Landau quantization and quasiparticle interference phenomena, associated with the topological surface states of this material, over a 300 meV energy range.

4.1   Experimental Techniques and Characterization

Single crystals of Sb were grown using the following method[99]. High-purity antimony (99.999%, supplied by Alfa Aesar® in shot form (10.15 g, 6 mm) was sealed in an evacuated quartz tube, and heated in a box furnace to 700 °C for 24 hours. The furnace was cooled slowly (0.1 °C/min) to 500 °C, and subsequently cooled to room temperature.

Our measurements were performed using a home-built STM at liquid helium temperatures. Single crystals of Sb were cleaved in-situ in cryogenic ultrahigh-vacuum to expose the (111) face, and inserted into the STM. Mechanically cut Pt-Ir tips, cleaned by field emission and characterized on gold, were used for the measurements. Spectroscopy data were acquired using a lock-in technique at 1.115 kHz, and conductance maps were obtained by recording out-of-feedback dI/dV spectra at each spatial location. Three single crystal samples of Sb(111) were investigated in this work, and their correspondence to the data shown in the manuscript is detailed in Tbl. 4.1.

Figure		Sample
4-1	a	3
4-2	a	3
	b, c	1
4-4	a	1
4-6, 4-7	all	1
4-8, 4-10	all	2
4-9	a, b	1, 2
4-11	all	3
4-12, 4-13, 4-14, 4-15	all	1

Table 4.1: Sample Tabulation. A tabulation of the samples investigated in this work, and their correspondence to the data shown in the manuscript. The chemical potential varied between samples by up to 15 mV, and dispersions varied by up to 5%.
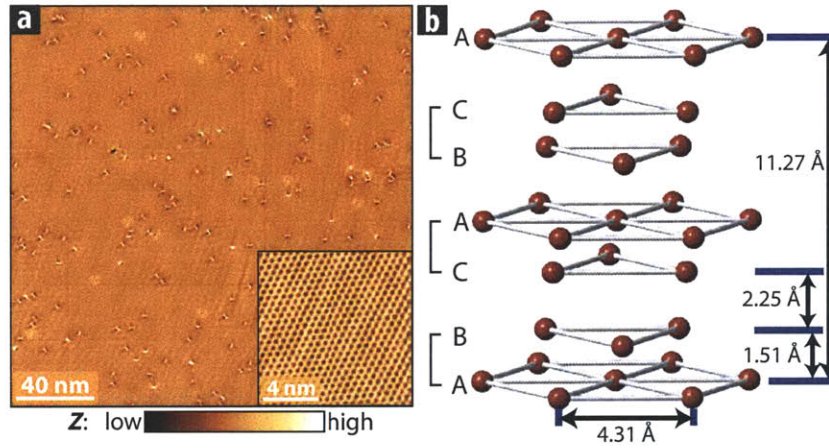
Figure 4-1: Topography and Crystal Structure of Sb(111). **(a)** STM topograph of Sb(111) showing an atomically flat surface. Setpoint parameters: sample bias, $V_0 = +200\,\mathrm{mV}$; junction resistance, $R_J = 10\ \mathrm{G\Omega}$. Inset shows the atomically resolved hexagonal lattice ($V_0 = +200\,\mathrm{mV}$; $R_J = 125\ M\Omega$). **(b)** The layered hexagonal structure of Sb(111), with the unit cell consisting of three bilayers.

4.1.1 Topographic Characterization of the Surface

Sb(111) has a layered hexagonal structure and R_{mh}^3 space group symmetry (space group no. 166). The unit cell (Fig. 4-1b) consists of three bilayers of Sb atoms, with lattice constants $a_0 = 4.31$ Å (in-plane) and $c = 11.27$ Å (out-of-plane). The crystal typically cleaves between the weakly coupled bilayers shown in Fig. 4-1b.

The (111) surface of Sb shows large atomically flat regions and atomic steps (Fig. 4-1a, Fig. 4-2), free from modulations associated with electronic inhomogeneity, except in the immediate vicinity of sparse single atom surface impurities. The surface displays a hexagonal lattice with the expected periodicity. The magnitude of atomic corrugations on Sb(111) is much lower than in semiconducting TMs due to screening effects from bulk bands, detailed further in § 4.1.2.
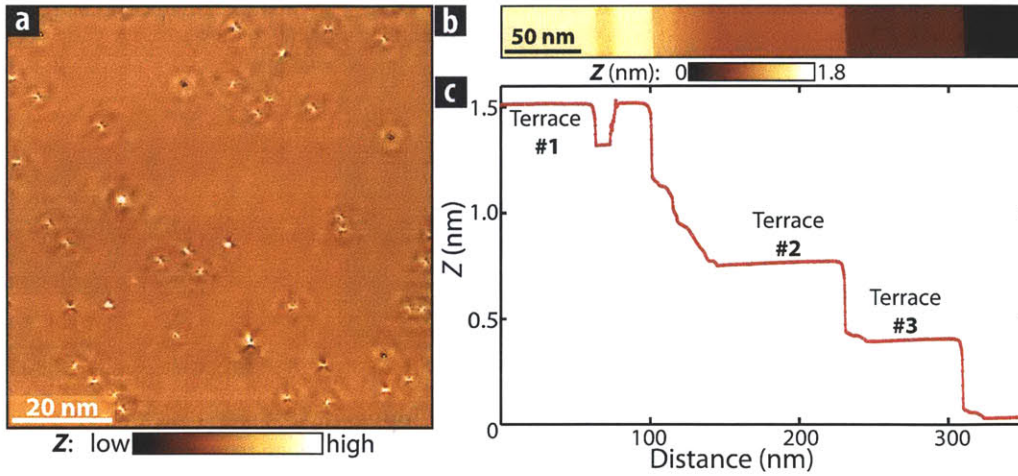
Figure 4-2: Prominent Topographic Features on the Sb(111) Surface: Impurities and Atomic Steps. (a) A topograph acquired over part of the field-of-view shown in Fig. 4-2a. Topographic variations seen over this field-of-view are associated with single-atom impurities, with no visible nanometer-scale potential fluctuations. **(b)** Topograph showing of a series of atomically flat terraces on Sb(111), perpendicular to the Bragg $(\Gamma - M)$ direction $(V_0 = +200 \, \mathrm{mV}; R_J = 10 \, \mathrm{G}\Omega)$. **(c)** A linecut through the topograph in (b), perpendicular to the terraces.

Fig. 4-2 shows in more detail the observed topographic features on the Sb surface. In Fig. 4-2a, we note the presence of two distinct kinds of single-atom impurities, one of which breaks the $\mathbb{C}_6$ symmetry of the lattice. Neither of these two kinds of impurities have been reported in STM studies of other TMs[14, 56, 134]. The presence of a third kind of impurity is noted in Fig. 4-1a, which is more similar to conventional impurities reported in other TMs[14, 56, 134]. Over flat regions of the sample, any modulations in the topographs (Fig. 4-1a, Fig. 4-2a) correspond directly to visible impurities on the surface. These impurities do not noticeably change the local chemical potential, but do scatter surface state quasiparticles to generate quasiparticle interference (QPI) patterns, detailed in § 4.3.

The other prominent topographic feature is associated with the presence of atomic steps. Some regions of the Sb(111) surface consist of several atomic terraces formed perpendicular to the Bragg $(\Gamma - M)$ direction, shown in Fig. 4-2b. The step height between adjacent terraces is ~ 0.38 nm (Fig. 4-2c), consistent with the expected bilayer spacing (Fig. 4-1b). The effects of scattering and transmission through these steps has been explored in detailed in the previous work of Seo *et al.*[135], and is also examined in § 4.4.

The comparison between topographs acquired on Sb with those reported on other TMs (Fig. 4-3) is rather striking. All these material surfaces have a hexagonal lattice, and therefore the structural contribution of the lattice to the topographs is nominally similar. However, the electronic contribution to the STM topograph, appearing as a result of the second term in Eqn. 2.5, are markedly different between Sb and other TMs. Notable in the Bi_2X_3 TMs (Fig. 4-3b-c) and com-
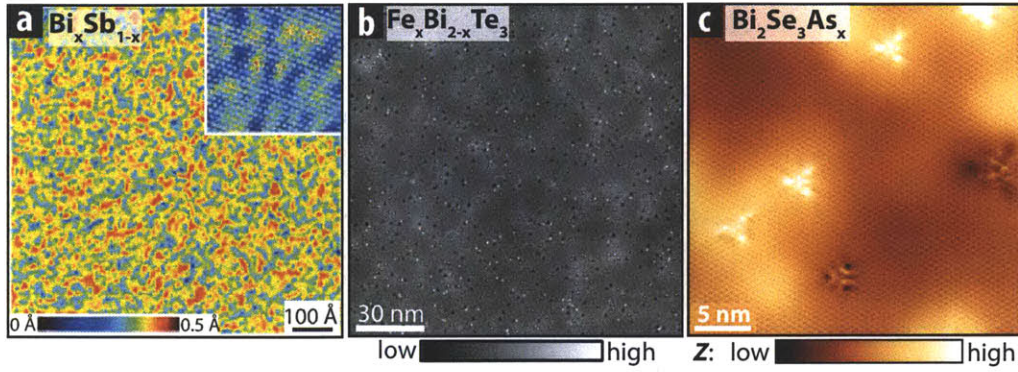
Figure 4-3: Representative Topographs of Other Hexagonal Topological Materials. (a-c) STM Topographs acquired on the TMs Bi_xSb_{1-x} (a, adapted from [68]), Bi_2Te_3 (b, adapted from [70]), and $Bi_2Se_3As_x$ (c). All three topographs show nanometer lengthscale modulations attributed to fluctuations of the chemical potential[23].

pletely dominating the topographic measurements in Bi_xSb_{1-x} (Fig. 4-3a) is the electronic inhomogeneity, understood to be associated with poorly screened bulk dopants and defects[23]. The contrasting topographs imaged on Sb suggest that the chemical potential on the surface of Sb(111) is homogeneous in comparison to other TMs, a fact which is detailed quantitatively in § 5.3.3. This homogeneity is associated with the presence of bulk bands proximate to the surface states, as detailed in the following section.

4.1.2 Surface State Band Structure and DOS Spectroscopy
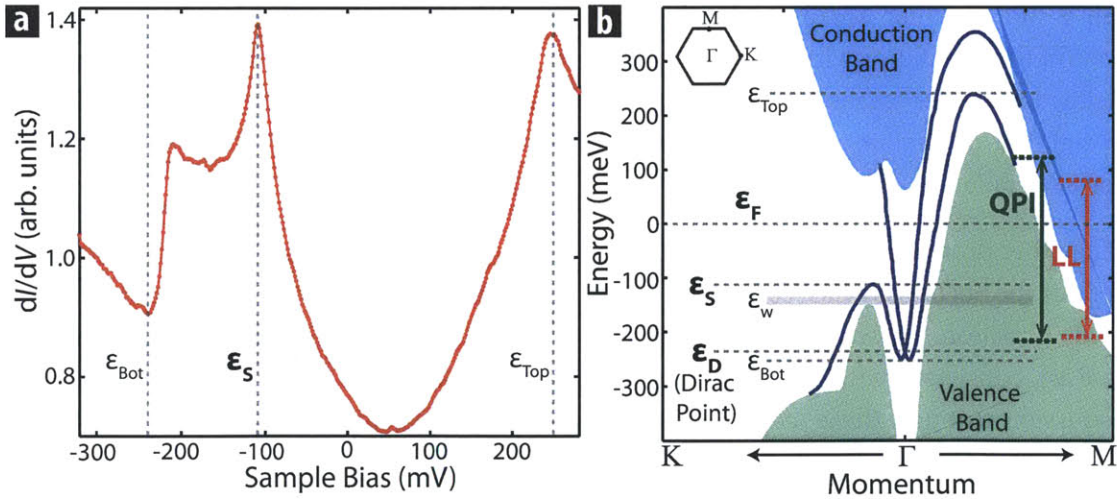
Figure 4-4: Spectroscopy and Band Structure of Sb(111). (a) A typical dI/dV spectrum on Sb(111), with cusp-like features at ε_{Bot}, ε_S, and ε_{Top}, corresponding to extremal features in the SS band structure defined in (b) ($V_0 = +300\,mV$; $R_J = 500\,M\Omega$; $V_{mod} = 3\,mV$). **(b)** Schematic band structure of the semimetal Sb(111) with topological surface states (dark blue) intersecting at the Dirac point, ε_D. The SS connect the bulk valence (green) and conduction (cyan) bands. Extremal band features ε_{Bot}, ε_S, and ε_{Top} are labeled. The spectral range of the observed LLs and QPI is indicated.

Energy Scale	First Usage	Definition
ε_{Bot}	Fig. 4-4b	Bottom SS band edge
ε_D	Fig. 4-4b	Dirac point (intersection of SSs)
ε_w	Fig. 4-4b	Warping energy for outer SS band
ε_S	Fig. 4-4b	Saddle Point: $\Gamma - K$ turnover of outer SS band
ε_F	Fig. 4-4b	Fermi energy
ε_{Top}	Fig. 4-4b	Top SS Band Edge: $\Gamma - M$ turnover of outer SS band
ε_n	Eqn. 4.3	Semiclassical LL energy (Dirac or Rashba formulas)
ε_N	Fig. 4-7	Empirically measured LL peak energies
$\varepsilon_{int,D}$	Fig. 4-10b	Intercept of Semiclassical Dirac LLs ($\sqrt{B}$-fit)
$\varepsilon_{int,R}$	Fig. 4-10c	Intercept of lowest Rashba-like LLs (B-linear fit)

Table 4.2: Energy Scales. A tabulation of the important energy scales of Sb(111) surface states used in this work. Note that the absolute values of these energies vary by up to 15 mV between samples.

The typical dI/dV spectrum acquired on Sb is shown inFig. 4-4a. While the spectrum is expected to be representative of the DOS, it would have contributions from both the surface and bulk bands. In particular, we note the presence of prominent cusp-like features in the spectrum. To understand the origin of these features and the shape of the spectrum, we turn to a schematic of the Sb band structure, shown in Fig. 4-4b. This schematic is obtained from first principles calculations, which qualitatively reproduce the band features.

Unlike Bi_2X_3 and Bi_xSb_{1-x} ($x < 0.2$) TMs, which have a bulk band gap, Sb is a semimetal with a negative band gap[136]. As can be seen in Fig. 4-4b, the bulk valence and conduction bands overlap for > 300 mV. Notably, the bulk band structure of Sb does have the topological invariant, $\nu_0 = 1$, and therefore the bulk bands near ε_F are inverted. This necessitates the existence of topological SSs (blue lines in Fig. 4-4b) that connect the valence and conduction bands. However, the peculiar bulk band structure of Sb results in the SS bands deviating markedly from the ideal Dirac cone structure observed in Bi_2Se_3 and Sb_2Te_3. The energy scales referred to in this work are detailed, along with their definitions, in Tbl. 4.2.

The SSs band structure near the Γ-point appears similar to that of Rashba SOC split parabolas (e.g. Fig. 3-9b) with a lower band edge at ε_{Bot}. They cross at Γ to define the Dirac point ε_D, with the crossing protected by Kramers theorem in the presence of time-reversal symmetry (§ 3.3.1). However, unlike typical Rashba SSs, the topological nature of Sb SS requires the outer Rashba cone to turn down and connect to the valence band (e.g. Fig. 3-9c). This results in the formation of extremal features in the outer Rashba cone, one of which is a *saddle point* (ε_S), and the other is a band edge (ε_{Top}). The asymmetry between these two features can be described by the presence of hexagonal warping, as detailed in § 3.4. The energy ε_w corresponds to the onset of noticeable warping on the outer Rashba cone.

Therefore, the cusp-like features in the dI/dV spectrum (Fig. 4-4a) can be well-explained by the extrema in the SS band structure (Fig. 4-4b). The steps in conductance at ~ -240 mV and

~ 270 mV are associated with 2D band edges - ε_{Bot} and ε_{Top} respectively. The sharp peak at -110 mV corresponds to the logarithmic singularity associated with the 2D saddle point at ε_S. We note in particular the importance of this saddle point, which signifies a crossover between the appearance of the SS bands as Rashba-split parabolas (below ε_S) to an isolated Dirac cone (above ε_S).
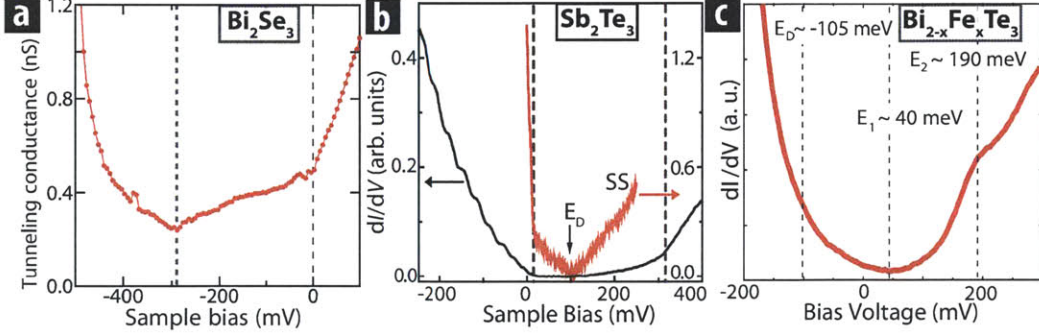
Figure 4-5: Representative STM Spectra on other TMs. (a–c) Representative STM spectra acquired on the TMs Bi_2Se_3 (adapted from [56]), Sb_2Te_3 (adapted from [123]), and Bi_2Te_3 (adapted from [70]). Note that in (a-b), the DP directly corresponds to the spectral minimum, while in (c), only SS band edge features can be identified, as in the case of Sb(111).

Finally, we highlight the absence of a conductance minimum associated with the Dirac point in Sb. Direct spectroscopic access to the DP is precluded due its spectral coincidence with other SSs and bulk bands. This is in marked contrast to the STM spectra acquired on TMs Bi_2Se_3 and Sb_2Te_3 (Fig. 4-5a-b, [56, 123]), where the bulk band gap and conventional Dirac cone structure results in a spectral minimum at ε_D. The spectra in Sb are similar to those observed on Bi_2Te_3, with prominent SS band edges. While the absence of direct access to the DP is a limitation, the presence of a bulk band continuum proves to be a distinct advantage in Sb(111), screening out tip-induced band bending artifacts[137] and chemical potential fluctuations[23, 68].

4.2 Landau Quantization of Sb(111) Surface States

In the presence of perpendicular magnetic fields above 4 T, conductance oscillations corresponding to quantized Landau levels (LLs) were observed in dI/dV spectra on Sb(111) (Fig. 4-6). The LLs emerge as modulations on top of the background (zero field) spectrum. We note that the LLs are unequally spaced in energy, as expected for Dirac fermion surface states, and are sharpest at ε_F, evincing lifetime broadening. We observe up to 27 such LL oscillations – more than the number reported in any other TM[56, 70, 123, 137], despite the presence of bulk bands throughout this energy range (Fig. 4-4b).
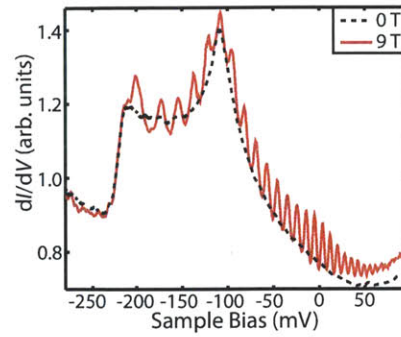
Figure 4-6: Landau Quantized STM Spectrum. Representative dI/dV spectrum acquired in a 9 T magnetic field (red), compared with the zero field spectrum (dashed black). The oscillations in the 9 T spectrum correspond to quantized Landau levels. Setpoint Parameters: $V_0 = +100$ mV; $R_J = 0.2$ GΩ; $V_{mod} = 0.4$ mV.

4.2.1 Normalization and Fitting of Landau Quantized STM Spectra
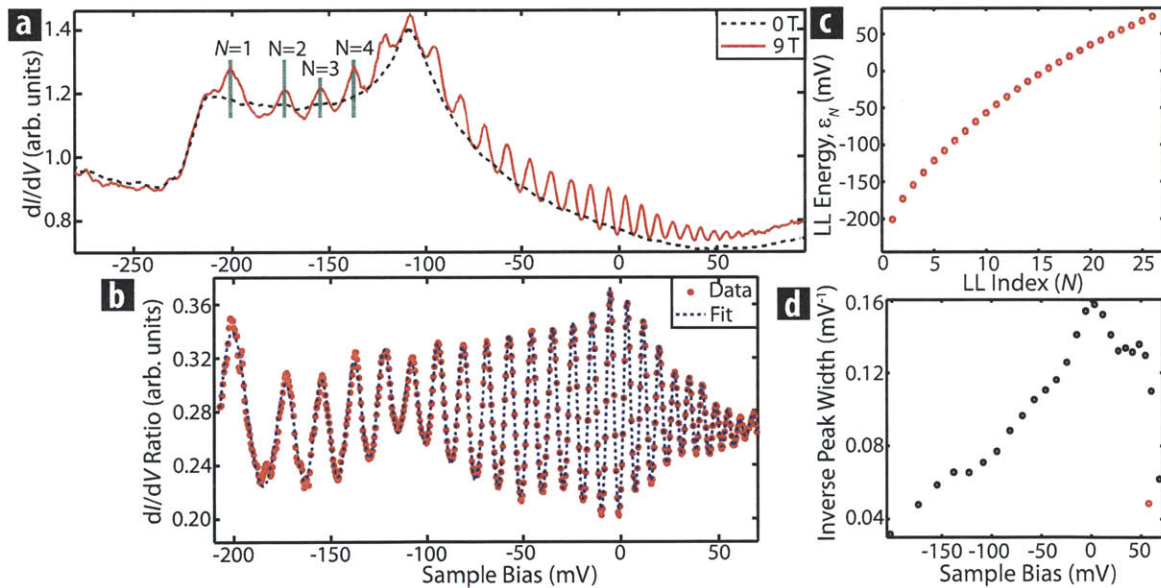
Figure 4-7: Normalization and Fitting of Landau Quantized STM Spectra. **(a)** Representative dI/dV point spectrum acquired in a 9 T magnetic field (red), compared with zero field point spectrum (dashed black). The two spectra were acquired within 5 nm of each other (identical data to Fig. 4-6). The green lines indicate the first few empirically identified LL indices. Setpoint parameters: $V_0 = +100$ mV ; $R_J = 0.1$ GΩ, $V_{mod} = 0.4$ mV. **(b)** The 9 T spectrum in (a) is divided by the 0 T spectrum to remove the bulk background, and a weak quadratic background (likely due to tip drift effects) is subtracted from the ratio, resulting in the normalized data shown as red dots. The data is fit to a sum of Lorentzian peak profiles over the range of observed LLs (dashed blue line). **(c)** The peak positions of the observed LL indices, N, extracted from the Lorentzian fit in (b). **(d)** The peak widths of the observed LL indices, N, extracted from the Lorentzian fit in (b).

We assign empirical indices starting with $N = 1$ to all such B-dependent LL peaks (Fig. 4-7a). Employing a polynomial background subtraction on the dI/dV spectrum acquired in field[56, 61] was not found to be sufficient for analyzing the LLs in Sb(111), due to the due to the prominent cusps in the conductance background generated by the SS extrema (Fig. 4-4), which cannot be removed by this process. The LL dispersion was therefore analyzed by normalizing the point spectrum acquired in field to that acquired at zero field – within 5 nm of each other. The spectra were recorded sufficiently far from impurities, which may introduce artifacts (Fig. 5-8). After the normalization, a weak quadratic background was subtracted from the ratio, resulting in the data shown in Fig. 4-7b. This weak background likely arises from tip drift effects in the z-direction over the ~ 10 s data acquisition process. While peak-like features were occasionally observed in the normalized spectrum at energies below the $N = 1$ LL that could in principle correspond to lower LLs, these could not be consistently reproduced.

To extract the positions and widths of the LLs, in order to analyze the LL dispersion, the data in Fig. 4-7a was fit to a sum of Lorentzian peak profiles, given by:

$$G_{\text{fit}}(\varepsilon) = y_0 + \sum_{i=N_{\text{min}}}^{i=N_{\text{max}}} \frac{2A_i}{\pi} \cdot \frac{w_i}{4(\varepsilon - \varepsilon_{c,i})^2 + w_i^2} \tag{4.1}$$

Here, N_{min} and N_{max} correspond to the indices of the lowest and highest observed LLs. The full spectrum is fit simultaneously using the following parameters – an overall offset y_0, and three independent parameters for each LL: center ε_c, width w, and amplitude A. The quality of the Lorentzian sum fit is shown in Fig. 4-7b.

The energies of the LL peaks, ε_N, thus determined, are plotted against the empirical LL index, N Fig. 4-7d. Meanwhile the set of Lorentzian fit parameters w_i correspond directly to the inverse LL widths plotted in Fig. 4-7d.

4.2.2 Magnetic Field Dependence and Landau Level Index Identification

LLs correspond to quantized orbits in real, as well as momentum space. Therefore, the energy-momentum Landau quantization can be used to measure the quasiparticle band structure corresponding to the LLs. To do so, we note that, as detailed in § 2.3, the semiclassical Bohr-Sommerfeld quantization relation gives the area in k-space for the nth LL[56] to be

$$A_n = \pi q_n^2 \equiv (n + \gamma) \cdot 2\pi e B/\hbar \tag{4.2}$$

The factor γ, determined by the Berry's phase of the quasiparticle, is $1/2$ for a free electron and 0 for a Dirac fermion[56]. For the surface states of Sb(111), the measured Berry's phase of π would correspond to $\gamma = 0$ (strictly speaking, for $\varepsilon > \varepsilon_S$)[99]. It remains to determine the offset
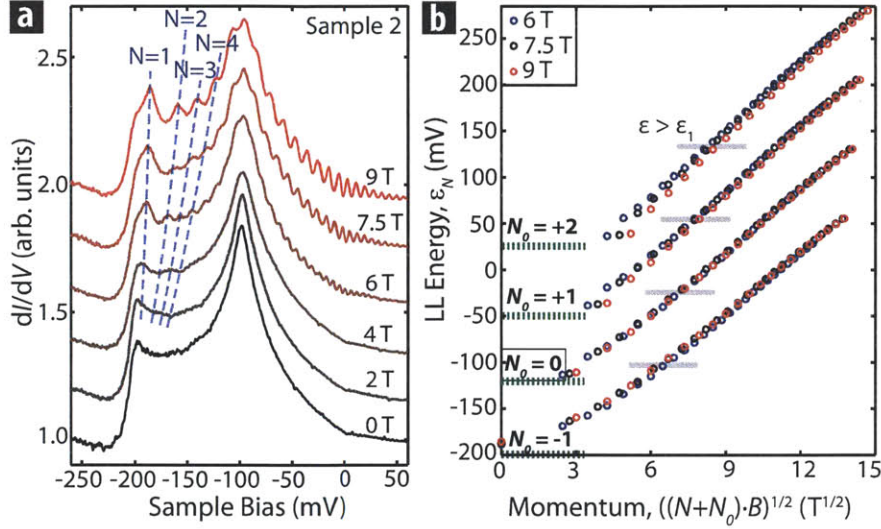
Figure 4-8: Magnetic Field Dependendence and Index Identification of Landau Levels. (a) B-dependence of LLs, showing representative dI/dV spectra, vertically offset for clarity. Dashed blue lines are guides to the eye following the first four LLs. Setpoint Parameters: $V_0 = +100\,\mathrm{mV}$; $R_J = 0.1 - 0.2\,\mathrm{G\Omega}$; $V_{\mathrm{mod}} = 0.4\,\mathrm{mV}$. **(b)** The $\varepsilon_N(q_N)$ dispersion of LLs at three representative magnetic fields (from the data in (a)), for different values of the offset parameter N_0, used to define the semiclassical (Bohr-Sommerfeld) momentum for Dirac fermions, $q_N \equiv \sqrt{(N + N_0)\,B}$, where N is the empirically observed LL index. The dispersions have been vertically offset by 75 mV for clarity; horizontal green dashed lines denote the same reference energy for each dispersion. Horizontal gray lines denote ε_S for each dispersion, indicating the energy above which we expect the Dirac dispersion to hold. The offset value $N_0 = 0$ is found to give the best collapse of $\varepsilon_N(q_N)$ spectra for different magnetic fields onto each other, above ε_S.

$N_0 = N - n$ between the empirical index N and the actual semiclassical index n.

To determine N_0, we performed detailed magnetic field dependent measurements from 4–9 T (representative spectra in Fig. 4-8a). Fig. 4-8b shows the $\varepsilon(q)$ LL dispersion obtained for a few values of N_0 using the peak positions at three representative magnetic fields. We find that $N_0 = 0$ gives the best collapse of $\varepsilon_N(q_N)$ values for different magnetic fields in the Dirac regime ($\varepsilon > \varepsilon_S$), confirming that the empirical LL index N is equivalent to the semiclassical LL index n.

4.2.3 Landau Quantization: Dispersion and Lifetime

Fig. 4-9a shows the LL peak energies, ε_N, plotted against the empirical LL momentum, $\sqrt{NB}$ ($N_0 = 0$). For energies $\varepsilon > \varepsilon_S$, the dispersions obtained at different magnetic fields collapse on to a single curve – validating the Dirac fermion semiclassical approximation with $n = N$, and demonstrating that the Landau quantization arises from a single pocket. From Fig. 4-4b, we conclude that the LL wavevector q_N corresponds to the area of the inner Γ-centered pocket. We note that the between the two samples examined in Fig. 4-9a, the chemical potential varies by $\sim 15\,\mathrm{mV}$ and the dispersion by $\sim 5\%$.

The LLs peaks are sharpest around the Fermi energy, ε_F (Fig. 4-6). This is quantified in Fig. 4-
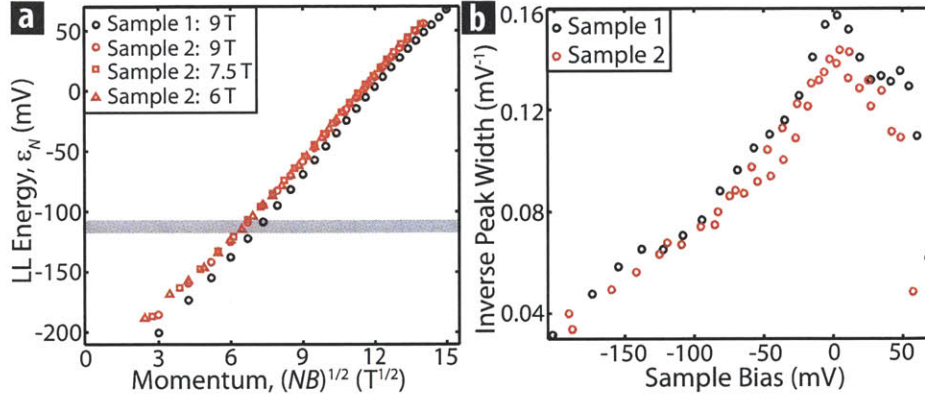
Figure 4-9: Landau Quantization: Dispersion and Lifetime of Surface States. (a) Dispersion of LL energies ε_N vs. momentum $\sqrt{NB}$ for two samples, based on the semiclassical approximation for Dirac fermions. Grey band shows the crossover energy below which the Dirac fermion description breaks down. **(b)** The LL inverse peak widths for two samples, measured using Lorentzian fits (e.g. Fig. 4-7b), showing lifetime broadening away from ε_F.

9b, where the inverse peak width, representative of the quasiparticle lifetime, is peaked at ε_F, and broadens away from it. We note that the energy dependence of the lifetime broadening is monotonic, in contrast to other TMs, where self-energy effects have been suggested to be prominent[56]. Such monotonic lifetime broadening can be well explained within the Fermi liquid picture, where quasiparticles with energy ε away from the Fermi energy decay by creating particle-hole excitations. The phase space of available excitations results in the quasiparticle lifetime having a $1/\varepsilon^2$ energy dependence, which adequately describes our observataions. Finally, the measured lifetime at ε_F ($\sim 0.16 \text{ mV}^{-1}$) corresponds to a mean free path, $l_F \sim 65$ nm, varying by $\sim 20\%$ between two samples, likely due to sample-dependent disorder.

Dirac fermion LLs are unequally spaced in energy, with the dispersion of the nth LL with magnetic field given by

$$\varepsilon_n(B) = \varepsilon_D + v_D \sqrt{2e\hbar nB} \tag{4.3}$$

To quantify the Dirac character of the LLs, we performed detailed magnetic field dependent measurements over 4-9 T on Sample 2. The resulting LL 'fan' plot is shown in Fig. 4-10a.

We fit the field-dependence of the LL dispersion to the form expected for Dirac fermions (Fig. 4-10b):

$$\varepsilon_N(B) = \varepsilon_{\text{int,D}} + v_D \cdot \sqrt{2e\hbar} \cdot \sqrt{NB} \tag{4.4}$$

and to the form expected for conventional fermions (Fig. 4-10c):
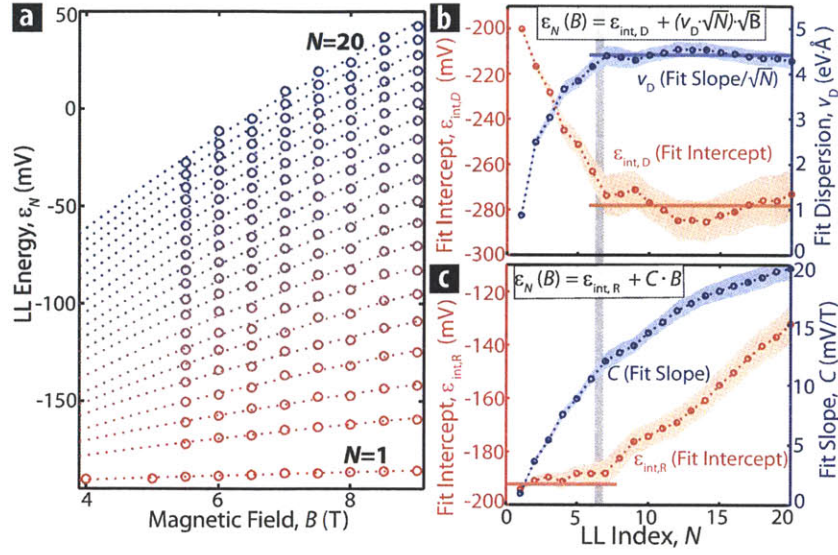
Figure 4-10: Landau Quantization: Quantifying the LL Crossover Behavior. (a) A LL 'fan' plot, showing the measured positions of the first 20 LLs observed for magnetic fields from 4–9 T (identical to Fig. 4-8b). The dotted lines are guides to the eye. **(b-c)** Fits to the LL dispersions in (a) using $\sqrt{B}$-dependence in (b), expected for massless Dirac fermions; and B-linear dependence in (c), expected for massive fermions. The curves show the fit slope and intercept corresponding to each of the LL indices, with the shaded blue and pink regions representing error bars. The data show a crossover, indicated by the vertical grey bar around $N = 6$, from B-linear behavior for $N < 6$ to $\sqrt{B}$-behavior for $N \geq 6$. The values of the parameters v_{D}, $\varepsilon_{\mathrm{int,D}}$, and $\varepsilon_{\mathrm{int,R}}$ determined from the data are indicated by horizontal blue and red lines.

$$\varepsilon_N(B) = \varepsilon_{\mathrm{int,R}} + C \cdot B \tag{4.5}$$

For LL indices $N \geq 6$, the Dirac form fits our data consistently, with intercept $\varepsilon_{\mathrm{int,D}} = -278$ mV, and dispersion $v^* = 4.42$ eV·Å, the latter consistent with the reported ARPES dispersion of the central SS pocket[136]. In contrast for the lower LLs ($N < 6$), the dispersion monotonically deviates from the ideal $\sqrt{B}$-fit, and the dispersion velocity $v^* \to 0$ as we approach the DP (blue curve in Fig. 4-10b). This is unphysical for an isolated Dirac cone, and is in marked contrast to the expectation and observation of linear dispersion near the Dirac point in other TMs[14, 56, 110, 123, 137]. We emphasize that higher order corrections to the single Dirac cone dispersion are expected to contribute only for larger momenta, as observed in other TMs[14, 56, 110].

In this range however, we find that the B-linear fit (Fig. 4-10c) gives a constant intercept ($\varepsilon_{\mathrm{int,R}} = -194$ mV), suggesting that the quasiparticles behave like massive fermions in this regime. That the range of energies for $N = 1 - 6$ approximately corresponds to the energy range $\varepsilon_{\mathrm{bot}} < \varepsilon < \varepsilon_{\mathrm{S}}$ suggests that the Rashba picture of SOC-split parabolic bands is more appropriate for analyzing the single particle behavior here. We will return to these low energy states after a quantitative reconciliation of the higher energy LLs with QPI.

4.3 Quasiparticle Interference of Topological Surface States

To examine the quasiparticle interference arising from the scattering of SSs from single-atom impurities, spatial conductance $(dI/dV(\vec{r}))$ maps were recorded on several samples. These $dI/dV(\vec{r}, V)$ maps were acquired over large (80-190 nm) fields of view, affording high q-space resolution ($\sim$ 0.004 Å^{-1}, or 0.3% of the BZ). Drift effects over the long time scale (3-5 days) of data acquisition were minimized by (a) relaxation for $\sim$ 6 − 8 hours over the region of interest before data acquisition to reduce piezoelectric creep, and (b) keeping the temperature constant to within 200 μK to reduce thermal effects.

As exemplified in Fig. 4-11a-d, impurity scattering creates striking interference patterns in spatial conductance on Sb(111). The interference patterns are markedly different around the distinct kinds of impurities noted to exist on the sample surface (Fig. 4-2a), appearing more triangular around one kind of impurities, and more hexagonal around the other. The periodicity of the interference patterns changes monotonically through Fig. 4-11a-d, the wavelength decreasing with increasing energy (sample bias).

For quantitative determination of the dispersing QPI modes, the conductance maps were normalized, Fourier transformed, and six-fold symmetrized to improve the signal-to-noise[23, 68, 70, 122]. In the Fourier space conductance maps shown in Fig. 4-11e-h, we note the presence of peaks along both the $\Gamma - M$ and $\Gamma - K$ reciprocal directions, which disperse towards higher wavevectors with increasing energy.

Conductance linecuts were then extracted along the high-symmetry ($\Gamma - M$ and $\Gamma - K$) reciprocal directions through the Fourier transformed maps (e.g. Fig. 4-11e-h) for all energy layers. These linecut plots (e.g. Fig. 4-12 and Fig. 4-13) clearly show the QPI modes as intensity peaks that disperse approximately linearly with energy (Fig. 4-12a-b) over $\sim$ 300 mV from the DP, the $\Gamma - M$ mode having been reported previously[135, 138]. The prominent modes seen in such data sets are labeled as $q_{\Gamma-M,1}$ and $q_{\Gamma-K}$ respectively. The Fourier positions of the QPI modes were measured by fitting the linecut data to a Lorentzian peak profile for each energy layer.

4.3.1 Scattering in Magnetic Field

The application of an external magnetic field breaks time-reversal symmetry. In principle, this would mean that backscattering is no longer forbidden. We would expect the SS spins to tilt from being perfectly in-plane, with the magnitude of tilt determined by the ratio of the Zeeman energy to the Fermi energy, $\theta_Z = g\mu_B B/\varepsilon_F$. Therefore, the onset of field-induced backscattering can in principle determine the SS g-factor. In addition, the onset of LLs is expect to manifest spatially around impurities in the form of QPI modes corresponding to bound LL states at finite magnetic fields[139].
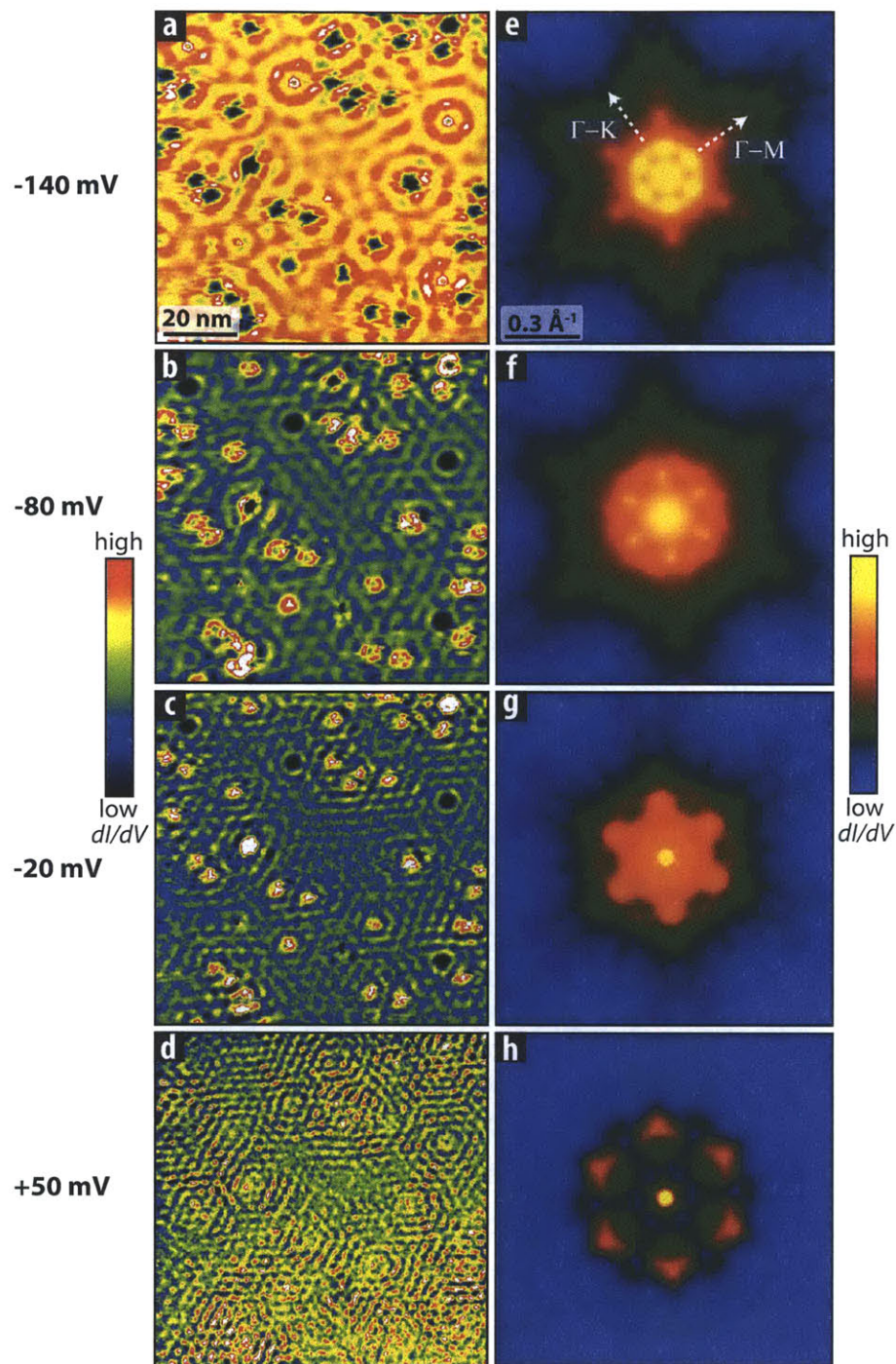
Figure 4-11: Quasiparticle Interference: Conductance Maps in Real and Reciprocal Space. (a–d) $dI/dV(\vec{r}, V)$ maps at sample bias -140 mV (a), -80 mV (b), -20 mV (c), and +50 mV (d), exemplifying standing wave patterns generated by scattering from impurities. **(e–h)** Fourier Transforms (FTs) of (a–d) respectively, showing distinct conductance peaks along the $\Gamma - M$ and $\Gamma - K$ reciprocal directions. FTs have been six-fold symmetrized to improve signal quality.
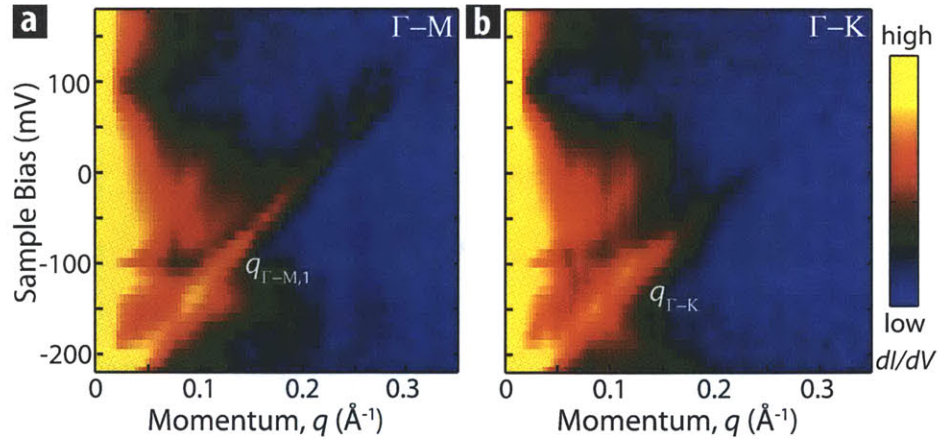
Figure 4-12: Quasiparticle Interference: Conductance Plot of Dispersing Modes. (a, b) Conductance linecuts through the FTs along the $\Gamma - M$ (a) and $\Gamma - K$ (b) directions, generated from 190 nm spatial maps. The prominent dispersing modes along each direction are labeled $q_{\Gamma-M,1}$ and $q_{\Gamma-K}$.
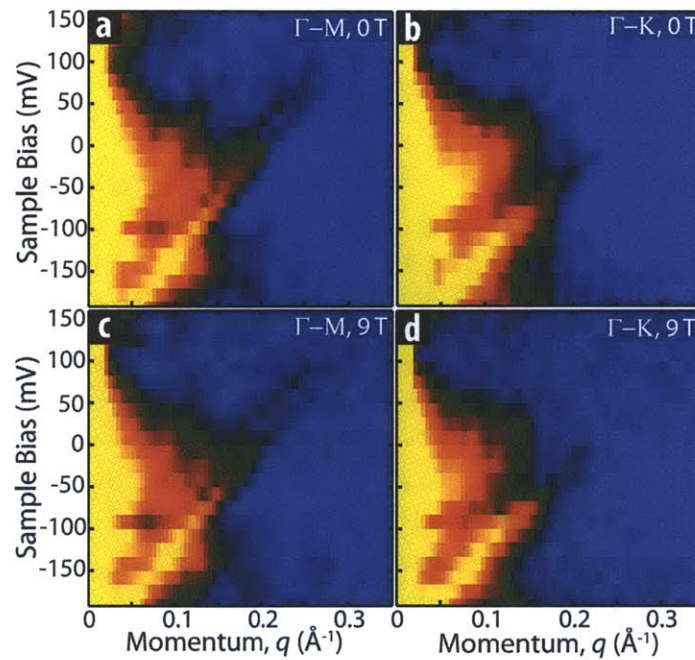
Figure 4-13: Quasiparticle Interference: Dispersing Modes in a Magnetic Field. (a-d) Linecuts through the FTs generated from 140 nm spatial dI/dV maps, along the $\Gamma - M$ (a, c) and $\Gamma - K$ (b, d) reciprocal directions. The maps were acquired at 0 T (a, b) and 9 T (c, d) over the same spatial region. The quasiparticle dispersion is unchanged to within 2% in the presence of a 9 T magnetic field. Setpoint parameters: $V_0 = +200\,\text{mV}$; $R_J = 0.2\,\text{G}\Omega$ (a); $V_{\text{mod}} = 10\,\text{mV}$.

To examine the effects of magnetic field on the scattering modes, conductance maps were recorded over the same ~140 nm spatial region at 0 T and 9 T magnetic fields (Fig. 4-13) with all other experimental parameters held identical. No change is observed in the QPI dispersions in the presence of a magnetic field. Identical QPI modes are seen at 0 T and 9 T with the dispersion

unchanged to within 2% (c.f. [139]). No field-induced backscattering was observed, as detailed further in § 5.2.2.

4.4 Scattering from Step Edges
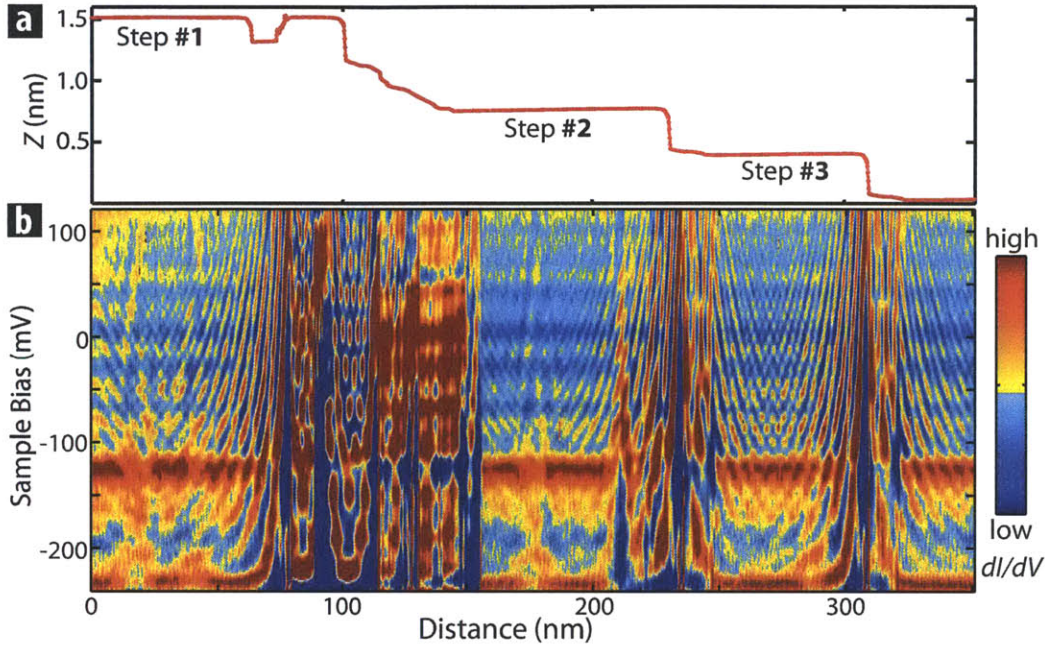
Figure 4-14: Scattering and Interference from Step Edges. (a) A linecut through the topograph in Fig. 4-2b, perpendicular to a series of atomic terraces on the Sb(111) surface (identical to Fig. 4-2c). **(b)** Conductance $(dI/dV(x,V))$ map generated from a linecut perpendicular to the steps, with dispersing oscillations corresponding to scattering from the steps. Oscillations along the vertical direction correspond to states bound between the step edges[135]. Setpoint parameters: $V_0 = +200\,\mathrm{mV}$; $R_J = 10\,\mathrm{G\Omega}$ (a), $0.2\,\mathrm{G\Omega}$ (b); $V_{\mathrm{mod}} = 2\,\mathrm{mV}$.

We had previously noted the observation of several atomic terraces formed perpendicular to the Bragg $(\Gamma - M)$ direction on some regions of the Sb(111) surface (Fig. 4-2b-c). Measurements of spatial conductance $((dI/dV(x,V))$ across a series of terraces, shown in Fig. 4-14b show oscillations emanating from the edges that disperse with energy, as reported previously by Seo *et al.*[135]. These dispersing oscillations should, in principle, be identical to QPI along the $\Gamma - M$ direction. As expected, these oscillations are much stronger in intensity than the impurity scattering detailed previously, due to the larger perturbative effects of atomic steps. We also note the presence of confinement states, more prominent between nearby steps (e.g. the series of resonances between Steps 1-2). These quantized resonances are analogous to the bound states of a quantum well, and have been examined in detail in the previous work by Seo *et al.*[135].

The scattering of SS from atomic step edges can be analyzed similarly to the previous QPI results, by Fourier transforming the conductance data for each atomic terrace. This results in conductance linecuts along the $\Gamma - M$ direction, as shown in Fig. 4-15 for the three terraces indicated
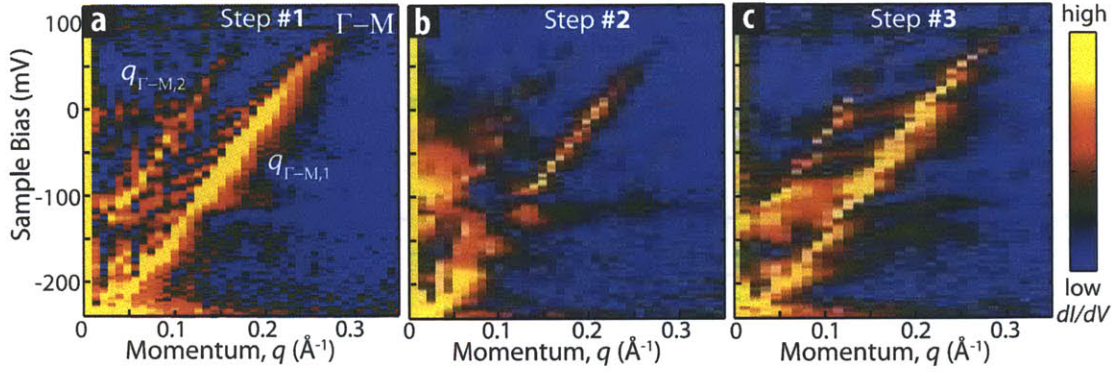
Figure 4-15: Quasiparticle Interference: Dispersing Modes on Atomic Terraces. (a-c) FT of the conductance in Fig. 4-14b from three large terraces indicated in Fig. 4-14a, showing two prominent dispersing modes along the $\Gamma - M$ direction, labeled $q_{\Gamma-M,1}$ and $q_{\Gamma-M,2}$.

in Fig. 4-14a. The most prominent mode observed in these linecuts, $q_{\Gamma-M,1}$ is nominally identical to the analogous mode observed in impurity QPI (Fig. 4-12a). However, step edge scattering allows the extraction of an additional mode along the $\Gamma - M$ direction which onsets at ~ -120 mV, corresponding to the warping energy, ε_w. Both these modes are observed in all three wide terraces imaged in this work.

The application of a magnetic field has no effect on the quasiparticle dispersion, and Landau quantization is found to exist along with the quantization of bound states. The quasiparticle dispersions obtained over terraced regions using Landau quantization and QPI are compared with analogous dispersions over flat regions in § 5.3.

Chapter 5

MR-STM Band Structure and Rashba-Dirac Crossover of Topological Surface States

Having detailed the simultaneous observation of Landau quantization and quasiparticle interference phenomena associated with the surface states of topological Sb in the previous chapter, we now identify their momentum space origin. Subsequently we report, for the first time, their quantitative reconciliation (to 3%), after two decades of their observation in various materials. We therefore establish momentum-resolved scanning tunneling microscopy (MR-STM) as a robust nanoscale band structure probe, and reconstruct the multi-component dispersion of Sb(111) surface states. We quantify surface state parameters relevant to spintronics applications and clarify the relationship between bulk conductivity and surface state robustness. Finally, we understand the anomalous behavior of the low index Landau levels detailed in the previous chapter as arising from a crossover in the single particle behavior from massless Dirac to massive Rashba character – a unique signature of topological surface states.

5.1 Identification of LL and QPI Modes

The $\varepsilon(q)$ dispersions of all quasiparticle modes measured over the same spatial region are shown in Fig. 5-1, with the addition of $q_{\Gamma-M,2}$, which is acquired from a nearby step edge. The marked variation in the dispersion of the various modes is reflective of the multi-component SS band structure of Sb(111). The notable features in Fig. 5-1 include (a) the onset of $q_{\Gamma-M,2}$ at a slightly higher energy, corresponding to ε_w, compared to the other QPI modes; (b) the identical dispersion of $q_{\Gamma-M,1}(\varepsilon)$ and $q_{\Gamma-K}(\varepsilon)$ for $\varepsilon < \varepsilon_S$, and their deviation above ε_S; and (c) the overlap of LL and QPI dispersions over ~ 300 mV.
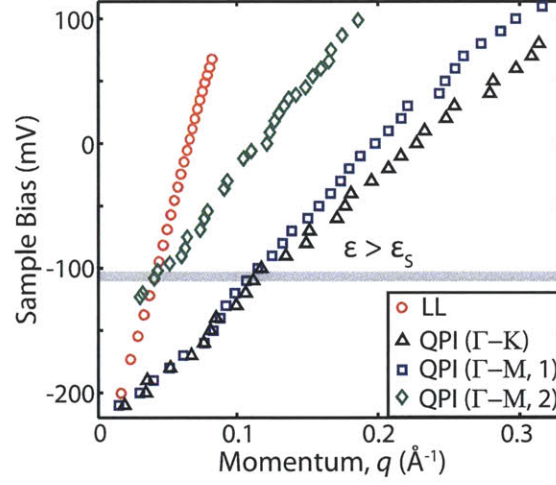
Figure 5-1: MR-STM: Compilation of Dispersing Modes. A compilation of the $\varepsilon(q)$ dispersions recorded over the same atomically flat spatial region (note – $q_{\Gamma-M,2}$ is acquired from a nearby step edge, Fig. 4-15a) using Landau quantization (Fig. 4-9a, red) and QPI (black and blue, from Fig. 4-12a-b).

To identify the momentum space origin of these dispersing modes, we examine schematics of the CECs in Fig. 5-2, which display three qualitatively different shapes over the energy range of interest. For $\varepsilon_D < \varepsilon < \varepsilon_w$, the CECs are concentric spin-polarized circles (Fig. 5-2b), corresponding to the spin-split Rashba parabolas. Here, the only allowed scattering mode is inter-band scattering between parallel spins, and therefore $q_{\Gamma-M,1}(\varepsilon)$ and $q_{\Gamma-K}(\varepsilon)$ both correspond to this mode, and are identical. For $\varepsilon_w < \varepsilon < \varepsilon_S$, the outer Rashba cone acquires a warped snowflake shape (Fig. 5-2c), which corresponds to the onset of intraband scattering on the outer cone, observed as the $q_{\Gamma-M,2}(\varepsilon)$ mode[135]. Meanwhile, the k-space origin of $q_{\Gamma-M,1}(\varepsilon)$ and $q_{\Gamma-K}(\varepsilon)$ is the same as before.

Finally, for $\varepsilon > \varepsilon_S$, the outer cone is no longer closed (Fig. 5-2d). While the $q_{\Gamma-M,1}(\varepsilon)$ mode remains the same as before, $q_{\Gamma-K}(\varepsilon)$ now corresponds to intra-band scattering across the outer 'pocket', analogous to $q_{\Gamma-M,2}(\varepsilon)$. Above ε_S, the LL wavevector, $q_{LL}(\varepsilon)$, is well defined, and corresponds to the area of the inner pocket – the only closed CEC over the energy range of interest.

Therefore, the dominant $\Gamma - M$ QPI mode, $q_{\Gamma-M,1}(\varepsilon)$, corresponds to inter-band scattering between parallel spins the the entire observed energy range. In contrast, the $\Gamma - K$ QPI mode $q_{\Gamma-K}(\varepsilon)$ corresponds initially to inter-band scattering below ε_S, and transitions to scattering between sections of the outer pocket for $\varepsilon > \varepsilon_S$. We note the kink and slight change in magnitude of $q_{\Gamma-K}(\varepsilon)$ around ε_S (Fig. 5-1), corresponding to this crossover from inter-pocket scattering to intra-pocket scattering. This crossover signifies the turnover of the outer cone and confirms the topological nature of the surface states, in contrast to conventional Rashba SOC split states known to exist on TM surfaces[127–129].
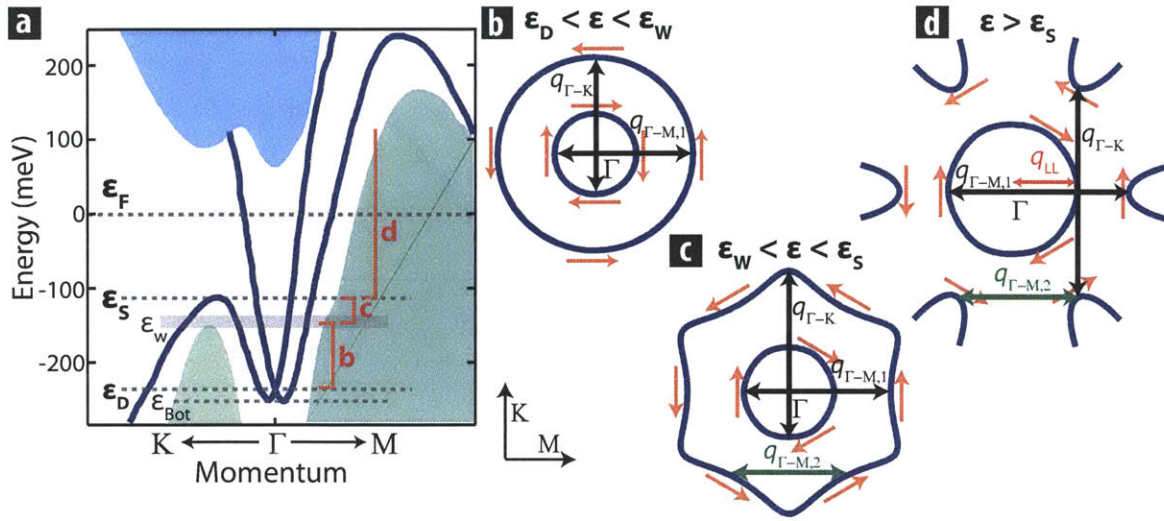
Figure 5-2: Sb(111) Band Structure and Identification of Dispersing Modes. (a) A zoom-in of the SS band structure shown in Fig. 4-4b over the energy range of interest (c.f. Fig. 5-1). **(b–d)** Schematic evolution of the SS constant energy contours (CECs), with the in-plane spin polarization (red arrows) and q-space location of the dispersing modes from Fig. 5-1 overlaid. The characteristic energy ranges of the CECs are shown in (a) (red braces) . From the Dirac point (ε_D) up to energy ε_S, the CECs correspond to a Rashba-split double cone structure (b-c). The outer cone acquires a warped snowflake shape above an intermediate energy ε_w (c). Above ε_S, the CEC topology changes, and the outer SS band no longer corresponds to a closed contour (d).

5.2 Measuring the SS Band Structure

Having determined the momentum space origin of all observed dispersing modes, we note that several of these modes overlap over a ~ 300 meV energy range. Therefore, these modes can be used to extract the multi-component SS band structure in the following manner.

For $\varepsilon > \varepsilon_S$, we note the presence of three modes: $q_{\Gamma-M,1}(\varepsilon)$, $q_{\Gamma-K}(\varepsilon)$, and $q_{LL}(\varepsilon)$; and need to determine three band features in this energy range. First, we use $q_{\Gamma-K}(\varepsilon)$, arising from scattering between the outer pockets for $\varepsilon > \varepsilon_S$, and its direct correspondence to the $\Gamma - M$ dispersion of the outer pocket to find $\varepsilon_{out}(k_{\Gamma-M}) \equiv \varepsilon(q_{\Gamma-K}/\sqrt{3})$. Second, this information, in conjunction with the scattering vector $q_{\Gamma-M,1}$ between the inner and outer pockets, can be used to determine the $\Gamma - M$ dispersion of the inner pocket as $\varepsilon_{in}(k_{\Gamma-M}) \equiv \varepsilon(q_{\Gamma-M,1}) - \varepsilon_{out}(k_{\Gamma-M})$. Finally, the Landau quantization wavevector q_{LL}, which corresponds to the area of the inner pocket, can be used to deduce its $\Gamma - K$ dispersion.

Furthermore, we can deduce the band structure for $\varepsilon < \varepsilon_S$ – for the inner pocket by employing a $k \cdot p$ fit to the $\varepsilon > \varepsilon_S$ data (detailed in § 5.2.1); and for the outer pocket by using the inter-band QPI in this energy range ($q_{\Gamma-K}(\varepsilon)$ and $q_{\Gamma-M,1}(\varepsilon)$), and the $k \cdot p$ fit to the inner pocket. We thus use $q_{LL}(\varepsilon)$, $q_{\Gamma-K}(\varepsilon)$, and $q_{\Gamma-M,1}(\varepsilon)$, in conjunction with the $k \cdot p$ fit to our data, to measure the SS band structure, shown in Fig. 5-3.
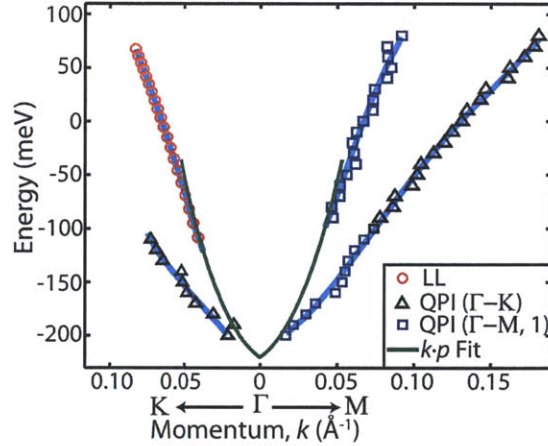
Figure 5-3: MR-STM: Surface State Band Structure. The MR-STM dispersion $\varepsilon(k)$ of the SS band structure, deduced as detailed in the text. Solid cyan lines correspond to a polynomial fit to the data points. Solid green lines correspond to an extrapolation using the Fu $k \cdot p$ model[110].

We therefore introduce MR-STM – a combination of LL and QPI spectroscopy – which is necessary to reconstruct such a multi-component band structure. The MR-STM band structure agrees with ARPES measurements of filled states to within 10%, comparable to the variation between ARPES measurements[136, 138]. Furthermore, the dispersion of the inner pocket, measured independently by Landau quantization and QPI above ε_S, is consistent to 3%, as detailed below.
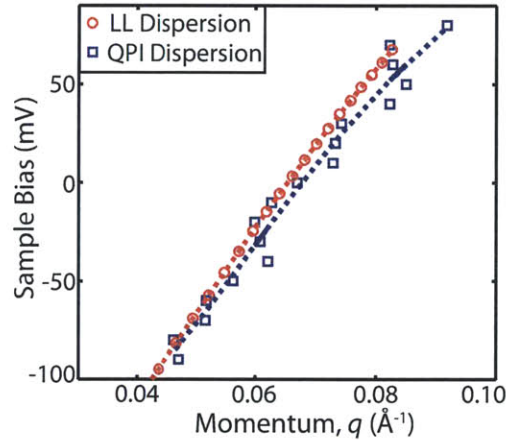
Figure 5-4: MR-STM: Inner Pocket Dispersion from Landau Quantization and QPI. The dispersion of the inner SS pocket measured using LL and QPI techniques over the same spatial region. The observed $\sim 3\%$ difference between the techniques is consistent with hexagonal warping, which results in a difference in dispersion along the $\Gamma - M$ and $\Gamma - K$ directions.

The lack of spatially and spectrally coexisting LL and QPI measurements, in conjunction with up to 40% discrepancies in independently reported LL & QPI dispersions on the same material (graphene)[21, 78] has hindered their use as complementary band structure probes. Our simultaneous observations of LL & QPI in Sb(111) allow us to directly compare the dispersions obtained

using these techniques. In Fig. 5-4, we compare the measured dispersion of the inner pocket in the Dirac regime ($\varepsilon > \varepsilon_S$) from LLs ($\varepsilon_N(q_N)$), and QPI ($\varepsilon(q_{\Gamma-M,1} - q_{\Gamma-K}/\sqrt{3})$). The measured dispersions, $v_{in,LL}$ =4.20 eV·Å and $v_{in,QPI}$ =4.07 eV·Å, are consistent to $\sim$ 3%. The slightly higher dispersion for $v_{in,LL}$ is consistent with the expected contribution of hexagonal warping[110].

5.2.1 $k \cdot p$ Fit and Spintronics Parameters

The MR-STM band structure in the Dirac regime ($\varepsilon > \varepsilon_S$) can be fit to the five-parameter $k \cdot p$ band structure for topological surface states proposed by Fu[110], the details of which are described in § 3.4:

$$E_{\pm}(k) = \varepsilon_{0,D} + k^2/2m \pm \sqrt{v_0^2(1 + \alpha k^2)^2 \cdot k^2 + \lambda_w^2 \cdot (16k_y^6 - 24k_y^2 k^2 + 9k_y^2 k^4)} \qquad (5.1)$$

The fit is performed using the MR-STM data acquired in Dirac regime, with the additional use of the energy scales ε_S, ε_{Bot}, and ε_{Top}. The best fit to our measurements on Sample 1 corresponds to the following parameters values: offset, $\varepsilon_D = -220$ mV; mass, $m = 0.094\,m_e$; Rashba parameter $v_0 = 0.94$ eV·Å; velocity correction, $\alpha = 130$ Å^{-2}; and warping parameter, $\lambda_w = 200$ Å^{-3}. We note that the $k \cdot p$ model is a small-k approximation, and we therefore use it to estimate the SS band structure near the Γ-point, in order to determine the MR-STM band structure for $\varepsilon < \varepsilon_S$. We note the utility of several of these parameters, notably v_0 and l_F (the latter was determined in § 4.2.3), towards spintronics applications. This is discussed further in § 5.5.

Because the $k \cdot p$ fit is valid for small momenta ($k \to 0$), it can also be utilized to understand the aforementioned deviant behavior of the low energy quasiparticles participating in LLs for $N \leq 6$ (§ 5.4).

5.2.2 Absence of Field-Induced Backscattering

As detailed in § 4.3.1, no change is observed in the QPI dispersions in the presence of a magnetic field. This is further shown by a representative linecut at a single bias layer in Fig. 5-5b. First, identical QPI modes are seen at 0 T and 9 T with no measurable difference in dispersion (dashed green line in Fig. 5-5b. Second, no field-induced backscattering modes are observed, as shown by the absence of peaks at the expected positions indicated by dashed blue lines in Fig. 5-5b. The robust protection of SSs from backscattering, even at magnetic fields up to 9 T, is indicative of a low SS g-factor in Sb(111).

5.3 Spatial Sensitivity of MR-STM

So far we have detailed the ability of MR-STM, the complementary use of LLs and QPI, in measuring the SS band structure of Sb(111) up to 100 mV above ε_F – a regime inaccessible to ARPES,
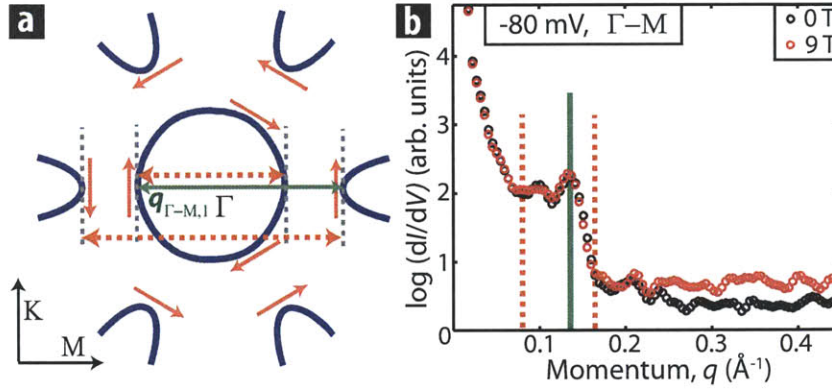
Figure 5-5: Quasiparticle Interference: Absence of *Field-Induced* Backscattering. (a) Schematic k-space CECs of Sb(111) for $\varepsilon > \varepsilon_S$, indicating the location of the observed QPI mode along the $\Gamma - M$ direction, $\vec{q}_{\Gamma-M,1}$ (green) and the expected location of spin-flip backscattering modes (dashed orange) which could be induced by a magnetic field. (b) Comparison of the conductance linecuts at 0 T (black) and 9 T (red), acquired along the $\Gamma - M$ direction at -80 mV (a representative energy layer), extracted from Fig. 4-13a,c respectively. The solid green line indicates the prominent QPI mode $q_{\Gamma-M,1}$, while the dashed orange lines indicate the expected positions of spin-flip backscattering modes, which we do not observe even at 9 T.

a filled states only probe. Now we demonstrate the nanoscale spatial resolution of MR-STM.

5.3.1 Variation Between Flat and Terraced Regions
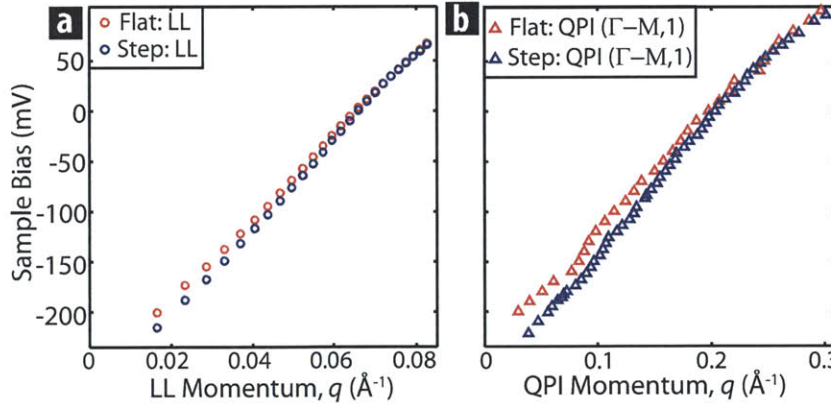
Figure 5-6: MR-STM Measurements: Variations Between Flat and Terraced Regions. Comparison of the (a) LL and (b) QPI $(\Gamma - M, 1)$ dispersion obtained over atomically flat regions (red) and terraced regions (blue), ~ 200 nm away from each other. Both the LL and QPI dispersions indicate a consistent, non-rigid difference in the band structure between the two regions, demonstrating the nanoscale spatial sensitivity of MR-STM.

Having established MR-STM as a self-consistent band structure probe, we explicitly demonstrate its nanoscale spatial sensitivity by comparing the MR-STM measurements recorded on atomically flat regions (Fig. 5-1) with those on terraced regions (Fig. 4-14), separated by ~ 200 nm, in Fig. 5-6. Both the LL & QPI $(\Gamma - M,1)$ measurements indicate a non-rigid band structure change between the regions, corresponding to a chemical potential offset of ~ -15 mV, and an increase in

dispersion of $\sim 5\%$ in the terraced regions.

The step edges must have broken bonds, which may cause charge redistribution as well as structural distortion, either of which may bear responsibility for the non-rigid changes in band structure. Previous STM measurements on various electronic materials have reported nanoscale fluctuations in chemical potential[21, 23, 61], and our observations of nanoscale non-rigid band structure variation underscore the importance of using STM as a local band structure probe.

5.3.2 Variation Across Terraces
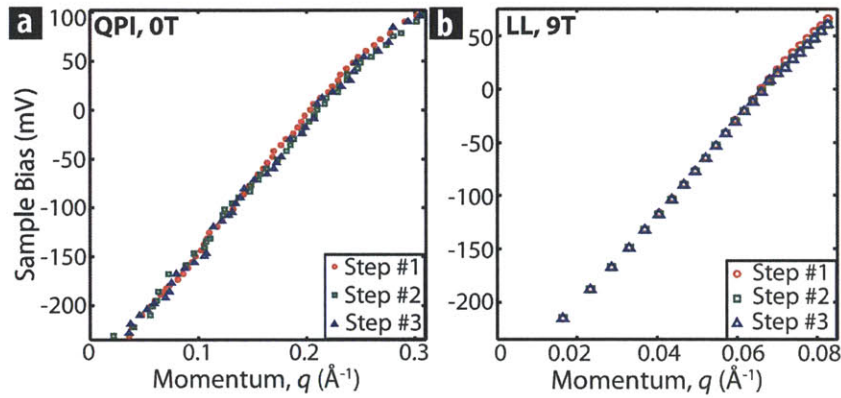
Figure 5-7: MR-STM Measurements: Variations Across Atomic Terraces. A comparison of the QPI ($\Gamma - M, 1$) and LL dispersions recorded at the three terraces indicated in (Fig. 4-14a). Small ($< 2\%$) deviations in the dispersion across the terraces are observed. Note that these deviations are consistent for both the MR-STM techniques: red points are above the others at high energies for both (a) and (b).

The measured dispersion of the $\Gamma - M, 1$ QPI mode is consistent to within 2% across the terraces (Fig. 5-7a), and also agrees with the results reported by Seo *et al*[135]. Additionally, our LL spectroscopy measurements (Fig. 5-7b) show a similarly consistent dispersion across the terraces. Finally, the small deviations between the dispersions of the terraces are consistent for both the MR-STM techniques.

5.3.3 Chemical Potential Homogeneity

Unlike other Dirac materials[14, 21, 23, 68], Sb(111) does not display marked nanoscale inhomogeneity. While the quasiparticle interference around single-atom impurities do result in standing wave patterns in spatial conductance maps (Fig. 5-8a), the LL peak energies are spatially consistent to within 2 mV (Fig. 5-8b-c), and the chemical potential is therefore an order of magnitude more homogeneous than in Bi_2Se_3[23]. We suggest that the presence of a parallel bulk conduction channel could play a role in the electronic homogeneity observed in Sb(111).

Finally, the observed chemical potential offset (~ 14 mV) and up to 2% variations in the surface state dispersion (Fig. 4-9a) could be attributed to the variation in impurity concentrations between
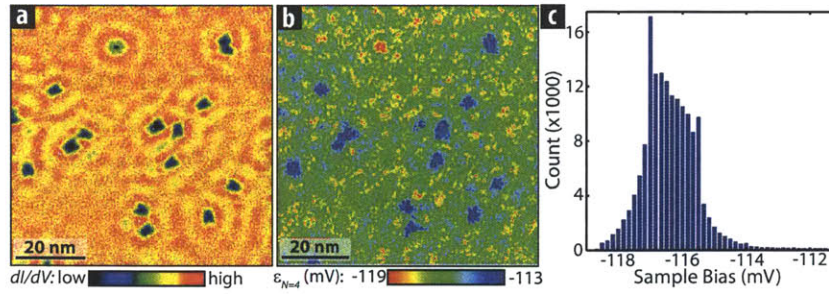
Figure 5-8: Spatial Homogeneity of Landau Quantization. **(a)** A $dI/dV(\vec{r}, V)$ map acquired at 9 T, +117 mV, corresponding to the average bias value for the $N = 4$ LL peak. **(b)** Spatial variation in the $N = 4$ LL energy. Observable variations are associated with QPI or impurities. $V_0 = +100\,\text{mV}$; $R_J = 0.1\,\text{G}\Omega$ (a); $V_{\text{mod}} = 1.2\,\text{mV}$. **(c)** A histogram of the variation in the $N = 4$ LL energy shown in (b), corresponding to a mean value of (117 ± 1) mV.

samples. We note that ARPES measurements of the surface state dispersion of Sb(111) report discrepancies of a similar magnitude[136, 138].

5.4 Landau Quantization Anomaly and Rashba-Dirac Crossover

In the Rashba picture of an SOC-split parabolic band, shown in Fig. 5-9a, LLs are separated by the cyclotron energy, $\hbar\omega_{\text{c}}$. An additional term dependent on the Rashba parameter and g-factor, further splits each LL, indexed by n, for $n > 0$, according to[140, 141]:

$$\varepsilon_{\text{R}}(n = 0) = \varepsilon_{0,\text{R}} + (1/2) \cdot (\hbar\omega_{\text{c}} + g\mu_{\text{B}}B)$$

$$\varepsilon_{\text{R}}(n > 0) = \varepsilon_{0,\text{R}} + \hbar\omega_{\text{c}}n \pm \sqrt{\delta^2/4 + (2mv_0^2) \cdot n\hbar\omega_{\text{c}}} \tag{5.2}$$

Here, $\omega_{\text{c}} = eB/m$ is the cyclotron energy, $\delta = (1 - 1/2\,gm^*)\hbar\omega_{\text{c}}$, $m^* = m/m_e$ is the effective mass, and g is the electron g-factor. The upper and lower Rashba-split branches qualitatively correspond to the inner and outer Rashba 'cones', respectively. Fig. 5-9b shows a comparison of the Rashba formula fit to the LL dispersion measured on Sample 2, using the parameters $\varepsilon_{\text{int,R}} = -194$ mV (from Fig. 4-10b); $m^* = 0.094\,m_e$, $v_0 = 0.94$ eV·Å (from $k \cdot p$ fit to Sample 1); and $g = 2$ - to the lower LLs; along with a comparison of the Dirac fit to the higher LLs with $\varepsilon_{\text{int,D}} = -278$ mV and $v^* = 4.42$ eV·Å. The Rashba fit shown, deriving from the upper Rashba branch (Fig. 5-9a), qualitatively reproduces the measured dispersion. The underestimation of the dispersion for $N > 1$ can be understood to arise from cubic corrections to the dispersion of the outer cone, which is not accounted for in the parabolic approximation above. We further suggest that this crossover might explain the anomalous LLs reported near the Dirac point in Bi_2Te_3[61].
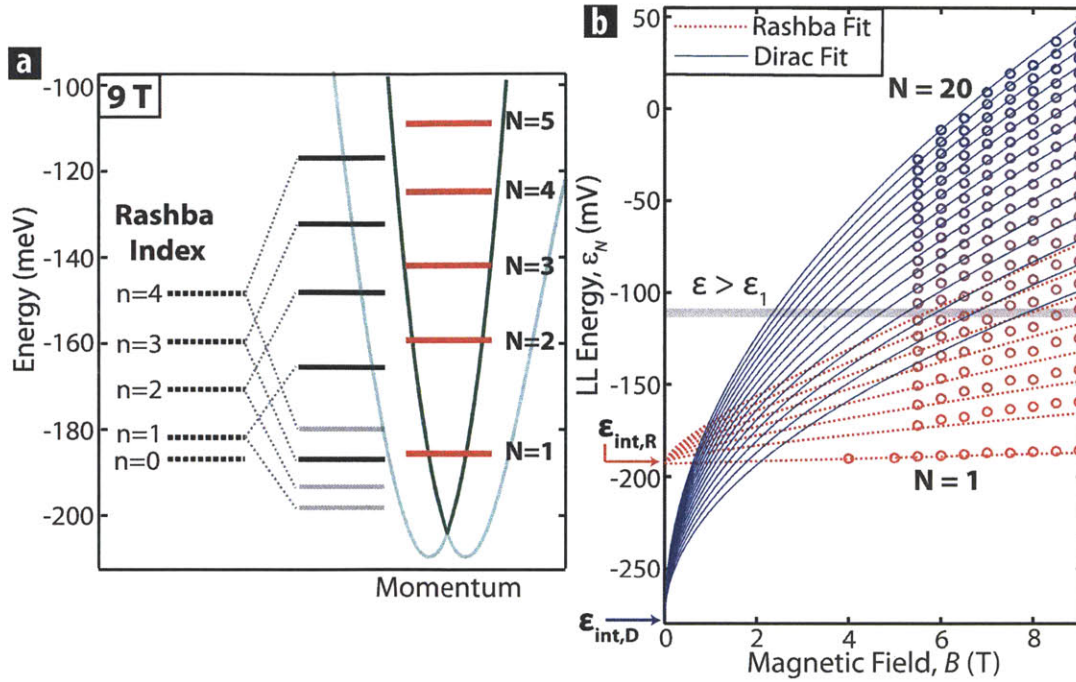
Figure 5-9: Landau Quantization: Quantifying the LL Crossover Behavior. (a) Schematic illustration of Rashba-split LLs for $\varepsilon < \varepsilon_S$, calculated using the MR-STM-determined $k \cdot p$ fit parameters (green bands). The Rashba SOC splits conventional LLs (dashed black) into upper (solid black) and lower (solid grey) branches. The experimentally observed LLs at 9 T (solid red lines) correspond qualitatively to the upper Rashba branch. (b) Fits to the magnetic field dispersion of the first 20 LL indices based on the Rashba (red) and Dirac (blue) formulations. The Landau quantized quasiparticles evolve from massive Rashba character with $\varepsilon_{int,R} = -194$ mV below ε_1 to massless Dirac-like above ε_1 with $\varepsilon_{int,D} = -278$ mV.

5.5 Towards Better Topological Materials

Our studies of SSs on Sb(111) shed light on several fundamental issues pertaining to TMs. First, the existence of up to 27 LLs arising from a single, robust cone – despite the presence of proximate surface and bulk bands throughout the energy range – is surprising. It had been speculated that in the Bi_2X_3 class of TMs, the onset of bulk bands induces surface-bulk scattering, limiting the observed range of LLs[56]. In contrast, our demonstration of robust Landau quantization in a semimetal suggests that even in the presence of proximate bulk bands, closed surface state contours strongly maintain their topological character. Second, the emergence of the Dirac character of Landau quantized quasiparticles from the Rashba dispersion reveals the signature of topological SSs, and draws a marked contrast with Dirac fermions in graphene, which arise from a spinless tight-binding model[57].

Our results have practical implications for the development and growth of TMs. The use of TMs for spintronics devices will require strong spin-momentum locking, long mean free path, and small g-factor. We note the quantitative distinction between the Rashba parameter $v_0 = 0.94$ eV·Å (extracted from the $k \cdot p$ fit) and the Dirac velocity $v_D = 4.2$ eV·Å, and clarify that the former is

the spin-momentum locking parameter relevant towards spintronics applications. We quantify the mean free path, $l_F = 65$ nm (Fig. 4-9b), apparently limited only by visible surface defects in Sb (Fig. 4-2a). Further theoretical work to quantitatively reconcile the measured $N < 6$ LLs with Eqn. 5.2 may enable the determination of the g-factor in Sb as well.

The search for better TMs has gravitated towards insulating ternary and quaternary materials, tuned off-stoichiometry to enhance the SS contribution in transport measurements[100, 131, 132]. However, our observations suggest that the presence of a bulk continuum in a semimetal suppresses chemical potential fluctuations[23], actually enhancing the mean free path rather than diminishing the lifetime of SS quasiparticles as had previously been speculated[56, 133]. We therefore suggest that epitaxial heterostructures, with the appropriate use of semimetals, is an alternate avenue towards better TMs. Finally, our observation of a crossover of quasiparticle character from massive Rashba-like to massless Dirac-like on a robust single SS cone, suggests alternative band structure engineering routes to tuning the properties of SSs[142, 143].

Part II

Spectroscopic Studies of Density Wave Order

In this part of the thesis, we describe our spectroscopic studies of the charge density waves (CDWs) in the transition metal dichalcogenide $2H$-NbSe$_2$.

We begin by motivating the origin of CDW order as a Fermi surface instability driven by a divergence in electronic reponse in one-dimensional (1D) systems, and show its extension to two dimensional (2D) systems. We outline the possible role of the Fermi surface and that of coupling to collective modes in driving the CDW transition. Following this, we examine the current understanding of the CDW transition in NbSe$_2$, discussing the debated issues of the CDW driving mechanism and the magnitude of the spectral gap, directly motivating our experiments.

We then discuss our STM studies of NbSe$_2$ - specifically the discovery of a quantum (zero temperature) interface between a triangular ($3Q$) and a stripe ($1Q$) CDW with different wavelengths. We first examine the origin of the quantum phase transition from the commonly observed $3Q$ phase to the hitherto unobserved $1Q$ phase, and show it to be driven by local strain. Following a phenomenological description of this phase transition, we discuss the relevance of our observations to strongly correlated systems evincing analogous charge order.

Following this, we use the the $1Q - 3Q$ CDW interface, in conjunction with band structure calculations, to address the two major debates in NbSe$_2$. First, the distinct wavelengths of the CDWs demonstrate that FS nesting plays a negligible role in setting their magnitude. Second, the distinct tunneling spectra of the $1Q$ CDW region help us disentangle the $3Q$ CDW spectra to expose a particle-hole asymmetric gap riding on top of a strong inelastic background. We then discuss the relevance of these observations to other CDW systems.

The STM experiments reported in this work were done in collaboration with Michael M. Yee, Yang He, Eric W. Hudson, and Jennifer E. Hoffman at Harvard University. The samples used in the work - single crystals of $2H$-NbSe$_2$ - were prepared by Wilfried Krüger at the University of Kiel. The supporting ARPES measurements reported here, used to generate the tight-binding band structure, were performed by Dirk J. Rahn and Kai Rossnagel at the University of Kiel. Band structure calculations and fits to the STM spectra were peformed by Jasper van Wezel and Michael R. Norman at Argonne National Laboratory.

The results detailed in this part of the thesis have been been published in [18].

Chapter 6

Charge Density Waves in Two Dimensions

While a classical phase transition separates two states of matter at different temperatures, two ordered ground states of a material at zero temperature are separated by a quantum critical point (QCP). The competition between proximate ordered phases near the QCP can dramatically influence a large region of the phase diagram[144]. While the fluctuations from competing quantum states lead to exotic physics even at higher temperatures, low temperature studies of these states can lead to a better understanding of the root of the competition.

Density waves - charge or spin ordered states of collective origin driven by instabilities of the Fermi surface - exist in close proximity to superconductivity in several classes of correlated materials[145–147], and various proposals have recently emerged to study their interplay in the presence of strong inhomogeneity in these systems[148]. However, density waves have been difficult to isolate in the presence of chemical disorder, and the suspected causal link between competing density wave orders and high temperature superconductivity is a subject of much debate.

In this light, it is surprising that charge density waves (CDWs) are not fully understood even in the weakly correlated and stoichiometric transition metal dichalcogenides (TMDCs). While a classic CDW arises from strong Fermi surface nesting, resulting in a sharply peaked susceptibility and a Kohn anomaly at the CDW wavevector, the quasi-2D transition metal dichalcogenides (TMDCs) are known to deviate from this picture[149].

6.1 Fermi Surface Instability and Density Waves

The conventional picture of a density wave is that it arises from the instability of the Fermi surface (FS) to a charge modulation with a periodicity related to the Fermi wavevector, k_F. The origin

87
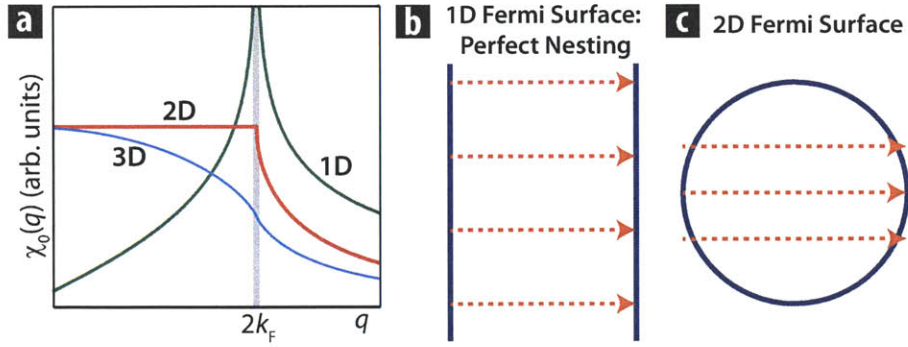
Figure 6-1: Susceptibility, Fermi Surface Nesting and Density Wave Formation. (a) The non-interacting susceptibility, $\chi_0(q, \omega = 0)$ of a free electron gas in one, two and three dimensions. While $\chi_0(q)$ diverges in one dimension at $q = 2k_F$, it does not display such singular behavior in two and three dimensions **(b-c)** Pictorial Fermi surface (FS) 'nesting' representation of the susceptibility for (b) one and (c) two dimensions, with the FS shown in blue, and the nesting vector $2k_F$ in dashed orange. A 1D FS nests perfectly, while an isotropic 2D FS does not nest well.

of such an instability can be understood by examining the response of the electron system to charge perturbations in momentum space. When an electrostatic potential, $\phi(\vec{q})$ is applied to a d-dimensional electron system, it leads to a rearrangement of the electron density, and the resultant distribution can be expressed in terms of an induced charge $\rho_{\mathrm{ind}}(\vec{q})$, as [150]

$$\rho_{\mathrm{ind}}(\vec{q}) = \chi(\vec{q})\,\phi(\vec{q}) \tag{6.1}$$

In other words, the response is quantified by the Lindhard function, also known as the static susceptibility, $\chi(\vec{q}, \omega = 0)$, defined as

$$\boxed{\chi(\vec{q}) = \int d\vec{k}\,\frac{f_{\vec{k}} - f_{\vec{k}+\vec{q}}}{\varepsilon_{\vec{k}} - \varepsilon_{\vec{k}+\vec{q}}}} \tag{6.2}$$

Here $f_{\vec{k}}$ is the Fermi function, and $\varepsilon_{\vec{k}}$ describes the band structure of the electron system.

6.1.1 Fermi Surface Instability and Density Waves in One Dimension

For a 1D electron system with parabolic dispersion, this expression is straightforward to evaluate[151], and is found to be

$$\chi_{1D}(q) = -e^2 D(\varepsilon_F)\,\log\left|\frac{q + 2k_F}{q - 2k_F}\right| \tag{6.3}$$

Thus, the response of a 1D electron system to charge perturbations diverges to infinity at $q =$

$2k_F$, as shown in Fig. 6-1a (green curve). This divergence can be well understood within a FS nesting picture. The FS of a 1D electron system consists of two points at $\pm k_F$. The wavevector connecting these two points represents the entire joint density of states at ε_F, and the electron system is therefore unstable to external perturbations at this wavevector (Fig. 6-1a). The system thus spontaneously breaks translational symmetry at zero temperature, resulting in a uniform charge modulation with periodicity $\lambda_{CDW} = 2\pi/(2k_F)$ - known as a charge density wave.

A consequence of the divergent response at $2k_F$ is that the screening response of the electron gas is enhanced at this wavevector, reducing the repulsive forces between the ions forming the underlying lattice. This leads to softening of the energy required to induce crystalline vibrations, or phonons, at $2k_F$, and is known as a Kohn anomaly[1]. Furthermore, below the transition temperature T_{CDW}, it produces static distortion in the atomic lattice (typically $1 - 2\%$) with λ_{CDW} periodicity, known as a Peierls distortion[152].

The formation of such a density wave phase in the presence of weak coupling between the electron gas and phonons can be understood with an analogy to the BCS picture of superconductivity, also a FS instability. The density wave phase is equivalent to the condensation of electron-hole pairs that form spin singlets with finite momentum ($2k_F$), and can therefore be described by an order parameter of the BCS form,

$$\Delta_{CDW} \equiv |\Delta| \exp{(i\varphi)} \tag{6.4}$$

where $|\Delta|$ and φ represent the magnitude and phase of the order parameter respectively. Therefore, in direct analogy to a superconducting transition, the phase transition to a CDW ground state results in the opening of a spectral gap in the single particle density of states around ε_F, the magnitude of which directly corresponds to Δ_{CDW}[151]. For a 1D system, the spectral gap is required to be centered at ε_F.

6.1.2 Density Waves in Higher Dimensions

The concept of a FS nesting driven instability leading to a CDW can be generalized in a straightforward manner to electron systems with highly aniostropic band structure that are approximately one-dimensional, i.e. quasi-1D systems. Several experimentally realized material systems have such strongly anisotropic band structures that can be approximated to be quasi-1D, such as transition metal chalcogenides of the MX_3 form (e.g. $NbSe_3$), transition metal bronzes of the $A_{0.3}MoO_3$ form (e.g. $K_{0.3}MoO_3$), and several classes of inorganic and organic linear chain compounds[151, 153].

In the case of electron systems with dimensionality $d > 1$, i.e. band structures with higher

dimensional character, nesting cannot connect the entire FS. In the extreme case of isotropic band structures, FS nesting connects only small portions of the FS (e.g. Fig. 6-1c), and the divergence of the response $\chi(q)$ progressively weakens in 2D and 3D, as shown in Fig. 6-1a (red and cyan curves)[151]. The existence of CDW order in higher dimensional electron systems, e.g. transition metal dichalcogenides[154], rare earth tritellurides[155], and (potentially) cuprate superconductors[156], is reconciled with the conventional nesting picture by examining smaller portions of the FS. If sufficiently large portions of the FS are nested as to lead to a lower energy ground state, then a CDW is understood to reside over these FS regions. This allows for the momentum space coexistence of CDW with other ordered states, and motivates us to examine the energetics of density wave formation.

6.1.3 Energetics of Density Wave Formation

In the conventional picture of density waves, the dominance of FS nesting at a certain wavevector, ($\vec{q}_{CDW}$) leads to a peak in the bare susceptibility, $\chi_0(\vec{q}, \omega = 0)$ at $\vec{q}_{CDW}$. In the presence of electron-phonon coupling, this results in the softening of the corresponding phonon mode at $\vec{q}_{CDW}$, known as a Kohn anomaly, and this results in a transition to a CDW phase[157]. More generally, Chan and Heine[158] have derived the condition for the formation of a stable density wave phase (further discussed in[157]) to be:

$$\frac{4\eta(q)^2}{\hbar\omega_0} \geq \frac{1}{\chi_0(q)} + \left(2\tilde{U}(q) - \tilde{V}(q)\right) \tag{6.5}$$

Here, $\eta(q)$ is the electron-phonon coupling parameter, ω_0 is the unrenormalized phonon energy, and $\tilde{U}(q)$ and $\tilde{V}(q)$ are the Coulomb and exchange interactions respectively. In the conventional FS nesting driven scenario, q_{CDW} is determined by the peak in $\chi_0(q)$, i.e. the right hand side of Eqn. 6.5[157, 158].

However, for materials with two- or three-dimensional band structures without notable anisotropy (e.g. dichalcogenides), the divergence of $\chi_0(q)$ is logarithmic or less. Therefore, the susceptibility $\chi_0(q)$ may have a broad peak over a range of wavevectors, corresponding to a broad Kohn anomaly. In such a weak-nesting scenario, the q-dependence of the left hand side of Eqn. 6.5 assumes importance, and the electron-phonon coupling term $\eta(q)$ can in principle determine q_{CDW}.

6.2 Density Wave Physics and Superconductivity in NbSe$_2$

$2H$-NbSe$_2$ (henceforth refererred to as NbSe$_2$) is a layered TMDC which has emerged as a model system for understanding the interplay of coexisting CDW and SC phases[154]. NbSe$_2$ undergoes a transition to an incommensurate CDW phase at $T_{CDW} \sim 33\,\mathrm{K}$[154, 159]. The CDW wavelength ($\sim 3a_0$, a_0 being the lattice constant) is known to vary with temperature (below T_{CDW}) in this material[159]. However unlike other TMDCs[154], the phase transition to a incommensu-

rate CDW phase is not followed by a transition to a commensurate phase. On the other hand, it does undergo a transition to a superconducting phase below $T_{SC} \simeq 7.2\,\mathrm{K}$[154, 159]. The spatial coexistence of CDW and superconducting phases in this material has generated much recent interest from the perspective of understanding coexisting and competing orders in more strongly correlated materials[160–162].

Extensive studies using ARPES and STM measurements, in conjunction with transport measurements, have shown that the superconducting order parameter in NbSe$_2$ has s-wave symmetry, and is anisotropic in momentum space[163–165]. Leading-edge shift measurements of ARPES spectral weight find large portions of the multi-band FS to be gapped below T_{SC} upon the onset of superconducting order, with an average gap size, $\Delta_{SC} \sim 1$ meV. The physics of the superconducting phase can therefore be well described within the intermediate coupling BCS picture with an anisotropic order parameter[163].

The onset of the CDW phase, found to be very prominent in X-ray and STM measurements[159, 163], has a much weaker signature in transport and thermodynamic measurements[166]. Often the transport characterization of samples with lower residual resistivity ratios do not show a clear anomaly at T_{CDW} (see e.g. Fig. 7-1b), and the samples continue to display metallic behavior down to the superconducting transition. It has been subsequently understood that unlike a quasi-1D system, where large portions of the FS are gapped out by density wave order, the CDW in NbSe$_2$ exists over a small ($\sim 3\%$) portion of the FS. Unlike the well-understood superconducting phase in this material, the mechanism and spectral manifestation of the quasi-2D CDW in NbSe$_2$ continues to be a subject of debate, and will be detailed in § 6.3.

The coexistence and interplay of superconductivity and CDW orders in NbSe$_2$ has also received recent attention. Transport studies with hydrostatic pressure by Suderow et al.[160] demonstrated the suppression of CDW order (later confirmed by X-ray measurements[162]), and enhancement of superconducting order with increasing pressure, suggesting a possible competition between the two phases. Meanwhile, temperature-dependent ARPES measurements by Kiss et al.[161] indicated the enhancement of the superconducting gap magnitude over the FS regions connected by the CDW wavevector, suggesting that the presence of CDW order could boost superconductivity. In contrast, more recent ARPES work by Rahn et al.[165] at much lower temperatures suggests a possible momentum-space competition between CDW and superconductivity. The disagreement over the nature of interaction, or lack thereof, between these orders stems in part from the limited understanding of the CDW phase, which we will detail in the following section.

6.3   CDW in NbSe$_2$: Ongoing Debates

The density wave phase in NbSe$_2$ in particular, and dichalcogenides in general, has been a subject of much theoretical and experimental interest. Following the discovery of CDW order in dichalco-

genides, early theoretical work focussed on the emergence of the density wave instability from saddle point singularities in the density of states near ε_F[167]. Meanwhile, it was also realized that the conventional Peierls mechanism of density wave formation, based on the weak coupling limit of electron-phonon interactions, may not be adequate to describe the intermediate coupling physics in dichalcogenide systems[168], and that a description analogous to the Eliashberg theory for superconductivity[169] may need to be considered. However, few theoretical efforts were directed towards this.

A limiting factor in understanding the momentum space manifestation of the density wave was the lack of experimental and theoretical tools to determine the FS and band structure of NbSe$_2$ with adequate precision. This was duly rectified in the 90s with the emergence of angle-resolved photoemission and improved density functional theory techniques. However, despite extensive experimental and theoretical efforts over the past two decades[157, 161, 165, 170, 171], several key facts about its familiar tri-directional ($3Q$) CDW in NbSe$_2$ remain unresolved. Most notable among these are the role of FS nesting in determining its wavevector $\vec{q}_{3Q}$, and the magnitude of the spectral gap and its role in the energetics of the transition.

6.3.1 CDW Driving Mechanism
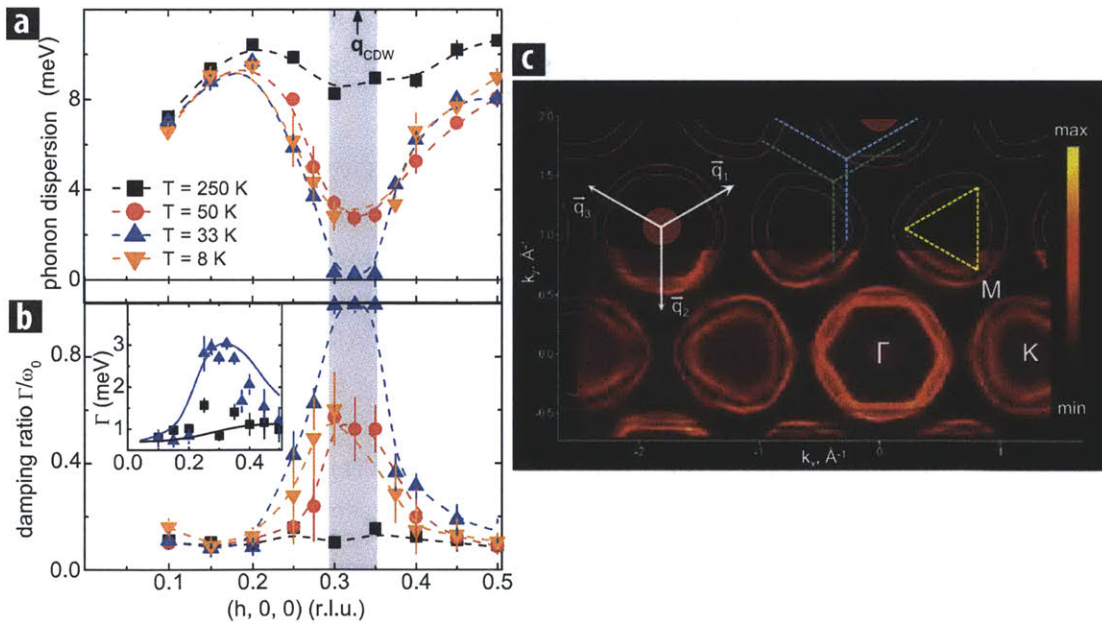
Figure 6-2: **Experimental Evidence for the Driving Mechanism of the CDW in NbSe$_2$.** (a-b) Inelastic X-ray scattering measurements of the dispersion of the phonon associated with the CDW. Unlike a typical Kohn anomaly, the softening of the phonon is found to extend over a broad range of wavevectors around q_{CDW} (shaded grey region), indicative of an electron-phonon coupling driven CDW (adapted from [157]). (b) The Fermi surface of NbSe$_2$ as measured by ARPES experiments, showing reduced intensity at regions of the inner K barrel connected by $\vec{q}_{3Q}$ (dahed light green lines), indicative of a FS nesting driven CDW (adapted from [170]).

The quasi-2D TMDCs, notably $NbSe_2$, are known to deviate from the picture of a sharp Kohn anomaly at the CDW wavevector. Angle-resolved photoemission (ARPES) studies of $NbSe_2$ have been unable to uniquely identify regions of the FS nested by the CDW wavevector $\vec{q}_{3Q}$. Different studies have reported the purported nested regions as being the Γ-barrel[172], the outer K-barrel[161], the inner K-barrel[165, 170] and unoccupied parts of the FS[173]. However, with improving precision and comparisons with DFT calculations, it is now reasonably well agreed upon that the end-points of the inner K-barrel (yellow points in Fig. 6-2b) are connected by $\vec{q}_{3Q}$. However, it is still debatable as to whether this is strong evidence for a FS nesting driven CDW transition.

Meanwhile, recent first-principles LDA calculations[149], ARPES studies[165] and inelastic X-ray scattering measurements[157] indicate the presence of a broadly peaked susceptibility and a soft, overdamped phonon over a wide range of wavevectors around $\vec{q}_{3Q}$, suggesting that the q-dependence of the electron-phonon coupling could possibly play an important role in driving the CDW transition.

6.3.2 CDW Spectral Gap
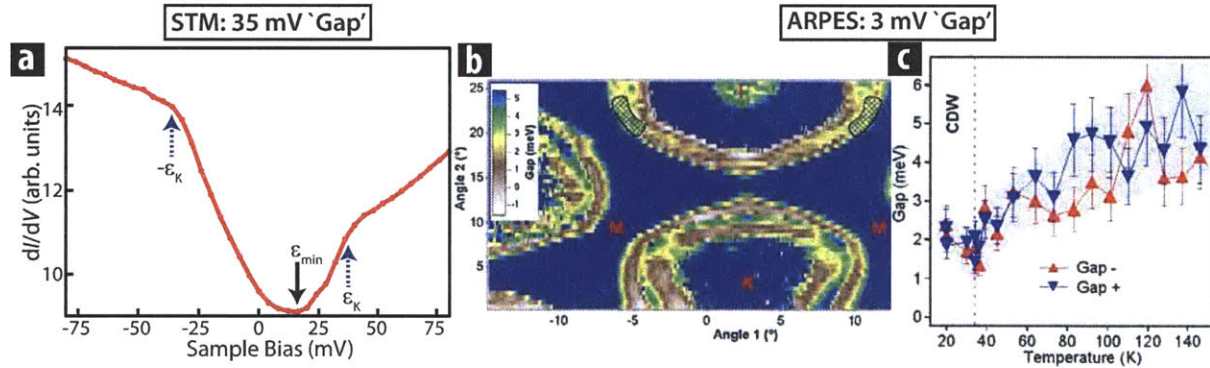
Figure 6-3: Spectral Gap of CDW in $NbSe_2$: STM vs. ARPES. (a) Average STM dI/dV spectrum, showing kinks at $\sim \pm 35\,mV$ (ε_K), the minimum ε_{min} offset from ε_F by $\sim 16\,mV$, and marked asymmetry about ε_F. Setpoint parameters: $V_0 = -80\,mV$; $R_J = 0.2\,G\Omega$; $V_{mod} = 3\,mV$. The ± 35 mV kinks have historically been interpreted as the CDW gap[45]. **(b)** ARPES measurements of the momentum-resolved spectral CDW gap using the shift of the spectral weight leading edge, compared with a reference in k-space. This technique shows a gap feature of 3–5 mV at regions nested by $\vec{q}_{3Q}$ (b) with an anomalous temperature dependence (c) (adapted from [170]).

The size of the spectral CDW gap in $NbSe_2$ is another issue of contention, with disagreements between STM and ARPES measurements corresponding to an order of magnitude.

Fig. 6-3a shows the typical STM spectrum recorded on $NbSe_2$. The spectrum has marked asymmetry about ε_F, with the spectral minimum centered at ~ 16 mV, in addition to prominent kinks at ± 35 mV ($\pm \varepsilon_K$). These ± 35 mV kinks in tunneling spectra have been historically identified as gap edges[45], and correspond to an anomalously large energy scale for the corresponding

T_{CDW} ($2\varepsilon_{\text{K}}/3.5k_{\text{B}}T_{\text{CDW}} \sim 7.05$).

While ARPES has historically been unable to locate a CDW gap in k-space, recent studies using leading edge shifts of spectral weight have identified a ~ 3 mV gap feature on the inner K-barrel[165, 170]. However, the magnitude and temperature dependence of the gap, as well as its role in the energetics of the CDW transition remain a subject of debate[149, 165]. Note that it has always been implicitly assumed, both in ARPES and STM studies, that the spectral gap is centered at the Fermi energy, ε_F.

These debated issues of the CDW driving mechanism and the spectral gap motivate our spectroscopic STM studies of $NbSe_2$.

Chapter 7

Quantum Phase Transition from Triangular to Stripe Charge Order in NbSe$_2$

Having motivated the key debated issues concerning the charge density wave in NbSe$_2$, we detail our experimental observations of a quantum interface between the known triangular CDW and a stripe CDW with a distinct wavelength, the latter unreported thus far. We show that the quantum phase transition between these two CDWs is tuned by local strain, and suggest the proximity of NbSe$_2$ to a density wave quantum critical point.

7.1   Material and Methods
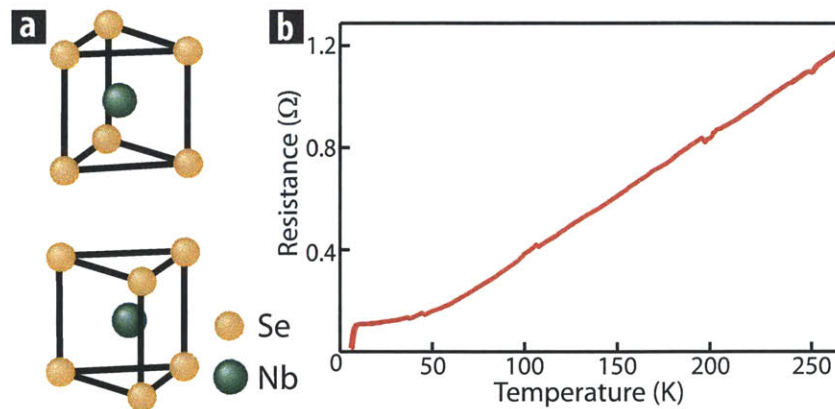
Figure 7-1: Crystal Structure and Sample Characterization. (a) The layered hexagonal crystal structure of $2H$-NbSe$_2$, with alternating sandwiches of Se-Nb-Se. **(b)** Temperature dependence of the resistance for the sample batch used for this study, showing a superconducting transition at $\sim 7\,\mathrm{K}$.

95

$2H$-NbSe$_2$ is a layered transition metal dichalcogenide with a hexagonal structure and D_{6h}^4 space group symmetry. The unit cell (Fig. 7-1a) consists of two sandwiches of Se-Nb-Se. The crystal typically cleaves between the neighboring Se layers, coupled by weak van der Waals forces.

Single crystals of $2H$-NbSe$_2$ were grown by chemical vapor transport using iodine as the transport agent. A transport characterization of the sample batch used in this work is shown in Fig. 7-1b. The superconducting transition is observed at $T_{SC} \sim 7$ K. The residual resistivity ratio (RRR), defined as the ratio of resistances $R(295\,\text{K})/R(7.5\,\text{K})$, is ~ 16.

Measurements were performed using a home-built STM at temperatures between $2 - 10$ K (unless indicated otherwise). Magnetic fields of up to 5 T were used to suppress the superconducting state as needed. Single crystals of $2H$-NbSe$_2$ were cleaved in situ in cryogenic ultrahigh-vacuum and inserted into the STM. A mechanically cut PtIr tip, cleaned by field emission and characterized on gold, was used for the measurements. Spectroscopy data were acquired using a lock-in technique at 1.115 kHz. The topographic and spectroscopic signatures of the $1Q$ ribbons detailed in this work have been verified with several tips.

7.2 The Triangular ($3Q$) Charge Density Wave
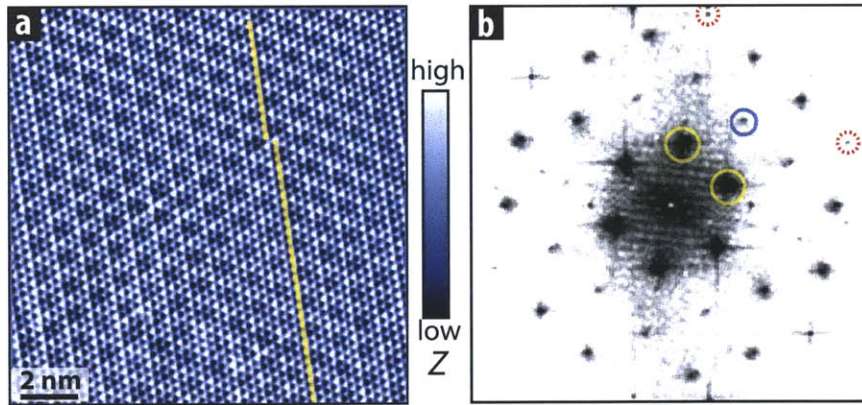
Figure 7-2: STM of the 3Q CDW. (a) Atomic resolution topograph showing the $\sim 3\,a_0$ periodic CDW. Yellow lines are overlaid on a one atom shift of the CDW maximum (phase slip). **(b)** Fourier Transform (FT) of a larger (~ 45 nm) topograph, displaying a $3Q$ CDW. Primary CDW wavevectors, $\vec{q}_1$ and $\vec{q}_2$ (yellow circles), a secondary CDW wavevector, $\vec{q}_1 + \vec{q}_2$ (blue circle) and Bragg vectors (dashed red circles) are indicated. Setpoint parameters: sample bias, $V_0 = -50$ mV (a), -60 mV (b); junction resistance, $R_J = 2.5$ GΩ (a), 0.1 GΩ (b).

Fig. 7-2a shows the prototypical low temperature STM topograph acquired on NbSe$_2$, with an atomically resolved hexagonal lattice with periodicity $a_0 = 3.45$ Å. In addition, we note the presence of a $3a_0$ periodic superstructure modulation along all three lattice directions. This modulation arises from the CDW phase in NbSe$_2$, which is locally commensurate. Occasional CDW phase slips are seen in topographs, as indicated by the yellow lines in Fig. 7-2a, resulting in an overall incommensurate periodicity.

The Fourier Transform (FT) of such a topograph is shown in Fig. 7-2b. The notable features include Bragg peaks (dashed red), corresponding to the atomic periodicity and primary CDW peaks (yellow circles), indicating a CDW periodicity of $\vec{q}_{3Q} \simeq 0.328\,\vec{Q}_0$ (i.e. wavelength, $\lambda_{3Q} \simeq 3.05\,a_0$), where $\vec{Q}_0$ is the Bragg vector. The 2% deviation from a commensurate CDW below 10 K, as measured from STM, is consistent with previous bulk X-ray measurements on NbSe$_2$[159, 162, 174]. However, in contrast to previous X-ray work[162], we note the presence of a secondary CDW wavevector in our FT (Fig. 7-2b, blue circle). This is equivalent to the vector sum of primary CDW wavevectors, and confirms the microscopic $3Q$ nature of the CDW on the surface. The absence of this peak in X-ray measurements[162] could be attributed to a slight difference between the CDWs on the surface and in the bulk. It is possible that the unambiguously $3Q$ CDW on the surface decouples to spatially separated $1Q$ phases in the bulk. Importantly, the CDW modulation periodicity is consistent between the bulk and the surface.

7.3 A Unidirectional ($1Q$) Charge Density Wave
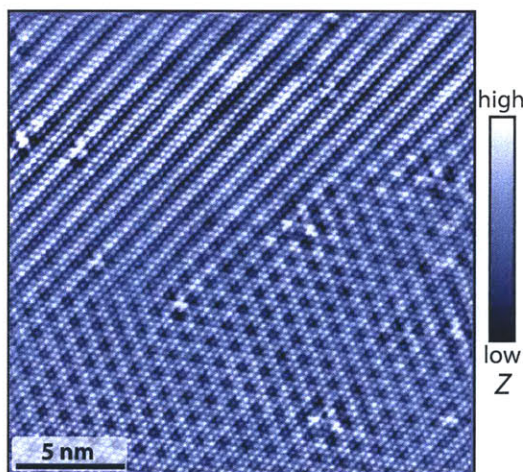
Figure 7-3: The $1Q - 3Q$ Interface. Topograph showing an atomically smooth interface between the $3Q$ (bottom) and $1Q$ (top) CDWs. The topograph has been leveled by removing a polynomial background to clearly show the CDW interface. Setpoint parameters: $V_0 = -50\,\mathrm{mV}$; $R_J = 1\,\mathrm{G\Omega}$.

Our primary experimental discovery is shown in Fig. 7-3. In some sample regions, we find the $3Q$ CDW forming an atomically smooth interface with a hitherto unreported unidirectional ($1Q$) CDW. The $1Q$ CDW has a unique wavevector $\vec{q}_{1Q}$ along a single $3Q$ direction with a visibly different periodicity, and the two CDWs smoothly merge over a few nanometer length scale. We note the presence of such interfaces at temperatures at our base temperature (2 K).

Spatial modulations in CDW systems have been studied extensively by STM over the past two decades[175]. Several of these systems display inhomogenous phases near the transition temperature, T_{CDW}[154, 175]. For example, observations of short range hexatic order above T_{CDW}[176], consistent with a 2D melting description[177], have been reported in some dichalcogenide sys-

tems. In other systems, notably $2H$-TaSe$_2$, a triclinic CDW ($q_1 = q_2 \neq q_3$) has been reported at temperatures above T_{comm}, corresponding to the transition from an incommensurate CDW to the commensurate phase[154, 175]. The presence of impurities has been shown to pin the CDW even above T_{CDW}[176, 178], and in some cases can lead to thermally induced unidirectional order[179]. Meanwhile at low temperatures, the relative strengths of CDW order along the three lattice directions has been found to vary even at low temperatures, attributed to chirality of the order parameters[180] and polaronic effects[181]. Finally, local annealing of dichalcogenide samples has been shown to generate structural interfaces between $2H$ and $1T$ polytypes, leading to CDWs with different periodicities ($\sim 3a_0$ vs. $\sim \sqrt{13}a_0$), oriented $\sim 13°$ with respect to each other[182].

In contrast, our observation of the CDW interface persist down to temperatures $T \ll T_{\mathrm{CDW}}$, ruling out any phases arising from thermal fluctuations. That the $1Q$ CDW is oriented along a single $3Q$ direction, and further that the CDWs form an atomically smooth interface with no lattice discontinuities, rules out the possibility of a NbSe$_2$ polytype interface. Finally, the absence of CDW modulations along the other two lattice directions rule out chiral order or smooth spatial variation of order parameters.

Therefore, we claim that our observations represent a quantum ($T = 0$) interface between the known $3Q$ CDW on NbSe$_2$ and a unidirectional ($1Q$) CDW with a distinct wavelength, the latter examined in more detail below.

7.3.1 Topography of the $1Q$ Charge Density Wave
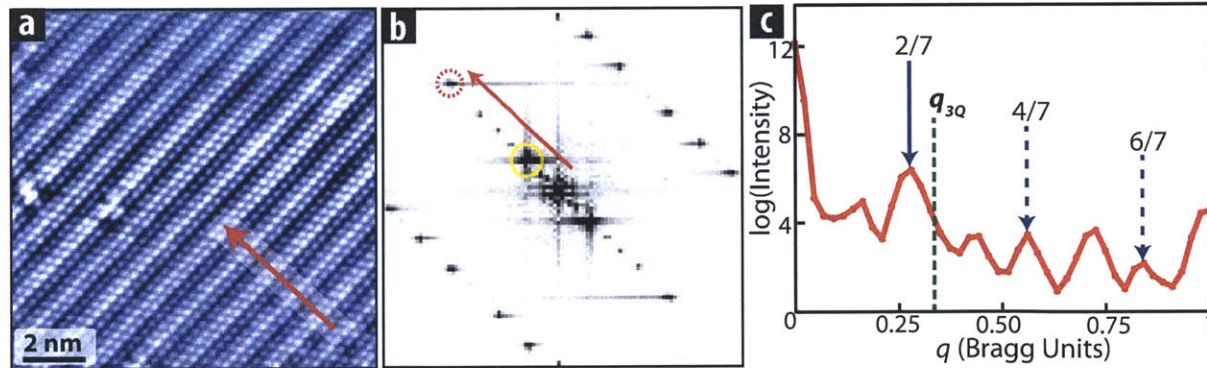
Figure 7-4: The $1Q - 3Q$ Interface. (a) A zoom-in STM topograph of the top left quadrant of Fig. 7-3, clearly showing the $1Q$ CDW. The red arrow points along the $1Q$ CDW direction ($\vec{q}_{1Q}$). **(b)** FT of the out-of-feedback current at $+50\,\mathrm{mV}$ over the region in (a). The dominant CDW wavevector (yellow circle) and Bragg vector (dashed red circle) are indicated. **(c)** Linecut of the FT intensity parallel to the red line in (b) from the center to the Bragg peak, in units of the Bragg vector $\vec{Q}_0$. The dominant peak, $q_{1Q} \simeq 2/7Q_0$ (solid blue arrow) and its harmonics (dashed blue arrows) are identified, and are distinct from the $3Q$ wavevector q_{3Q} (dashed green line). Setpoint parameters: $V_{\mathrm{sample}} = -50\,\mathrm{mV}$; $R_{\mathrm{J}} = 0.2\,\mathrm{G\Omega}$.

Fig. 7-4a shows a zoom-in topograph of the $1Q$ CDW region, with the red arrow parallel to the CDW wavevector $\vec{q}_{1Q}$. The FT of the out-of-feedback current over this region (Fig. 7-4a) shows

the reciprocal space signature of the unidirectional CDW. In addition to Bragg peaks (dashed red circles), we see a prominent peak at $\vec{q}_{1Q} \simeq 0.286 \, \vec{Q}_0$ (yellow circle), corresponding to a wavelength $\lambda_{1Q} \simeq 3.5 \, a_0$, 15% larger in magnitude than λ_{3Q}. A more careful examination of the topograph suggests the presence of a $\sim 7a_0$ periodicity as well. This, and the other periodicities associated with the 1Q CDW can be visualized by extracting a FT linecut along along $\vec{q}_{1Q}$, shown in Fig. 7-4c. We find that the linecut consists of six peaks (excluding the Bragg peak), corresponding to harmonics of $1/7 \, Q_0$, with the dominant peak, $q_{1Q} \simeq 2/7 \, Q_0$, corresponding to the fundamental 1Q CDW periodicity.

7.4 Topographic 'Ribbons' Pinning the 1Q CDW
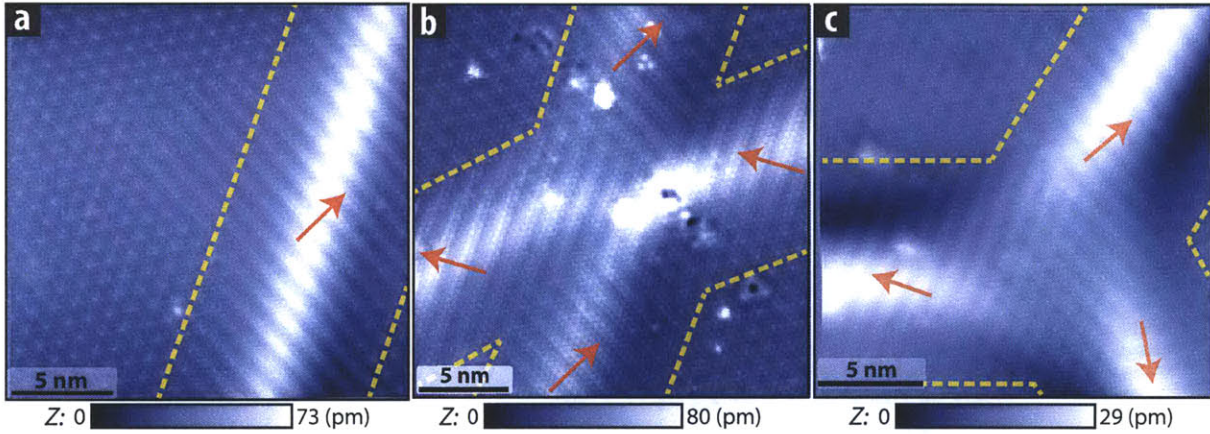
Figure 7-5: Topographic Ribbons and the 1Q CDW. (a) Topograph showing formation of 1Q CDW along a 'ribbon'. Ribbons are typically $10 - 20$ nm in width, and elevated by $20 - 40$ pm. Dashed yellow lines indicate the approximate extent of the ribbon; the red arrow points along the 1Q CDW direction ($\vec{q}_{1Q}$). **(b, c)** Topographs showing 'ribbons' of unidirectional (1Q) CDW, intersecting to form an X-junction (b) and a Y-junction (c), with CDW wavevector $\vec{q}_{1Q}$ varying between the arms. Setpoint parameters: $V_{\mathrm{sample}} = -50$ mV (a-c); $R_J = 5$ GΩ (a,b), 1 GΩ (c).

The 1Q CDW typically appears in regions which persist in one direction with apparent $20 - 40$ pm topographic elevation, forming a $10 - 20$ nm wide 'ribbon' structure (Fig. 7-5a).These ribbons are found to extend across the entire field-of-view accessible to our STM, and terminate only upon intersecting with another such ribbon oriented differently, forming $X-$ and $Y-$junctions (Fig. 7-5b-c). The confinement of the unidirectional CDW to such topographically elevated features suggests that strain tunes the transition between the 1Q and 3Q quantum phases. The observation of X and Y-junctions between ribbons with differently oriented $\vec{q}_{1Q}$ (Fig. 7-5b-c) rules out extrinsic uniaxial strain and suggests instead locally varying strain, perhaps due to underlying defects causing nanoscale buckling of the top few atomic layers.

We note that the topographic elevation $z_{\mathrm{STM}}(\vec{r}, V_0, I_0)$ as measured by maintaining a constant current I_0 with bias setpoint V_0 at lateral tip position $\vec{r} \equiv (x, y)$ can be given by

$$z_{\text{STM}}(\vec{r}, V_0, I_0) \simeq z_{\text{T}}(\vec{r}) + \frac{1}{\kappa(\vec{r})} \cdot \ln \left(\frac{I_0}{\int_0^{V_0} dV \, eD(\vec{r}, eV)} \right) \tag{7.1}$$

Here $z_T(\vec{r})$ is the true topographic corrugation of the sample, $\kappa(\vec{r})$ is a measure of the local tunnel barrier height (LBH), and $D(\vec{r}, eV)$ is the local density of states (LDOS) of the sample at energy eV. Because of the logarithmic sensitivity of $z_{\text{STM}}(\vec{r}, V_0, I_0)$ to the integral of the LDOS from the Fermi energy, ε_F (corresponding to $V = 0$) up to the bias setpoint eV_0, STM topographs may contain electronic artifacts masquerading as geometric effects. Therefore, we present two pieces of evidence for the true geometric elevation of these ribbons.

7.4.1 Evidence for the Topographic Origin of the $1Q$ Ribbons
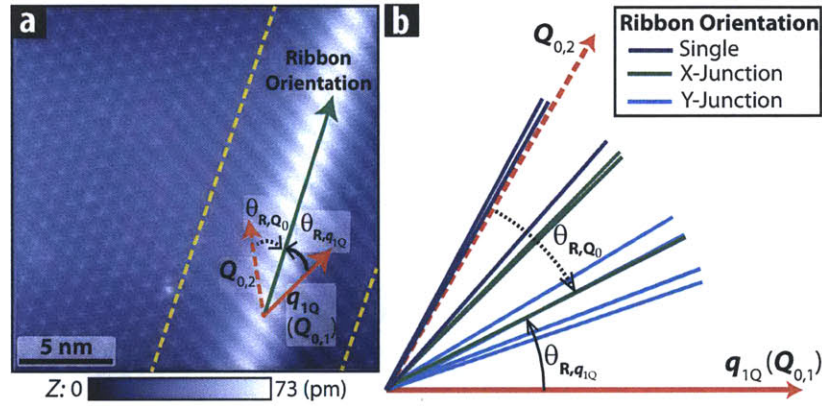
Figure 7-6: $1Q$ 'Ribbons': Orientation. (a) STM topograph of a $1Q - 3Q$ interface (top arm of X-junction, also shown in Fig. 7-5a), demonstrating the definitions of the relative orientations θ_{R,Q_0}, between the ribbon (green arrow) and the nearest Bragg vector (dashed red arrow), and $\theta_{\text{R},q_{1Q}}$, between the ribbon and $1Q$ wavevector $\vec{q}_{1Q}$ (solid red arrow). (b) A visual illustration of the spread of values in Tbl. 7.1. The dark blue (single), green (X-junction) and cyan (Y-junction) lines describe the orientation of the various ribbons with respect to the $1Q$ wavevector $\vec{q}_{1Q}$ along the $\vec{Q}_{0,1}$ Bragg vector (solid red arrow) and another Bragg vector $\vec{Q}_{0,2}$ (dashed red arrow).

First, a tabulation of the relative orientation $\theta_{\text{R},\vec{Q}_0}$ of the ribbon to the nearest Bragg vector of the underlying hexagonal lattice for the various ribbons imaged in the study shows a seemingly random spread from $-30°$ to $30°$ - the full range of available angles (Tbl. 7.1, Fig. 7-6b). Furthermore, these ribbon structures can intersect to form $X-$ as well as $Y-$junctions (Fig. 7-5b-c), and the angle between intersecting ribbons varies from $40°$ to $60°$. The fact that ribbon orientation does not respect lattice symmetry strongly suggests a true geometric, rather than electronic origin of their apparent height. We contrast this observation with enhanced STM topographic corrugation associated with predominantly electronic features in a wide range of other materials, which respect the symmetry of the hexagonal[56, 71] or square[156] lattice.

Second, the measured height of these ribbons in STM topographs exhibits $< 5\%$ dependence

Ribbon Type	$\theta_{R,\vec{Q}_0}(°)$	$\theta_{R,\vec{q}_{1Q}}(°)$
X-Junction	-28	32
X-Junction	-16	44
X-Junction	-14	46
X-Junction	27	27
Y-Junction	19	19
Y-Junction	21	21
Y-Junction	28	28
Single	1	61
Single	2	62
Single	-11	49

Table 7.1: A table detailing the values of the angular orientations $\theta_{R,\vec{Q}_0}$ and $\theta_{R,\vec{q}_{1Q}}$ (defined in Fig. 7-6a) observed in the various $1Q$ ribbons studied in this work, with the first entry corresponding to Fig. 7-6a.
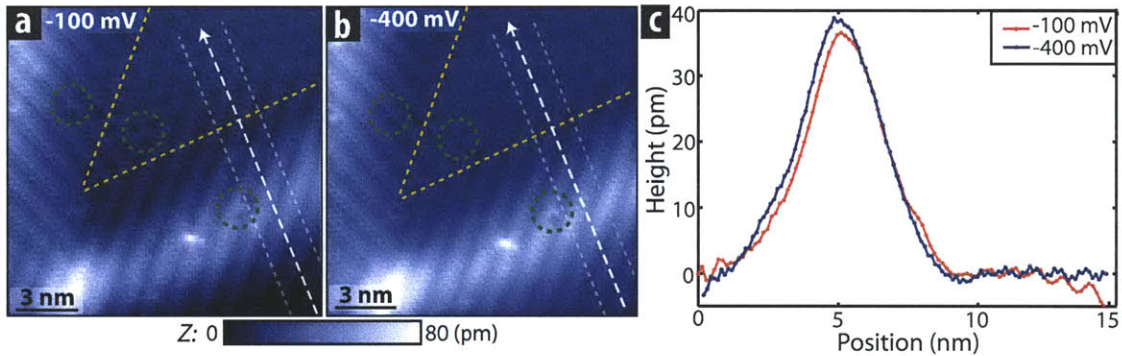
Figure 7-7: $1Q$ 'Ribbons': Bias Setpoint Dependence. **(a, b)** Topographs of $1Q$ ribbons over the same spatial area acquired with different bias setpoints: -100 mV (*A*) and -400 mV (*B*), with $R_J = 10$ GΩ in both. The dashed yellow lines indicate the approximate extent of the ribbons, and the dashed green circles enclose triangular impurities, visible in B with a $50 - 70\%$ larger apparent height than in A. **(C)** Linecuts taken through the topographs in A (red) and B (blue) transverse to the lower ribbon, along the dashed white arrows. The measured ribbon height varies less than 5% between bias setpoints -100 mV and -400 mV. The linecuts have been laterally averaged over a 3 nm width indicated by the dashed grey lines..

on bias setpoint within 400 mV below the Fermi energy (Fig. 7-7). We note that this energy range over which the measured height of the ribbons is invariant is much larger than the spectral range of CDW variation in the DOS ($\sim$ 50 mV). We further note the contrast between the bias-independent ribbons, and single atom impurity resonances, whose measured 'height' varies by $50 - 70\%$ between Fig. 7-7a and b. Therefore we conclude that the measured height ($20 - 40$ pm) and width ($10 - 20$ nm) of these ribbons has a predominantly geometric origin.

Having established the topographic origin of these ribbons (Fig. 7-6 and Fig. 7-7), we suggest that these ribbons are likely a topographic rippling of the top few layers. These ribbons may arise during the cleaving process due to underlying growth defects which can intercalate between Se-Nb-Se sandwich layers. We note that similar topographic ribbon deformations have recently been observed in another layered chalcogenide (Bi_2Te_3)[14].
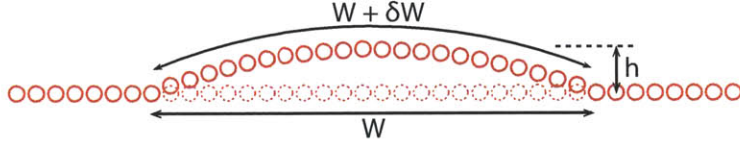
Figure 7-8: Schematic of the Ribbon Distortion. A cartoon representation of the lattice distortion caused by the formation of such a ribbon, modeled as a half period of a sinusoid. The red circles correspond to rows of displaced Se atoms, while the dashed red circles represent their original undistorted positions. The ribbon has height h (40 pm) and width W (10 nm), resulting in a total lateral distortion of $\delta W \sim 45$ pm across the ribbon.

7.4.2 Estimating the Strain in the Ribbon Region

We estimate the in-plane and out-of-plane lattice strain associated with the topographic ribbon features. Using the maximum topographic elevation of an observed ribbon (40 pm), we can put an upper limit on the out-of-plane distortion by assuming that a minimum of 2 sandwich layers are elevated (any fewer, and the defects causing the elevation would be likely visible in our topographs). The out of plane distortion is therefore $\lesssim 3\%$ ($40\,\text{pm}/12.54$ Å) of the unit cell spacing. To measure the in-plane distortion, we first use the Lawler-Fujita algorithm[183], which can determine the lateral location of atoms with precision $\sim 2\%$ of the lattice spacing[184, 185]. With this algorithm, we do not observe any change in the lattice constant across the ribbon, which places a direct experimental upper limit on the in-plane distortion of $\sim 2\%$.

However, we can estimate the actual in-plane distortion indirectly from the measured out-of-plane distortion, by modeling the ribbon as a half-period of a sinusoid with height h (40 pm) and width W (10 nm) (Fig. 7-8). The total lateral deformation due to such a ribbon is $\delta W \sim 45\,\text{pm}$, corresponding to $\sim 0.06\%$ of the lattice spacing. As this is well below the resolution of the Lawler-Fujita algorithm, it is not surprising that the in-plane distortion is not detectable in STM topographs. From the upper bounds of 3% on the vertical strain and 0.06% on the lateral strain, we note that the magnitude of the strain field leading to the formation of these ribbons is moderate, in comparison to some other correlated materials[186, 187]. We also note that while the magnitude of lattice distortion of these ribbons may seem small in the context of the observed quantum phase inhomogeneity, a comparison with other known materials suggests that strain of this magnitude can be sufficient to drive a transition to the unidirectional CDW phase[155].

We previously discussed the ribbon orientation with respect to the lattice ($\theta_{R,\vec{Q}_0}$); we now consider the ribbon orientation with respect to the $1Q$ CDW wavevector ($\theta_{R,\vec{q}_{1Q}}$), also detailed in Fig. 7-6b-c. In a simple picture of the strained ribbon structure, we would expect the ribbon-induced strain to couple strongly to the $1Q$ CDW orientation either parallel or perpendicular to the ribbon, and thus we would expect to observe values of $\theta_{R,q_{1Q}}$ either between $0-30°$ or between $60-90°$. Yet we often find $\theta_{R,q_{1Q}}$ to be in the $30-60°$ range as well. Insufficient statistics prevent us from inferring a clear connection between ribbon orientation and $\vec{q}_{1Q}$ orientation, but the wide

distribution of relative angles suggests the complexity of the interaction.

7.5 Landau Description of the $1Q - 3Q$ Quantum Phase Transition

Our work motivates the utility of the $1Q-3Q$ interface in NbSe$_2$ as a platform to explore competing quantum phases in the weakly correlated limit, as a step towards understanding them in strongly correlated systems. In the Landau picture of CDWs[188], a quantum phase transition between $3Q$ and $1Q$ states can arise by tuning the coefficient of the interaction term between the three inequivalent CDW propagation directions (though in our case, the magnitude of q differs between the two states). In NbSe$_2$, even at low temperatures $T \ll T_{CDW}$, where the amplitude of the order parameter is already large, moderate strain is seen to have a strong influence, indicating that the system is intrinsically close to the QCP separating these states. We note that a related phase transition between the observed $1Q$ CDW phase and a 'hidden' $2Q$ phase has been suggested, but not directly visualized, in the rare-earth tritellurides[155, 189].

7.5.1 Landau Description of the $1Q - 3Q$ Transition with Equal Wavevectors

To understand how moderate strain can drive a $1Q - 3Q$ transition in NbSe$_2$ at temperatures $T \ll T_{CDW}$ with CDW wavevectors identical in magnitude, consider the general form of the Landau free energy[188]:

$$\mathcal{F} = \int dx \left[A\,\alpha^2 + B\,\alpha^3 + C\,\alpha^4 + D\left\{ |\psi_1\psi_2|^2 + |\psi_2\psi_3|^2 + |\psi_1\psi_2|^2 \right\} \right] \qquad (7.2)$$

Here, the charge density modulation is described as $\rho(x) = \rho_0(x)\,[1 + \alpha]$, with $\alpha \equiv \psi_1 + \psi_2 + \psi_3$, and the order parameters $\psi_{1,2,3}$ corresponding to the three inequivalent CDW propagation directions. The final term in this expansion, proportional to D, represents the competition between the different CDW components over the available states at the FS. The $3Q$ CDW state with all $\psi_{1,2,3}$ non-zero is the minimum energy state if $D > 3C/2$[188]. For smaller values of D, a $1Q$ state with $\psi_i \neq 0$ but $\psi_j = \psi_k = 0$ results.

Alternatively, the $1Q$ state can be stabilized by the application of strain, which favors one of the CDW propagation vectors over all others. Our observations indicate that a moderate strain field can drive the transition, even at temperatures well below T_{CDW}. At such low temperatures, higher order terms contribute more strongly to $\mathcal{F}$, so that the large influence of only moderate strain can be taken as an indication that the $1Q$ and $3Q$ states are close in energy. The system may thus be intrinsically close to the quantum critical point separating these states.

7.5.2 Landau Description of the $1Q - 3Q$ Transition with Change in Wavevectors

Our observations correspond to a transition not only from a $3Q$ to a $1Q$ phase, but also to a change in the CDW periodicity, indicative of weak nesting at the CDW wavevector in NbSe$_2$. In this case, the Landau free energy description is more involved, and can be expressed more generally as

$$\mathcal{F} = \int \mathrm{d}x \left[A\,\alpha^2 + B\,\alpha^3 + C\,\alpha^4 + D\left\{ |\psi_1\psi_2|^2 + |\psi_2\psi_3|^2 + |\psi_1\psi_2|^2 \right\} \right. \tag{7.3}$$

$$\left. + E\sum_j \left| \left(\vec{q}_j \cdot \vec{\nabla} - i\vec{q}_j^{\,2} \right)\psi_j \right|^2 + F\sum_j \left| \vec{q}_j \times \vec{\nabla}\psi_j \right|^2 \right] \tag{7.4}$$

In comparison to Eqn. 7.2, we now include two additional terms that depend on the magnitude of the CDW wavevectors $\{\vec{q}_j\}$. The term proportional to F ensures that the directions of the CDW components are aligned with those of the preferred wave vectors $\vec{q}_{1,2,3}$, while the term proportional to E sets the sizes of the CDW propagation vectors.

If the Fermi surface is well-nested, only one possible set of propagation vectors $\vec{q}_{1,2,3}$ needs to be taken into account. However, in the presence of only weak nesting and an extended range of soft phonon modes, as is the case in NbSe$_2$[157], there may be multiple choices for the sizes of the CDW propagation vectors which are close in energy. This situation can be included in the Landau free energy by generalizing the term proportional to E, and writing it as

$$\mathcal{F}_{\text{no nesting}} \propto \int \mathrm{d}x \sum_{\vec{q}} E(\vec{q}) \sum_j \left| \left(\vec{q}_j \cdot \vec{\nabla} - i\vec{q}_j^{\,2} \right)\psi_j \right|^2 \tag{7.5}$$

In the well-nested case, the function $E(\vec{q})$ is sharply peaked around the nesting vector $\vec{q}_0$, and may be approximated by $E\delta_{\vec{q},\vec{q}_0}$. In the case of NbSe$_2$ on the other hand, the flat and shallow phonon spectrum suggests that the function $E(\vec{q})$ may likewise be relatively flat, thus allowing even relatively small external influences like uniaxial strain to have a significant effect on the preferred size of the CDW propagation vector.

Additionally, the presence of uniaxial strain also influences the other terms in the free energy by explicitly breaking the three-fold rotational symmetry of the material. Ignoring terms like $\int \mathrm{d}x\,\psi_1\psi_2$, which will integrate to zero, and setting $B = 0$, the first line of Eqn. 7.3 in the presence of uniaxial strain becomes

$$\mathcal{F}_{\text{strain}} \propto \int \mathrm{d}x \sum_j \left[A_j\,|\psi_j|^2 + C_j\,|\psi_j|^4 + D_j'\,|\psi_{j+1}\psi_{j+2}|^2 \right] \tag{7.6}$$

Here j is defined modulo 3, and D' includes the cross terms originating from the term proportional to C in Eqn. 7.3. In the presence of uniaxial strain, the coefficients A_j, B_j and C_j may be different for different CDW components j. If the strain on the sample is large enough, a situation could arise in which A_j is negative for one of the components, but positive for the other two. This would then result in a $1Q$ rather than a $3Q$ structure. In the strain ribbons on NbSe$_2$ however, the strain is relatively moderate, and is observed to result in a $1Q$ structure even far below the CDW transition temperature. Since we know that in the $3Q$ state all components A_j become more negative as temperature is lowered below T_{CDW}, it would require an increasingly large strain to force the system into a $1Q$ state this way. It is therefore likely that the dominant effect of the presence of moderate uniaxial strain in NbSe$_2$ is to change the values of the components D'_j .

That only moderate strain suffices to favour the $1Q$ state over the original $3Q$ state, even at low temperatures where the higher order terms in the Landau expansion acquire more weight, suggests that the $1Q$ and $3Q$ states were already close in energy. The system may thus be intrinsically close to the quantum critical point separating these states.

7.5.3 Cuprate Charge Order: 'Stripes' v. 'Checkerboard'
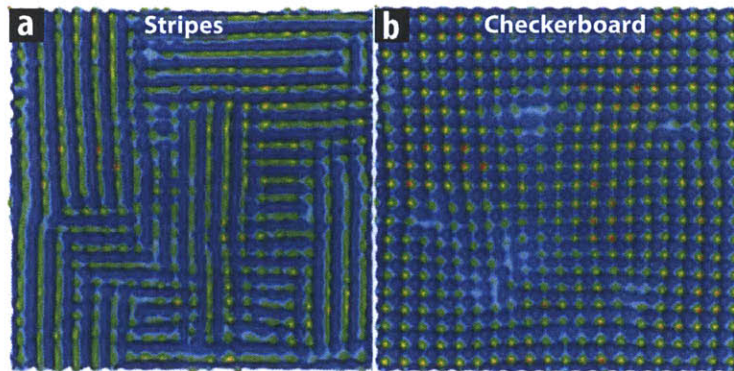
Figure 7-9: Schematic of Possible Charge Order in the Cuprates. (a-b) Pictorial depiction of possible static charge order in the cuprates, corresponding to unidirectional 'stripes' (a) or a bidirectional checkerboard (b), lying on either side of a quantum critical point.

Our observation of the local effect of even moderate strain in driving a quantum phase transition between density waves calls for a reinvestigation of possible phase inhomogeneity in other strongly correlated systems, where larger strain may occur[186, 187].

In the cuprate superconductors, an analogous phase boundary between unidirectional ($1Q$) charge 'stripes' and bidirectional ($2Q$) 'checkerboard' (Fig. 7-9) has been predicted[190, 191]. The introduction of quenched disorder results in discommensurations in the $2Q$ phase and disordered orientational order in the $1Q$ phase, making them hard to distinguish - especially in the cuprate BSCCO, thought to be in proximity to the $1Q - 2Q$ phase boundary[190, 191]. Recent STM studies of the $\sim 4\,a_0$ charge order in BSCCO have had conflicting interpretations, with independent

suggestions of fluctuating $2Q$ and $1Q$ order[156, 192]. However, the influence of strain, from the supermodulation lattice buckling, or from randomly distributed dopants, is seldom accounted for.

Previous studies have shown that both these strain phenomena correlate with nanoscale electronic inhomogeneity[186, 193]. A possible explanation is local stabilization of the $1Q$ state, producing $1Q-2Q$ and $1Q-1Q$ interfaces, analogous to Fig. 7-5. While the presence of strong disorder (up to 12% strain variations on a nanometer length scale[186]) complicates the interpretations in BSCCO, we stress the importance of isolating and modeling strain effects for better understanding and control of the phase transitions in cuprates. Finally, the microscopic visualization of the role of strain in stabilizing new order suggests a controlled route towards engineering novel quantum phases and interfaces and studying symmetry breaking in strongly correlated materials. In this regard, we suggest a connection to the emerging importance of strain as a route to high-T_C superconductivity in novel iron-based materials[194, 195].

Chapter 8

Strong Coupling Origin of the Charge Density Wave in NbSe$_2$

We use our observation of a $1Q - 3Q$ charge density wave interface on NbSe$_2$, in conjunction with band structure calculations, to resolve the longstanding questions of the CDW wavevector and spectral gap. First, we use the distinct CDW wavelengths to demonstrate that FS nesting plays a negligible role in setting their magnitude. Second, we use the distinct tunneling spectra of the $1Q$ CDW region to disentangle the $3Q$ CDW spectra, and expose a particle-hole asymmetric gap, riding on top of a strong inelastic background.

8.1 Phenomenological Picture of a 'Nearly Commensurate' $1Q$ CDW
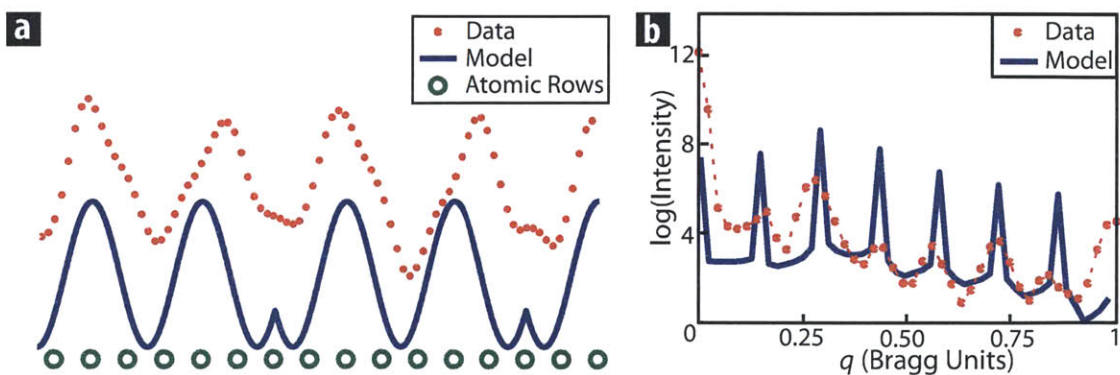
Figure 8-1: Phenomenological Model of the $1Q$ CDW. (a) Phenomenological model of the observed $1Q$ CDW wavelength, $\lambda_{1Q} \simeq 3.5\,a_0$. The atomic periodicity is indicated by green circles and the phase of the CDW order parameter from the model is shown in blue[174]. A topographic linecut (red dots) is extracted along the red arrow in Fig. 7-4a (along $\vec{q}_{1Q}$), filtered to remove atomic corrugations, and overlaid for comparison. (b) Simulated FT intensity (blue line) from the cartoon CDW modulation, for comparison with experimental FT peak positions (red dots, shown in Fig. 7-4c).

The dominant Fourier peak for the 1Q modulation, $\vec{q}_{1Q} \simeq 2/7\,\vec{Q}_0$ (Fig. 7-4c), corresponds to a wavelength, $\lambda_{1Q} \simeq 3.5\,a_0$. No similar periodicity has thus far been reported in any TMDC system[154]. In addition, as noted in § 7.3, the FT of the 1Q CDW region shows a rich harmonic structure.

We develop a phenomenological understanding of the 1Q harmonic structure following McMillan's Landau theory[174, 188]. Rather than having a uniform $3.5\,a_0$ charge modulation, the system could lower its energy by locking the charge modulation to the lattice with $3\,a_0$ periodicity. This would require compensation by a one atom phase slip every two oscillations, corresponding to a $2\pi/3$ discommensuration, as shown in Fig. 8-1a[174]. The resulting harmonic structure shown in Fig. 8-1b (blue) reproduces all observed peak positions (red dots). Moreover, the rich harmonic content we observe is another indication of the strong coupling of the electronic modulation to the lattice. An even better agreement with relative peak heights could be obtained by considering spatial variations in the order parameter amplitude[174].

8.2 Band Structure of NbSe$_2$
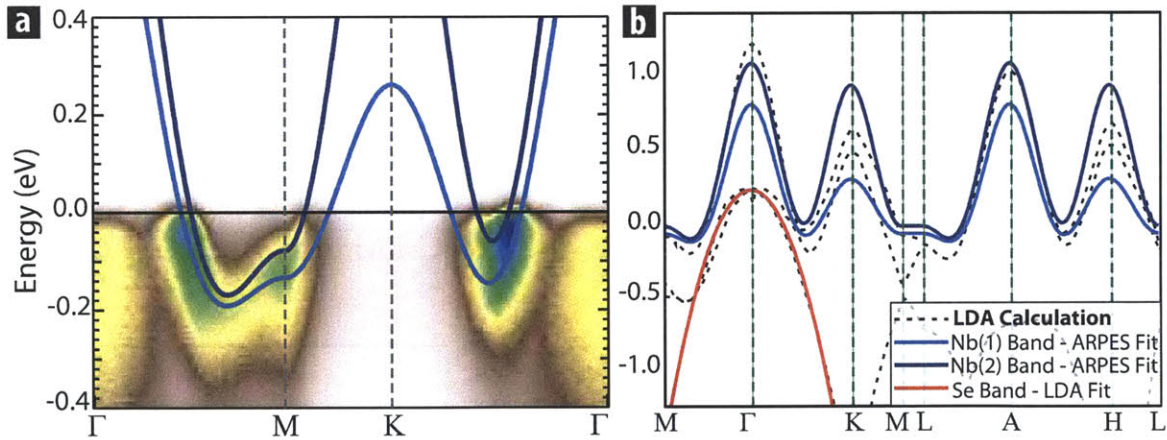
Figure 8-2: Tight-Binding Fit to the ARPES Measured NbSe$_2$ Band Structure. (a) ARPES measurements of the band structure of NbSe$_2$ along high symmetry directions in reciprocal space, recorded at 33 K. The ARPES data is fit using a tight-binding approximation, to describe the dispersion of the two Nb-4d bands (light and dark blue)[165]. **(b)** The calculated band structure of 2H-NbSe$_2$ along high-symmetry directions, showing the two Nb-4d bands obtained from (a), and the Se-4p band, modeled as a parabolic fit to LDA calculations of Johannes *et al.*[149], compared with the LDA calculations (dashed black lines).

The band structure of NbSe$_2$ close to ε_F consists of two Nb-4d derived bands and one Se-4p 'pancake'-shaped hole pocket[149, 196]. Close to ε_F, the Se-4p pancake-shaped hole pocket which surrounds the Γ-point can be modeled by a simple quadratic form,

$$E = A \cdot \frac{a_0^2}{4\pi^2}\left(k_x^2 + k_y^2\right) + B \tag{8.1}$$

With the values of $A = -5.4\,$eV and $B = -0.65\,$eV, this model accurately reproduces the dispersion obtained in LDA calculations by Johannes *et al.*[149], as shown in Fig. 8-2b.

To model the Nb-4d bands, we use a tight-binding fit to the band structure observed in ARPES experiments (Fig. 8-2a, [165]). We find that a small ($\sim +16\,$meV) offset in the chemical potential relative to the parameters used by Rahn *et al.*[165] was needed to reproduce the observed DOS from STM measurements. This offset is within the accuracy of the tight-binding fitting scheme. The band energies of the tight-binding description are given by [165]:

$$
\begin{aligned}
E = t_0 &+ t_1[2\cos\xi\cos\eta + \cos 2\xi]\\
&+ t_2[2\cos 3\xi\cos\eta + \cos 2\eta]\\
&+ t_3[2\cos 2\xi\cos 2\eta + \cos 4\xi]\\
&+ t_4[\cos\xi\cos 3\eta + \cos 5\xi\cos\eta + \cos 4\xi\cos 2\eta]\\
&+ t_5[2\cos 3\xi\cos 3\eta + \cos 6\xi]
\end{aligned}
\tag{8.2}
$$

where $\xi = \frac{1}{2}k_x a_0$ and $\eta = \frac{1}{2}\sqrt{3}k_y a_0$ and k_y is along $\Gamma - M$. The values of the tight binding parameters (including the offset) used in this work are outlined in Tbl. 8.1. Fig. 8-3a-b show a direct comparison of the CECs generated using the tight-binding fit with the ARPES data acquired at ε_F and -0.1 eV.

Parameter	Nb Band (1)	Nb Band (2)
t_0	26.9	219.0
t_1	86.8	46.0
t_2	139.9	257.5
t_3	29.6	4.4
t_4	3.5	-15.0
t_5	3.3	6.0

Table 8.1: Tight-binding parameters for the two Nb bands (in meV), based on fits to the ARPES data of Rahn *et al.*[165].

The Fermi surface of NbSe$_2$ therefore derives from the two Nb bands and the Se pancake pocket, shown in Fig. 8-3c. It consists of three barrels around the Γ-point, from each of the three bands, and two barrels around the K-point deriving from the two Nb bands. While previous ARPES work indicated that the CDW corresponded to nesting around the Γ-point[172], more recent studies suggest that gapped regions of the FS on the inner Nb barrel at the K-point are nested by $\vec{q}_{3Q}$[165, 170]. In addition, we note the presence of a van Hove singularity at ~ -80 mV associated with the triangular features in Fig. 8-3b.
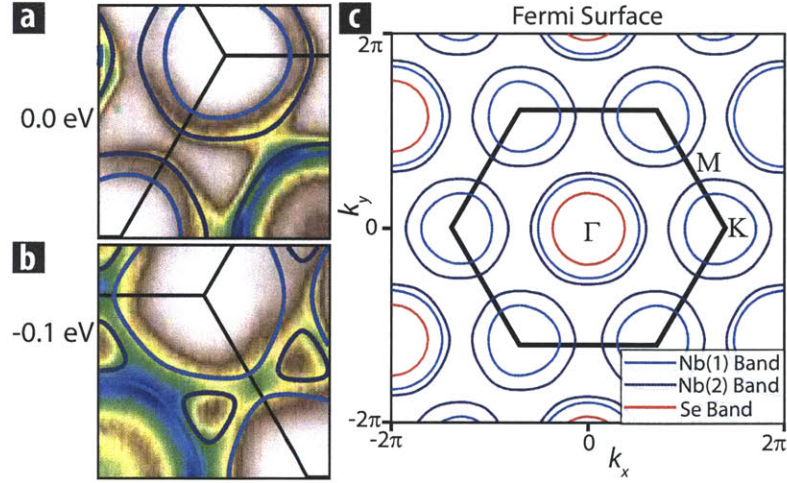
Figure 8-3: The Fermi Surface of NbSe$_2$. (a-b) ARPES measurements of constant energy contours (CECs) at the Fermi energy, ε_F (a), and -0.1 eV (b), with the corresponding CECs generated using tight-binding fit (Fig. 8-2a) overlaid to show the quality of the fit. **(b)** The Fermi surface obtained using the band structure fit in Fig. 8-2b, with the BZ shown in black.

8.3 Fermi Surface Nesting and the CDW Transition in NbSe$_2$
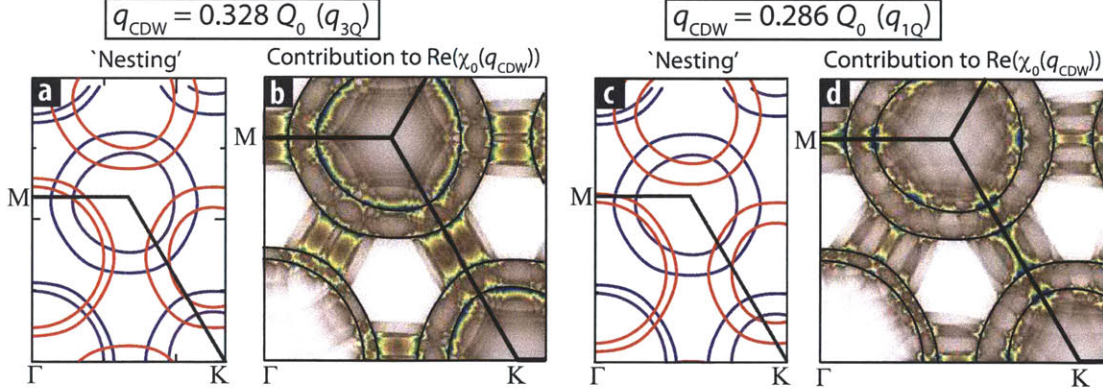
Figure 8-4: Inconsistencies in the Nesting-Driven CDW Picture of NbSe$_2$. (a, c) Visualizing potential FS nesting at the (a) $3Q$ and (c) $1Q$ wavevectors by translating the FS (Fig. 8-3c) by (a) $\vec{q}_{3Q}$ (a) and $\vec{q}_{1Q}$ (c) respectively (red) and superimposing onto the original FS (blue). **(b, d)** Another equivalent visualization of FS nesting, showing the momentum-resolved contributions to the noninteracting susceptibility, $\chi_0(\vec{q}_{CDW}, \omega = 0)$, for (b) $\vec{q}_{CDW} = \vec{q}_{3Q}$ and (d) $\vec{q}_{CDW} = \vec{q}_{1Q}$ respectively. The comparisons between (a,b) and (c,d) show that the FS nesting picture for CDWs at $\vec{q}_{3Q}$ and $\vec{q}_{1Q}$ are inconsistent with each other.

As a step towards understanding the 13% difference between the magnitudes of the observed $1Q$ and $3Q$ wavevectors, we examine their momentum space origin in the conventional nesting picture of density waves in Fig. 8-4. We note that the upper limit of the lateral strain in the $1Q$ regions was found to be 0.06% (§ 7.4.2), and therefore, to first order, the FS would be unchanged while considering wavevector differences of 13%.

The nesting conditions for the two CDWs can be examined by comparing Fermi surfaces displaced by the CDW wavevectors with the original FS. In such a picture, large regions of contact between the displaced FSs would correspond to classical FS nesting. We find that while the $3Q$ CDW could correspond to self-nesting within the inner K-barrel (Fig. 8-4a), as has been suggested previously[170], the $1Q$ CDW cannot be explained by this piece of the FS. The $1Q$ CDW could instead correspond to the nesting between the inner Γ-barrel and the K-barrel (Fig. 8-4c). Importantly, both cases highlight the absence of large parallel regions of the FS nested by the appropriate wavevectors.

More support for weak nesting at these wavevectors can be obtained by examining the k-space contributions to the non-interacting susceptibility, $\chi_0(\vec{q}, \omega = 0)$, at the two CDW wavevectors. In a traditional picture of a nesting driven CDW, the contributions to $\chi_0(\vec{q})$ at $\vec{q} = \vec{q}_{CDW}$ would be dominated by the nested FS regions. In contrast, we find that for both the $3Q$ and $1Q$ wavevectors, the susceptibility has contributions not only from the nested regions (as identified by Fig. 8-4a, c respectively), but equal, and sometimes even larger contributions from other k-space regions (Fig. 8-4b, d). These contributions likely arise from energies far from ε_F, and are further indicative of the absence of strong FS nesting in proximity to the CDW wavevectors.
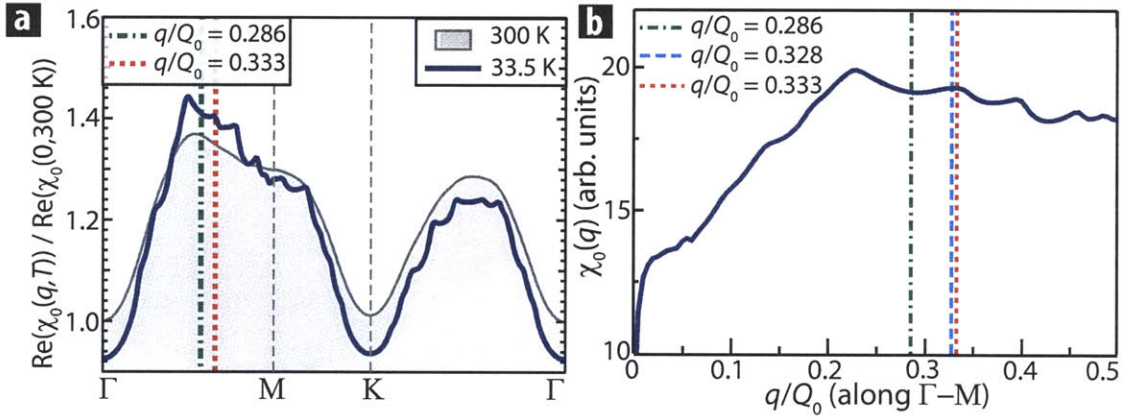
Figure 8-5: Noninteracting Susceptibility of NbSe$_2$. (a) The non-interacting susceptibility $\chi_0(q, \omega = 0)$ (blue, normalized to its value at 300 K, $q = 0$), calculated from the tight-binding fit to the NbSe$_2$ band structure (Fig. 8-2a) along the high symmetry directions in reciprocal space, compared to its value at 300 K (grey). **(b)** The noninteracting susceptibility, $\chi_0(q, \omega = 0)$ along the $\Gamma - M$ over the region of interest for the CDW transition, displaying a broad maximum over a range of wavevectors: $\tilde{q} \sim 0.25 - 0.4$[149, 157, 165]. The CDW wavevectors q_{1Q}, q_{3Q} and $Q_0/3$ are overlaid for comparison.

The stark contrast between our observations of two CDW wavevectors $\vec{q}_{1Q}$ and $\vec{q}_{3Q}$ of same orientation but 13% difference in magnitude, and the recent X-ray measurements reported by Feng *et al.*[162], provides strong evidence against FS nesting at one particular wavevector as a driving force for either CDW. While our 13% wavevector difference arose from moderate anisotropic strain (up to 0.06% in-plane), Feng *et al.* applied hydrostatic pressure sufficient to induce in-plane lattice distortions up to 1.6%, yet observed no measurable deviation of the CDW wavevector from $\vec{q}_{3Q}$[162]. The observed insensitivity of q_{3Q} to hydrostatic pressure would clearly indicate that the

FS does not qualitatively change in the presence of even relatively large lattice distortions, and would thus rule out a change in the FS as the source of our observed 13% wavevector difference.

Furthermore, consistent with our experiment and with previous calculations[149, 157, 165], we find no sharp peak in the susceptibility (Fig. 8-5b) computed from our modeled band structure. Therefore, our observations and calculations both indicate that the FS can play only a minor role in determining CDW wavevectors in NbSe₂. This highlights the key role that the q-dependence of alternative mechanisms such as electron-phonon coupling may play in driving the transition, and particularly the manner in which these mechanisms may be influenced by local strain.

8.4 Spectroscopy of the $1Q - 3Q$ Interface
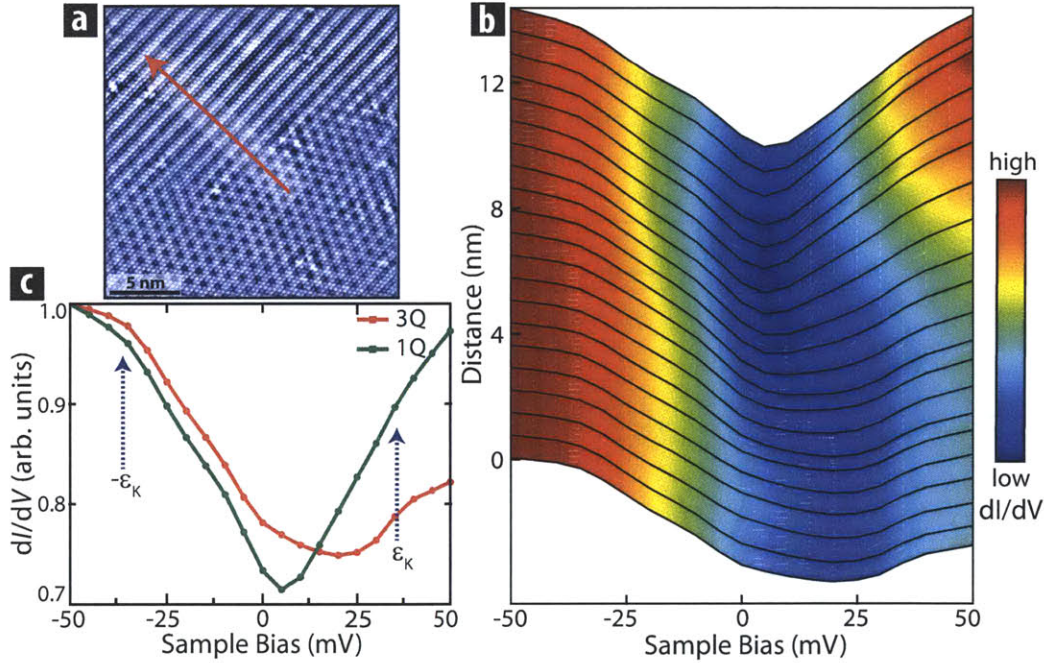
Figure 8-6: Spectroscopy Across the $1Q - 3Q$ Interface. (a-b) Linecut of dI/dV spectra across the $1Q - 3Q$ interface (b) taken along the red arrow in (a). **(c)** Representative spectra in the $3Q$ (red) and $1Q$ (green) regions of (a) overlaid for comparison. The $1Q$ spectra have a minimum close to ε_F, a deep V-shape with reduced asymmetry, and kinks at $\pm\varepsilon_K$. The spectra are normalized at -50 mV. Setpoint parameters: $V_0 = -50$ mV; $R_J = 0.2$ GΩ; $V_{mod} = 3.5$ mV.

Recall that the notable features in the typical spectra recorded over $3Q$ regions are (a) kinks at $\sim \pm35$ mV ($\pm\varepsilon_K$); (b) the spectral minimum centered above ε_F, at $\sim +16$ mV; and (c) marked asymmetry in the spectrum about ε_F. Spectroscopy across the $1Q - 3Q$ interface (Fig. 8-6) shows a marked difference between the tunneling signatures of the two CDW regions. Firstly, we note the continued presence of the ±35 mV kinks in the $1Q$ region, albeit with slightly reduced prominence. Second, we find that the spectral minimum shifts to close to ε_F in the $1Q$ regions. Also, the asymmetry of the spectra is significantly reduced in the $1Q$ regions, with increased conductance

in the empty states. The $1Q$ spectra are more V-shaped. A direct comparison of typical $1Q$ and $3Q$ spectra (Fig. 8-6c) indicates that the 'gap' feature is much deeper in the $1Q$ region. Finally, the spectra evolve smoothly between the two regions, and no abrupt changes in the spectral features are observed.

8.5   A Particle-Hole Asymmetric Spectral CDW Gap
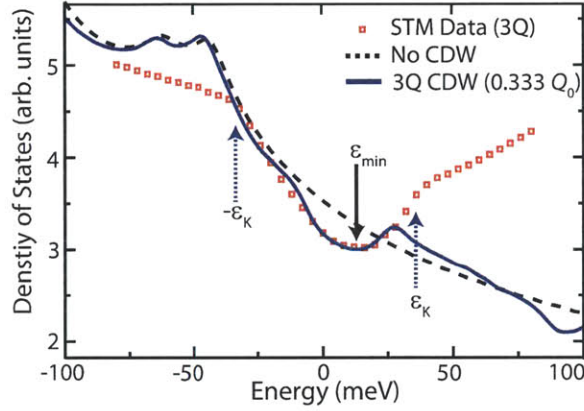
Figure 8-7: Particle-Hole Asymmetric CDW Gap in NbSe$_2$. Calculated DOS for NbSe$_2$ in the 'normal' state (black) and in the presence of a $3Q$ CDW (blue) using $\tilde{q} = 0.333\,Q_0$, $\tilde{\Delta} = 12\,\text{mV}$, $\tilde{\Gamma} = 5\,\text{mV}$, compared with the $3Q$ STM spectrum (red). The calculations reproduce the observed asymmetry, offset ε_{min}, and shape of the gap structure.

To calculate the DOS in the presence of a $3Q$ CDW, we impose a coupling between states connected by any one of the three $\tilde{\vec{q}}$-vectors, given by:

$$\mathcal{H}_{\text{CDW}} = \tilde{\Delta} \cdot \sum_{\vec{k}} \left(c^{\dagger}_{\vec{k}+\tilde{\vec{q}}} c_{\vec{k}} + \text{h.c.} \right) \tag{8.3}$$

The strength $\tilde{\Delta}$ of the coupling is taken as a free parameter in the reproduction of the experimentally observed DOS, with a broadening parameter fixed at $\Gamma = 5$ meV. Adjusting the size of $\tilde{q}$ slightly around the observed value of $q_{3Q} = 0.328\,Q_0$, we find the best match with STM dI/dV spectra using $\tilde{q} = (0.333 \pm 0.004)\,Q_0$ (corresponding to the locally commensurate CDW periodicity), $\tilde{\Delta} = (12 \pm 2)$ meV (which has not been previously apparent from direct observations by spectroscopic techniques), and $\tilde{\Gamma} = 5$ meV. With these parameter values, the gap structure in the calculated DOS closely approaches the overall shape, width and center of the gap structure seen in the measured data within ± 30 meV of the Fermi energy ε_F, as shown in Fig. 8-7.

In particular, we note the strong particle-hole asymmetry of the gap, with the gap center, ε_{min}, being well above ε_F. Furthermore, the absence of nesting over large parallel regions of the FS means that the apparent size of the full gap (~ 40 mV) is much larger than $2\tilde{\Delta}$. The fact that ε_{min} is offset from ε_F should be unsurprising for a quasi-2D system[197], but had not been understood

or observed in NbSe₂ until now, due to limitations of spectroscopic techniques which are sensitive to filled states only[170].
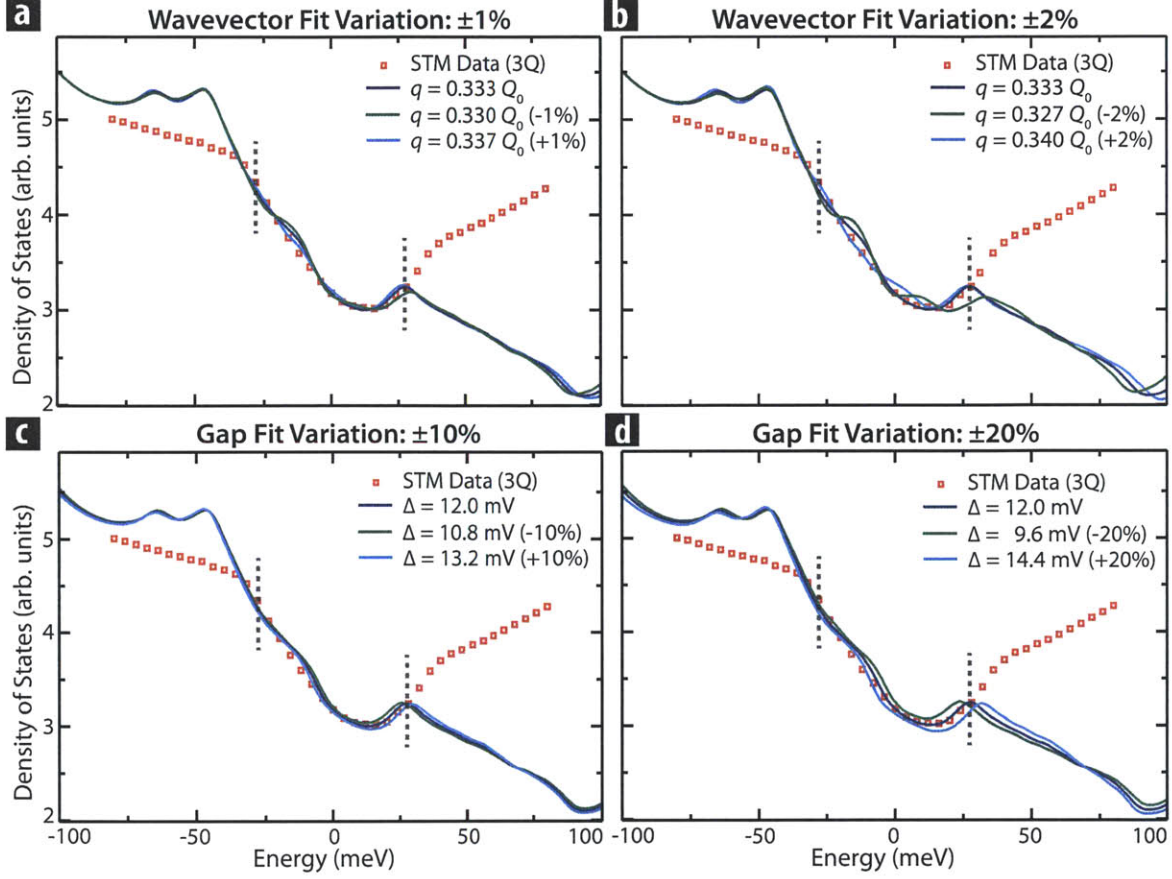
Figure 8-8: Fit Parameter Variation for Spectral CDW Gap. Calculated DOS spectrum using the band structure fit in the presence of a $3Q$ CDW, showing the effects of varying the fit parameters, wavevector $\tilde{q}$ and gap value $\tilde{\Delta}$ around the best fit values ($\tilde{q} = 0.333\,Q_0$, $\tilde{\Delta} = 12\,\text{meV}$, dark blue), compared with the STM data (red). **(a, b)** show the effects of varying the wavevector $\tilde{q}$ around $0.333\,Q_0$ by $\pm 1\%$ and $\pm 2\%$ respectively. **(c, d)** show the effects of varying the gap value $\tilde{\Delta}$ around 12 meV by $\pm 10\%$ and $\pm 20\%$ respectively. Error bars for $\tilde{q}$ ($0.004\,Q_0$) and $\tilde{\Delta}$ (2 meV) are deduced using these variations.

To demonstrate the accuracy of this fit, we show the effects of varying the wavevector $\tilde{q}$ by $1 - 2\%$ (Fig. 8-8a-b), and the gap value $\tilde{\Delta}$ by $10 - 20\%$ (Fig. 8-8c-d). Using these fit parameter variations, we estimate the errors for $\tilde{q}$ and $\tilde{\Delta}$ to be $0.004\,Q_0$ and 2 meV respectively. The value of $\tilde{\Delta}$ may however be an overestimate, leading to a systematic error of the same order as the fit uncertainty, since the described procedure does not take into account the particle-hole symmetric inelastic background in the experimental DOS. Accurate modeling of the inelastic background would require detailed temperature dependent spectroscopic data, which is beyond the scope of this work.

Crucially, we note that the particle-hole asymmetry in the CDW gap, with its minimum cen-

tered above ε_F, cannot be removed by the subtraction of a particle-hole symmetric background. Likewise, the striking deviation of our fitted gap parameter ($\tilde{\Delta} = 12$ meV) from previous results (four times larger than the 3 meV value detailed by Borisenko *et al.*[170], and three times smaller than the 35 meV value detailed by Hess *et al.*[45]) far exceeds fit or systematic uncertainties.

8.6 Red Herrings Surrounding the CDW Gap

We disentangle the CDW gap from the red herrings in the $3Q$ spectra through a comparison with the $1Q$ spectra in Fig. 8-6c, and through spectroscopy above T_{CDW} shown in Fig. 8-9.

The observed upturn above +35 mV and the kinks at ±35 mV are present in both the $1Q$ and $3Q$ spectra, but are absent in the DOS calculations. Moreover, these V-shaped $1Q$ spectra resemble the linear tunneling conductance background historically attributed to the inelastic coupling of tunneling electrons to a flat bosonic spectrum[198]. That this background is much stronger in the $1Q$ region, obscuring band structure effects, is likely a strain-induced phenomenon, which may be related to the buckling and associated decoupling of the topmost layers in the $1Q$ region. Meanwhile, present in both $1Q$ and $3Q$ spectra (thus unlikely to be associated with these different CDWs), yet absent in calculations (thus unlikely to be a band structure effect), are the ±35 mV kinks, previously and mistakenly identified as the CDW gap[45], which we examine in detail through temperature dependent spectroscopy.

8.6.1 Spectroscopic Studies above T_{CDW}
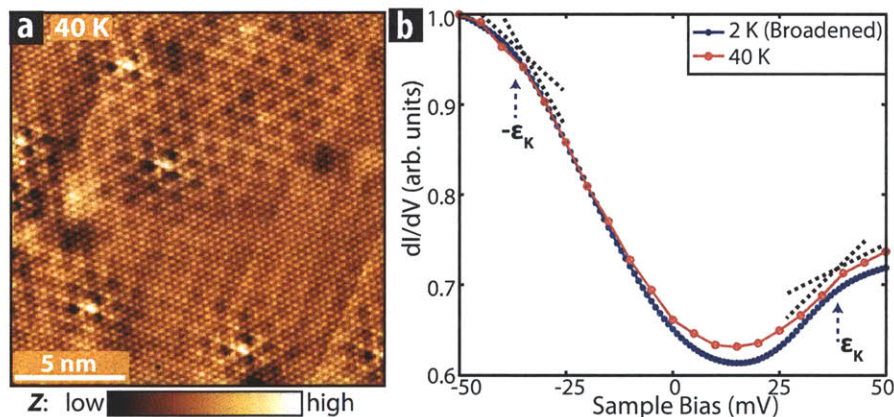
Figure 8-9: Spectroscopy above T_{CDW}. (a) An STM topograph acquired at 40 K, well above T_{CDW}, showing patches of CDW pinned to defects and impurities. **(b)** Spectrum acquired at 40 K (red) compared with that acquired at 2 K, 6 T (blue) on the same cleaved surface (within 300 nm). The 2 K spectrum has been thermally broadened to 40 K for ease of comparison. The spectral kinks at ±35 mV (±ε_K) are distinguishable well above T_{CDW}, as shown by the guides to the eye.

To experimentally verify the lack of bearing of the 35 mV kinks on the CDW phase, we performed spectroscopic measurements up to 45 K. We note the presence of the CDW in small regions

of the sample, visibly pinned to defects on the surface. We universally observe the presence of the 35 mV kinks in the STM spectra well above T_{CDW} (~ 33 K) in all sample regions. A comparison of the typical spectrum acquired at $40\,$K to that acquired at $2\,$K, is shown in Fig. 8-9b. We note that the data acquired at $40\,$K are thermally smeared by $\mathcal{O}(3k_B T)$, i.e. ~ 10 mV, resulting in a broadening of the kinks. Despite this, the kinks remain distinguishable, and are present throughout all spatial regions studied in this work. The universal presence of these ± 35 mV kinks even well above T_{CDW}, further demonstrates their lack of bearing on the CDW phase.

ARPES studies observe a prominent band structure kink at a similar energy in the Se Γ-pocket[165, 199], attributed to coupling to an optical phonon[171]. We therefore conclude that this self-energy effect is responsible for the ε_K kinks in the tunneling spectra as well. The discrepancy between the data and band structure calculations above $\sim 30\,$mV in Fig. 8-7 can thus be attributed to the inelastic tunneling background and self-energy effects.

8.6.2 Density of States Calculations for the $1Q$ Spectra
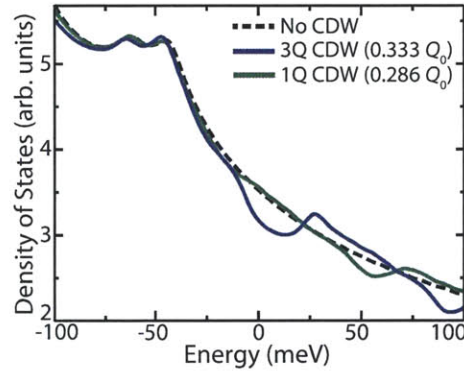
Figure 8-10: DOS Calculation for the $1Q$ CDW. Calculated DOS spectrum using the ARPES tight-binding fit - in the presence of a 3Q CDW ($\tilde{q} = 0.333\,Q_0$, blue) and a 1Q CDW ($q_{1Q} = 0.286\,Q_0$, green), with $\tilde{\Delta} = 12\,$meV.

For completeness, we show in Fig. 8-10 the calculated DOS in the presence of a $1Q$ CDW at the experimentally observed wavevector, $q_{1Q} = 0.286\,Q_0$, using $\tilde{\Delta} = 12$ meV. The lack of correspondence between this calculation (green curve in Fig. 8-10) and the measured dI/dV spectrum (green curve in Fig. 8-6c) can be attributed to the increased intensity of the inelastic background in the buckled region of the $1Q$ ribbons. This background is evident in the V-shape of the dI/dV spectrum in Fig. 8-6c, centered close to ε_F, as explained theoretically[198] and observed experimentally across a wide variety of materials[50, 198, 200–205].

8.6.3 Comparison of Band Structure Fits to ARPES Data and LDA Calculations

We also compare our results to a calculation of the DOS based on a tight-binding fit to the full three-dimensional LDA band structure reported by Johannes *et al.*[149]. The DOS obtained using
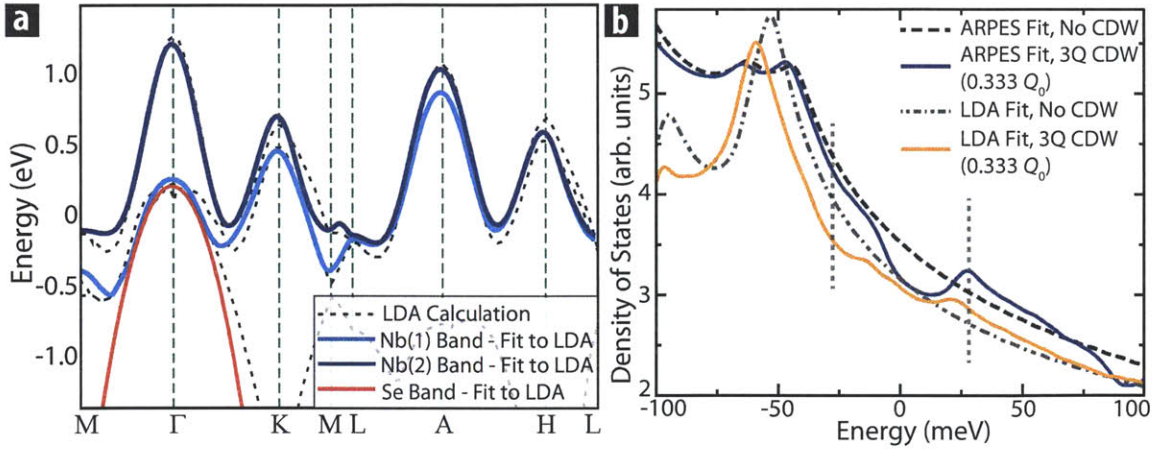
Figure 8-11: Comparison of Tight Binding Fits to ARPES Data and LDA Calculations. (a) The calculated band structure of NbSe$_2$ along high-symmetry directions, showing the two Nb-4d bands obtained from a Slater-Koster tight-binding fit to the LDA calculations of Johannes *et al.*[149], and the Se-4p band, modeled as a parabolic fit to LDA calculations of Johannes *et al.*[149], compared with the LDA calculations (dashed black lines). (b) Calculated DOS spectrum using the tight-binding fit to ARPES data (Fig. 8-2a, [165]) compared with the spectrum obtained using a tight-binding fit to LDA calculations of Johannes *et al.*[149], shown in (a), in the 'normal' state and in the presence of a 3Q CDW ($\tilde{q} = 0.333\,Q_0$, $\tilde{\Delta} = 12\,\mathrm{meV}$). The DOS spectrum calculated using the fit to the ARPES data better reproduces the gap feature observed in the STM dI/dV spectrum in Fig. 8-7.

this 3D LDA fit is compared to the results based on the 2D fit in Fig. 8-11b. We find that the STM data are best reproduced using the band structure observed by ARPES, and that there is a noticeable difference between the depths of the gaps in the two-dimensional ARPES based and three-dimensional LDA-based band structure fits (despite independent parameter optimization), which is indicative of some difference between the surface and bulk dispersions[149].

8.7 Perspectives on CDW Order in NbSe$_2$

We therefore resolve a longstanding debate about the anomalous CDW gap magnitude reported by STM measurements[45], and caution that not all ε_F-symmetric kinks in tunneling spectra are associated with order (e.g. density wave or superconducting gaps). On the contrary, we emphasize that the true CDW signature in NbSe$_2$ is offset from ε_F, which has confused an active research community for two decades, and has been disentangled now only by a combination of spatially resolved filled and empty state spectroscopy of a proximate (1Q) phase, and band structure calculations[197]. This emphasizes the need for full experimental exploration of proximate phases in other pertinent materials, combined with quantitative modeling. We further suggest that controlled local strain, through epitaxy or intentional defects, may be a useful tuning parameter to access the necessary proximate phases for comparison.

Our discovery provides a new perspective on the role of density wave order in complex systems. First, our resolution of two longstanding debates about NbSe$_2$ puts this much-studied mate-

rial on firmer footing as a well-understood model system for CDW studies and competing ground states in superconductors. We have disentangled the true CDW gap, and clarified that FS nesting plays a minor role in determining the CDW wavevectors in this material, thereby highlighting the role of other mechanisms in driving the transition. Second, our revelation of a particle-hole asymmetric CDW gap emphasizes the limitations of filled-state-only probes, e.g. ARPES, for investigating phases other than superconductivity - which is unambiguously particle-hole symmetric. Full spectral probes such as STM, in combination with quantitative calculations, are necessary to understand the competition between superconductivity and particle-hole asymmetric phases.

Chapter 9

Concluding Remarks

The exploration of the diverse electronic properties and ordered states emerging from the discovery of several classes of two dimensional electron materials over the past decade necessitates the development of a complement to traditional band structure probes. The nanoscale spatial resolution, temperature limited energy resolution, access to dilution fridge temperatures and magnetic fields, ability to measure empty states, and simultaneous access to various tuning parameters for 2D materials including gate tuning of the carrier density and strain – result in the spectroscopic STM being a promising candidate in this regard. However, a large discrepancy between the dispersions measured using Landau quantization and quasiparticle interference (QPI) – the two phenomena that equip STM with momentum resolution – have proved to be a major limitation.

In the first part of this thesis, we reported on the simultaneous observation and quantitative reconciliation of Landau quantization and QPI over a 300 meV energy range on the topological surface of Sb. We therefore introduced momentum-resolved scanning tunneling microscopy (MR-STM) – the combined measurement of LLs and QPI – as a reliable band structure probe, and demonstrated its nanoscale sensitivity to band structure deformations as well as chemical potential shifts, and its ability to measure the band structure of empty states. Armed with the technique of MR-STM, we addressed several important questions pertaining to the robustness of surface states in topological materials.

In the second part of the thesis, we demonstrated the indispensable utility of nanoscale spatial resolution and empty state sensitivity offered by spectroscopic STM. We reported on the imaging of a quantum interface between two charge density waves of triangular ($3Q$) and stripe ($1Q$) nature on the surface of the stoichiometric superconductor $2H$-NbSe$_2$. Our observation of distinct $1Q$ and $3Q$ CDW wavelengths rules out strong nesting in NbSe$_2$ and implies that factors such as electron-phonon coupling play the lead role in driving the CDW transition. Furthermore, by comparing the $1Q$ and $3Q$ spectra, we have for the first time disentangled the particle-hole asymmetric CDW gap, centered above the Fermi energy, from spectroscopic red herrings.

In conclusion, our work puts spectroscopic STM on a sound platform as a nanoscale probe of electronic band structure and ordered phases, with several promising applications towards the study of 2D materials.

Bibliography

[1] N. W. Ashcroft and N. D. Mermin. *Solid State Physics*. Academic Press, 1st edition, January 1979. ISBN 0030839939.

[2] Piers Coleman. *Introduction to Many Body Physics*. Cambridge University Press, May 2001. ISBN 0521864887.

[3] A. H. Castro Neto, F. Guinea, N. M. R. Peres, K. S. Novoselov, and A. K. Geim. The electronic properties of graphene. *Reviews of Modern Physics*, 81(1):109–162, January 2009. doi:10.1103/RevModPhys.81.109.

[4] Timothy H. Hsieh, Hsin Lin, Junwei Liu, Wenhui Duan, Arun Bansi, and Liang Fu. Topological crystalline insulators in the SnTe material class. *Nature Communications*, 3:982, July 2012. doi:10.1038/ncomms1969.

[5] Roland Winkler. *Spin-orbit Coupling Effects in Two-Dimensional Electron and Hole Systems*. Springer, December 2003. ISBN 3540011870.

[6] Choongyu Hwang, David A. Siegel, Sung-Kwan Mo, William Regan, Ariel Ismach, Yuegang Zhang, Alex Zettl, and Alessandra Lanzara. Fermi velocity engineering in graphene by substrate modification. *Scientific Reports*, 2:590, August 2012. doi:10.1038/srep00590.

[7] J. T. Ye, Y. J. Zhang, R. Akashi, M. S. Bahramy, R. Arita, and Y. Iwasa. Superconducting Dome in a Gate-Tuned Band Insulator. *Science*, 338(6111):1193–1196, November 2012. doi:10.1126/science.1228006.

[8] Simon M. Sze and Kwok K. Ng. *Physics of Semiconductor Devices*. Wiley-Interscience, 3rd edition, October 2006. ISBN 0471143235.

[9] C. H. Ahn, M. Di Ventra, J. N. Eckstein, C. Daniel Frisbie, M. E. Gershenson, A. M. Goldman, I. H. Inoue, J. Mannhart, Andrew J. Millis, Alberto F. Morpurgo, Douglas Natelson, and Jean-Marc Triscone. Electrostatic modification of novel materials. *Reviews of Modern Physics*, 78(4):1185–1212, November 2006. doi:10.1103/RevModPhys.78.1185.

[10] K. S. Novoselov, A. K. Geim, S. V. Morozov, D. Jiang, Y. Zhang, S. V. Dubonos, I. V. Grigorieva, and A. A. Firsov. Electric field effect in atomically thin carbon films. *Science*, 306(5696):666–9, October 2004. doi:10.1126/science.1102896.

[11] Hadar Steinberg, Dillon R. Gardner, Young S. Lee, and Pablo Jarillo-Herrero. Surface State Transport and Ambipolar Electric Field Effect in Bi_2Se_3 Nanodevices. *Nano Letters*, 10:5032–5036, November 2010. doi:10.1021/nl1032183.

[12] Dohun Kim, Sungjae Cho, Nicholas P. Butch, Paul Syers, Kevin Kirshenbaum, Shaffique Adam, John-pierre Paglione, and Michael S. Fuhrer. Surface conduction of topological Dirac electrons in bulk insulating Bi_2Se_3. *Nature Physics*, (8):459–463, April 2012. doi:10.1038/nphys2286.

[13] D. Daghero, F. Paolucci, A. Sola, M. Tortello, G. A. Ummarino, M. Agosto, R. S. Gonnelli, Ji-jeesh R. Nair, and C. Gerbaldi. Large Conductance Modulation of Gold Thin Films by Huge Charge Injection via Electrochemical Gating. *Physical Review Letters*, 108(6):066807, February 2012. doi:10.1103/PhysRevLett.108.066807.

[14] Yoshinori Okada, Wenwen Zhou, D. Walkup, Chetan Dhital, Stephen D. Wilson, and V. Madhavan. Ripple-modulated electronic structure of a 3D topological insulator. *Nature Communications*, 3:1158, October 2012. doi:10.1038/ncomms2150.

[15] N. Levy, S. A. Burke, K. L. Meaker, M. Panlasigui, A. Zettl, F. Guinea, A. H. C. Neto, and M. F. Crommie. Strain-Induced Pseudo-Magnetic Fields Greater Than 300 Tesla in Graphene Nanobubbles. *Science*, 329(5991):544, July 2010. doi:10.1126/science.1191700.

[16] Vitor M. Pereira and A. H. Castro Neto. Strain Engineering of Graphene's Electronic Structure. *Physical Review Letters*, 103(4):046801, July 2009. doi:10.1103/PhysRevLett.103.046801.

[17] David A. Siegel, Choongyu Hwang, Alexei V. Fedorov, and Alessandra Lanzara. Electron-phonon coupling and intrinsic bandgap in highly-screened graphene. *New Journal of Physics*, 14(9):095006, September 2012. doi:10.1088/1367-2630/14/9/095006.

[18] Anjan Soumyanarayanan, Michael M. Yee, Yang He, Jasper van Wezel, Dirk J. Rahn, Kai Rossnagel, E. W. Hudson, Michael R. Norman, and Jennifer E. Hoffman. Quantum phase transition from triangular to stripe charge order in $NbSe_2$. *Proceedings of the National Academy of Sciences*, 110(5):1623–1627, January 2013. doi:10.1073/pnas.1211387110.

[19] Niv Levy, Tong Zhang, Jeonghoon Ha, Fred Sharifi, A. Alec Talin, Young Kuk, and Joseph A. Stroscio. Experimental Evidence for s-Wave Pairing Symmetry in Superconducting $Cu_xBi_2Se_3$ Single Crystals Using a Scanning Tunneling Microscope. *Physical Review Letters*, 110(11):117001, March 2013. doi:10.1103/PhysRevLett.110.117001.

[20] Julie A. Bert, Beena Kalisky, Christopher Bell, Minu Kim, Yasuyuki Hikita, Harold Y. Hwang, and Kathryn A. Moler. Direct imaging of the coexistence of ferromagnetism and superconductivity at the $LaAlO_3/SrTiO_3$ interface. *Nature Physics*, 7(10):767–771, September 2011. doi:10.1038/nphys2079.

[21] Yuanbo Zhang, Victor W. Brar, Caglar O. Girit, Alex Zettl, and Michael F. Crommie. Origin of spatial charge inhomogeneity in graphene. *Nature Physics*, 5(10):722–726, August 2009. doi:10.1038/nphys1365.

[22] Jungseok Chae, Suyong Jung, Andrea F. Young, Cory R. Dean, Lei Wang, Yuanda Gao, Kenji Watanabe, Takashi Taniguchi, James Hone, Kenneth L. Shepard, Phillip Kim, Nikolai B. Zhitenev, and Joseph A. Stroscio. Renormalization of the Graphene Dispersion Velocity Determined

from Scanning Tunneling Spectroscopy. *Physical Review Letters*, 109(11):116802, September 2012. doi:10.1103/PhysRevLett.109.116802.

[23] Haim Beidenkopf, Pedram Roushan, Jungpil Seo, Lindsay Gorman, Ilya Drozdov, Yew San Hor, R. J. Cava, and Ali Yazdani. Spatial fluctuations of helical Dirac fermions on the surface of topological insulators. *Nature Physics*, 7(12):939–943, October 2011. doi:10.1038/nphys2108.

[24] Y. S. Hor, A. J. Williams, J. G. Checkelsky, Pedram Roushan, Jungpil Seo, Q. Xu, H. W. Zandbergen, Ali Yazdani, N. P. Ong, and R. J. Cava. Superconductivity in $Cu_xBi_2Se_3$ and its Implications for Pairing in the Undoped Topological Insulator. *Physical Review Letters*, 104(5):057001, February 2010. doi:10.1103/PhysRevLett.104.057001.

[25] D. Shoenberg. *Magnetic Oscillations in Metals (Cambridge Monographs on Physics)*. Cambridge University Press, 1st edition, 1984. ISBN 0521118786.

[26] Donghui Lu, Inna M. Vishik, Ming Yi, Yulin Chen, Rob G. Moore, and Zhi-Xun Shen. Angle-Resolved Photoemission Studies of Quantum Materials. *Annual Review of Condensed Matter Physics*, 3(1):129–167, March 2012. doi:10.1146/annurev-conmatphys-020911-125027.

[27] Andrea Damascelli, Zahid Hussain, and Zhi-Xun Shen. Angle-resolved photoemission studies of the cuprate superconductors. *Reviews of Modern Physics*, 75(2):473–541, April 2003. doi:10.1103/RevModPhys.75.473.

[28] J. Bardeen. Tunnelling from a Many-Particle Point of View. *Physical Review Letters*, 6(2):57–59, January 1961. doi:10.1103/PhysRevLett.6.57.

[29] J. J. Sakurai. *Modern Quantum Mechanics*. Addison Wesley, September 1993. ISBN 0201539292.

[30] R. Shankar. *Principles of Quantum Mechanics*. Springer, 2nd edition, September 1994. ISBN 0306447908.

[31] Gerd Binnig and Heinrich Rohrer. Scanning tunneling microscopy - from birth to adolescence. *Reviews of Modern Physics*, 59(3):615–625, July 1987. doi:10.1103/RevModPhys.59.615.

[32] S.-H. Pan, E. W. Hudson, and J. C. Davis. 3He refrigerator based very low temperature scanning tunneling microscope. *Review of Scientific Instruments*, 70(2):1459, 1999. doi:10.1063/1.1149605.

[33] J. Bardeen, L. N. Cooper, and J. R. Schrieffer. Theory of Superconductivity. *Physical Review*, 108(5):1175–1204, December 1957. doi:10.1103/PhysRev.108.1175.

[34] C. Julian Chen. *Introduction to Scanning Tunneling Microscopy (Monographs on the Physics and Chemistry of Materials)*. Oxford University Press, 2nd edition, December 2007. ISBN 0199211507.

[35] M. C. Boyer, W. D. Wise, Kamalesh Chatterjee, M. Yi, Takeshi Kondo, T. Takeuchi, H. Ikuta, and E. W. Hudson. Imaging the two gaps of the high-temperature superconductor $Bi_2Sr_2CuO_{6+x}$. *Nature Physics*, 3(11):802–806, November 2007. doi:10.1038/nphys725.

[36] Curry B. Taylor. *Coexistence of Bogoliubov Quasiparticles and Electronic Cluster Domains in Lightly Hole-Doped Cuprate Superconductors*. Phd, Cornell University, 2008.

[37] Y. Kohsaka, C. Taylor, K. Fujita, A. R. Schmidt, C. Lupien, T. Hanaguri, M. Azuma, M. Takano, H. Eisaki, H. Takagi, S. Uchida, and J. C. Davis. An intrinsic bond-centered electronic glass with unidirectional domains in underdoped cuprates. *Science*, 315(5817):1380–5, March 2007. doi:10.1126/science.1138584.

[38] K. M. Lang, V. Madhavan, J. E. Hoffman, E. W. Hudson, H. Eisaki, S. Uchida, and J. C. Davis. Imaging the granular structure of high-T_c superconductivity in underdoped $Bi_2Sr_2CaCu_2O_{8+\delta}$. *Nature*, 415 (6870):412–6, January 2002. doi:10.1038/415412a.

[39] Akira Sugimoto, Toshikazu Ekino, and Hiroshi Eisaki. Nanoscale Modulation of Local Barrier Height on Bi-based Cuprate Superconductors Observed by Scanning Tunneling Microscopy/Spectroscopy. *Journal of the Physical Society of Japan*, 77(4):043705, April 2008. doi:10.1143/jpsj.77.043705.

[40] Ø ystein Fischer, Martin Kugler, Ivan Maggio-Aprile, Christophe Berthod, and Christoph Renner. Scanning tunneling spectroscopy of high-temperature superconductors. *Reviews of Modern Physics*, 79(1):353–419, March 2007. doi:10.1103/RevModPhys.79.353.

[41] Ali Yazdani, B. A. Jones, C. P. Lutz, M. F. Crommie, and D. M. Eigler. Probing the local effects of magnetic impurities on superconductivity. *Science*, 275(5307):1767, March 1997. doi:10.1126/science.275.5307.1767.

[42] V. Madhavan, W. Chen, T. Jamneala, M. F. Crommie, and N. S. Wingreen. Tunneling into a single magnetic atom: spectroscopic evidence of the Kondo resonance. *Science*, 280(5363):567–9, April 1998. doi:10.1126/science.280.5363.567.

[43] E. W. Hudson, K. M. Lang, V. Madhavan, S.-H. Pan, H. Eisaki, S. Uchida, and J. C. Davis. Interplay of magnetism and high-T_c superconductivity at individual Ni impurity atoms in $Bi_2Sr_2CaCu_2O_{8+\delta}$. *Nature*, 411(6840):920–4, June 2001. doi:10.1038/35082019.

[44] H. F. Hess, R. Robinson, and J. Waszczak. Vortex-core structure observed with a scanning tunneling microscope. *Physical Review Letters*, 64(22):2711–2714, May 1990. doi:10.1103/PhysRevLett.64.2711.

[45] H. F. Hess, R. B. Robinson, and J. V. Waszczak. STM spectroscopy of vortex cores and the flux lattice. *Physica B: Condensed Matter*, 169(1-4):422, February 1991. doi:10.1016/0921-4526(91)90262-D.

[46] I. Maggio-Aprile, Ch. Renner, A. Erb, E. Walker, and Ø ystein Fischer. Direct Vortex Lattice Imaging and Tunneling Spectroscopy of Flux Lines on $YBa_2Cu_3O_{7-\delta}$. *Physical Review Letters*, 75(14):2754–2757, October 1995. doi:10.1103/PhysRevLett.75.2754.

[47] J. E. Hoffman, E. W. Hudson, K. M. Lang, V. Madhavan, H. Eisaki, S. Uchida, and J. C. Davis. A four unit cell periodic pattern of quasi-particle states surrounding vortex cores in $Bi_2Sr_2CaCu_2O_{8+\delta}$. *Science*, 295(5554):466–9, January 2002. doi:10.1126/science.1066974.

[48] Yi Yin, M. Zech, T. L. Williams, X. Wang, G. Wu, X.-H. Chen, and J. E. Hoffman. Scanning Tunneling Spectroscopy and Vortex Imaging in the Iron Pnictide Superconductor $BaFe_{1.8}Co_{0.2}As_2$. *Physical Review Letters*, 102(9):097002, March 2009. doi:10.1103/PhysRevLett.102.097002.

[49] J. M. Carpinelli, H. H. Weitering, E. W. Plummer, and R. Stumpf. Direct observation of a surface charge density wave. *Nature*, 381(6581):398–400, 1996. doi:10.1038/381398a0.

[50] K.C. Rahnejat, C.a. Howard, N.E. Shuttleworth, S.R. Schofield, K. Iwaya, C.F. Hirjibehedin, Ch. Renner, G. Aeppli, and M. Ellerby. Charge density waves in the graphene sheets of the superconductor CaC_6. *Nature Communications*, 2:558, November 2011. doi:10.1038/ncomms1574.

[51] T.-M. Chuang, Milan P. Allan, Jinho Lee, Yang Xie, Ni Ni, S. L. Bud'ko, G. S. Boebinger, P. C. Canfield, and J. C. Davis. Nematic electronic structure in the "parent" state of the iron-based superconductor $Ca(Fe_{1-x}Co_x)_2As_2$. *Science*, 327(5962):181–4, January 2010. doi:10.1126/science.1181083.

[52] Sangita Bose, Antonio M. García-García, Miguel M. Ugeda, Juan D. Urbina, Christian H. Michaelis, Iván Brihuega, and Klaus Kern. Observation of shell effects in superconducting nanoparticles of Sn. *Nature Materials*, 9(7):550–4, July 2010. doi:10.1038/nmat2768.

[53] Shengyong Qin, Jungdae Kim, Qian Niu, and Chih-Kang Shih. Superconductivity at the two-dimensional limit. *Science*, 324(5932):1314–7, June 2009. doi:10.1126/science.1170775.

[54] David J. Griffiths. *Introduction to Electrodynamics*. Addison Wesley, 3rd edition, 1980. ISBN 013805326X.

[55] John H. Davies. *The Physics of Low-Dimensional Semiconductors*. Cambridge University Press, December 1997. ISBN 052148491X.

[56] T. Hanaguri, S. Niitaka, K. Kuroki, and H. Takagi. Unconventional s-Wave Superconductivity in Fe(Se,Te). *Science*, 328(5977):474–476, April 2010. doi:10.1126/science.1187399.

[57] David L. Miller, Kevin D. Kubista, Gregory M. Rutter, Ming Ruan, Walt A. de Heer, Phillip N. First, and Joseph A. Stroscio. Observing the quantization of zero mass carriers in graphene. *Science*, 324 (5929):924–7, May 2009. doi:10.1126/science.1171810.

[58] Walter Kohn. Cyclotron Resonance and de Haas-van Alphen Oscillations of an Interacting Electron Gas. *Physical Review*, 123(4):1242–1244, August 1961. doi:10.1103/PhysRev.123.1242.

[59] J. W. G. Wildöer, C. J. P. M. Harmans, and H. van Kempen. Observation of Landau levels at the InAs(110) surface by scanning tunneling spectroscopy. *Physical Review B*, 55(24):R16013, June 1997. doi:10.1103/PhysRevB.55.R16013.

[60] M. Morgenstern, Chr. Wittneven, R Dombrowski, and R. Wiesendanger. Spatial Fluctuations of the Density of States in Magnetic Fields Observed with Scanning Tunneling Spectroscopy. *Physical Review Letters*, 84(24):5588–5591, June 2000. doi:10.1103/PhysRevLett.84.5588.

[61] Yoshinori Okada, Wenwen Zhou, Chetan Dhital, D. Walkup, Ying Ran, Z. Wang, Stephen D. Wilson, and V. Madhavan. Visualizing Landau Levels of Dirac Electrons in a One-Dimensional Potential. *Physical Review Letters*, 109(16):166407, October 2012. doi:10.1103/PhysRevLett.109.166407.

[62] Young Jae Song, Alexander F. Otte, Young Kuk, Yike Hu, David B. Torrance, Phillip N. First, Walt A. de Heer, Hongki Min, Shaffique Adam, Mark D. Stiles, Allan H. MacDonald, and Joseph A. Stroscio. High-resolution tunnelling spectroscopy of a graphene quartet. *Nature*, 467(7312):185–189, September 2010. doi:10.1038/nature09330.

[63] K. Hashimoto, C. Sohrmann, J. Wiebe, T. Inaoka, F. Meier, Y. Hirayama, R. Römer, R. Wiesendanger, and M. Morgenstern. Quantum Hall Transition in Real Space: From Localized to Extended States. *Physical Review Letters*, 101(25):256802, December 2008. doi:10.1103/PhysRevLett.101.256802.

[64] K. Hashimoto, T. Champel, S. Florens, C. Sohrmann, J. Wiebe, Y. Hirayama, R. A. Römer, R. Wiesendanger, and M. Morgenstern. Robust Nodal Structure of Landau Level Wave Functions Revealed by Fourier Transform Scanning Tunneling Spectroscopy. *Physical Review Letters*, 109(11):116805, September 2012. doi:10.1103/PhysRevLett.109.116805.

[65] M. F. Crommie, C. P. Lutz, and D. M. Eigler. Imaging standing waves in a two-dimensional electron gas. *Nature*, 363(6429):524–527, June 1993. doi:10.1038/363524a0.

[66] J. Friedel. Electronic structure of primary solid solutions in metals. *Advances in Physics*, 3(12):446–507, October 1954. doi:10.1080/00018735400101233.

[67] Jennifer E. Hoffman. *A Search for Alternative Electronic Order in the High Temperature Superconductor $Bi_2Sr_2CaCu_2O_{8+\delta}$ by Scanning Tunneling Microscopy*. Phd, University of California at Berkeley, 2003.

[68] Pedram Roushan, Jungpil Seo, C. V. Parker, Yew San Hor, David Hsieh, Dong Qian, Anthony Richardella, M. Zahid Hasan, R. J. Cava, and Ali Yazdani. Topological surface states protected from backscattering by chiral spin texture. *Nature*, 460(7259):1106–1109, 2009. doi:10.1038/nature08308.

[69] Tong Zhang, Peng Cheng, Xi Chen, Jin-Feng Jia, Xu-Cun Ma, Ke He, Li-Li Wang, Hai-Jun Zhang, Xi Dai, Zhong Fang, Xin-Cheng Xie, and Qi-Kun Xue. Experimental Demonstration of Topological Surface States Protected by Time-Reversal Symmetry. *Physical Review Letters*, 103(26):266803, December 2009. doi:10.1103/PhysRevLett.103.266803.

[70] Yoshinori Okada, Chetan Dhital, Wenwen Zhou, Erik D. Huemiller, Hsin Lin, S. Basak, A. Bansil, Y.-B. Huang, H. Ding, Z. Wang, Stephen D. Wilson, and V. Madhavan. Direct Observation of Broken Time-Reversal Symmetry on the Surface of a Magnetically Doped Topological Insulator. *Physical Review Letters*, 106(20):206805, May 2011. doi:10.1103/PhysRevLett.106.206805.

[71] G. M. Rutter, J. N. Crain, N. P. Guisinger, T. Li, Phillip N. First, and J. A. Stroscio. Scattering and interference in epitaxial graphene. *Science*, 317(5835):219–22, July 2007. doi:10.1126/science.1142882.

[72] J. E. Hoffman, K. McElroy, D.-H. Lee, K. M. Lang, H. Eisaki, S. Uchida, and J. C. Davis. Imaging quasiparticle interference in $Bi_2Sr_2CaCu_2O_{8+\delta}$. *Science*, 297(5584):1148–51, August 2002. doi:10.1126/science.1072640.

[73] K. McElroy, R. W. Simmonds, J. E. Hoffman, D.-H. Lee, J. Orenstein, H. Eisaki, S. Uchida, and J. C. Davis. Relating atomic-scale electronic phenomena to wave-like quasiparticle states in superconducting $Bi_2Sr_2CaCu_2O_{8+\delta}$. *Nature*, 422(6932):592–6, April 2003. doi:10.1038/nature01496.

[74] T. Hanaguri, Y. Kohsaka, M. Ono, M. Maltseva, P. Coleman, I. Yamada, M. Azuma, M. Takano, K. Ohishi, and H. Takagi. Coherence factors in a high-T_c cuprate probed by quasi-particle scattering off vortices. *Science*, 323(5916):923–6, March 2009. doi:10.1126/science.1166138.

[75] Jhinhwan Lee, K. Fujita, A. R. Schmidt, Chung Koo Kim, H. Eisaki, S. Uchida, and J. C. Davis. Spectroscopic fingerprint of phase-incoherent superconductivity in the cuprate pseudogap state. *Science*, 325(5944):1099–103, August 2009. doi:10.1126/science.1176369.

[76] Milan P. Allan, A. W. Rost, A. P. Mackenzie, Y. Xie, J. C. Davis, K. Kihou, C. H. Lee, A. Iyo, H. Eisaki, and T.-M. Chuang. Anisotropic Energy Gaps of Iron-Based Superconductivity from Intraband Quasiparticle Interference in LiFeAs. *Science*, 336(6081):563–567, May 2012. doi:10.1126/science.1218726.

[77] A. R. Schmidt, M. H. Hamidian, P. Wahl, F. Meier, A. V. Balatsky, J. D. Garrett, T. J. Williams, G. M. Luke, and J. C. Davis. Imaging the Fano lattice to 'hidden order' transition in URu_2Si_2. *Nature*, 465 (7298):570–576, June 2010. doi:10.1038/nature09073.

[78] Adina Luican, Guohong Li, and Eva Y. Andrei. Quantized Landau level spectrum and its density dependence in graphene. *Physical Review B*, 83(4):041405, January 2011. doi:10.1103/PhysRevB.83.041405.

[79] L. D. Landau and E. M. Lifshitz. *Statistical Physics, Part 1*. Butterworth-Heinemann, 3rd edition, 1980. ISBN 0750633727.

[80] Mehran Kardar. *Statistical Physics of Particles*. Cambridge University Press, 1st edition, 2007. ISBN 0521873428.

[81] L. D. Landau and E. M. Lifshitz. *Statistical Physics, Part 2*. Butterworth-Heinemann, 3rd edition, 1980. ISBN 0750626364.

[82] R. B. Laughlin. Quantized Hall conductivity in two dimensions. *Physical Review B*, 23(10):5632–5633, May 1981. doi:10.1103/PhysRevB.23.5632.

[83] J. E. Avron, Daniel Osadchy, and Ruedi Seiler. A topological look at the quantum Hall effect. *Physics Today*, 56(8):38–42, August 2003. doi:10.1063/1.1611351.

[84] B. Jeckelmann and B. Jeanneret. The quantum Hall effect as an electrical resistance standard. *Reports on Progress in Physics*, 64(12):1603–1655, 2001. ISSN 0034-4885. doi:10.1088/0034-4885/64/12/201.

[85] B. I. Halperin. Quantized Hall conductance, current-carrying edge states, and the existence of extended states in a two-dimensional disordered potential. *Physical Review B*, 25(4):2185–2190, February 1982. doi:10.1103/PhysRevB.25.2185.

[86] D. J. Thouless, M. Kohmoto, M. P. Nightingale, and M. den Nijs. Quantized Hall Conductance in a Two-Dimensional Periodic Potential. *Physical Review Letters*, 49(6):405–408, August 1982. doi:10.1103/PhysRevLett.49.405.

[87] M. Zahid Hasan and C. L. Kane. Colloquium: Topological insulators. *Reviews of Modern Physics*, 82 (4):3045–3067, November 2010. doi:10.1103/RevModPhys.82.3045.

[88] F. D. M. Haldane. Model for a Quantum Hall Effect without Landau Levels: Condensed-Matter Realization of the "Parity Anomaly". *Physical Review Letters*, 61(18):2015–2018, October 1988. doi:10.1103/PhysRevLett.61.2015.

[89] C. L. Kane and E.J. Mele. Quantum Spin Hall Effect in Graphene. *Physical Review Letters*, 95(22): 226801, November 2005. doi:10.1103/PhysRevLett.95.226801.

[90] C. L. Kane and E.J. Mele. Z_2 Topological Order and the Quantum Spin Hall Effect. *Physical Review Letters*, 95(14):146802, September 2005. doi:10.1103/PhysRevLett.95.146802.

[91] B. A. Bernevig, T. L. Hughes, and Shou-Cheng Zhang. Quantum spin Hall effect and topological phase transition in HgTe quantum wells. *Science*, 314(5806):1757, December 2006. doi:10.1126/science.1133734.

[92] Markus König, Steffen Wiedmann, Christoph Brüne, Andreas Roth, Hartmut Buhmann, L. W. Molenkamp, Xiao-Liang Qi, and Shou-Cheng Zhang. Quantum spin hall insulator state in HgTe quantum wells. *Science*, 318(5851):766, November 2007. doi:10.1126/science.1148047.

[93] Xiao-Liang Qi and Shou-Cheng Zhang. Topological insulators and superconductors. *Reviews of Modern Physics*, 83(4):1057–1110, October 2011. doi:10.1103/RevModPhys.83.1057.

[94] Andreas Roth, Christoph Brüne, Hartmut Buhmann, L. W. Molenkamp, Joseph Maciejko, Xiao-Liang Qi, and Shou-Cheng Zhang. Nonlocal Transport in the Quantum Spin Hall State. *Science*, 325(5938): 294, July 2009. doi:10.1126/science.1174736.

[95] Liang Fu, C. L. Kane, and E.J. Mele. Topological Insulators in Three Dimensions. *Physical Review Letters*, 98(10):106803–4, March 2007. doi:10.1103/PhysRevLett.98.106803.

[96] J. E. Moore and L. Balents. Topological invariants of time-reversal-invariant band structures. *Physical Review B*, 75(12):121306, March 2007. doi:10.1103/PhysRevB.75.121306.

[97] Rahul Roy. Topological phases and the quantum spin Hall effect in three dimensions. *Physical Review B*, 79(19):195322, May 2009. doi:10.1103/PhysRevB.79.195322.

[98] Liang Fu and C. L. Kane. Topological insulators with inversion symmetry. *Physical Review B*, 76(4): 045302, July 2007. doi:10.1103/PhysRevB.76.045302.

[99] David Hsieh, Y. Xia, L. A. Wray, Dong Qian, A. Pal, J. H. Dil, J. Osterwalder, F. Meier, G. Bihlmayer, C. L. Kane, Yew San Hor, R. J. Cava, and M. Zahid Hasan. Observation of unconventional quantum spin textures in topological insulators. *Science*, 323(5916):919–22, February 2009. doi:10.1126/science.1167733.

[100] D. Hsieh, Y. Xia, D. Qian, L. A. Wray, J. H. Dil, F. Meier, J. Osterwalder, L. Patthey, J. G. Checkelsky, N. P. Ong, A. V. Fedorov, Hsin Lin, A. Bansil, D. Grauer, Yew San Hor, R. J. Cava, and M. Zahid Hasan. A tunable topological insulator in the spin helical Dirac transport regime. *Nature*, 460(7259): 1101–5, August 2009. doi:10.1038/nature08234.

[101] David Hsieh, Dong Qian, L. A. Wray, Y. Xia, Yew San Hor, R. J. Cava, and M. Zahid Hasan. A topological Dirac insulator in a quantum spin Hall phase. *Nature*, 452(7190):970–4, April 2008. doi:10.1038/nature06843.

[102] Joel E. Moore. The birth of topological insulators. *Nature*, 464(7286):194–8, March 2010. doi:10.1038/nature08916.

[103] Liang Fu and C. L. Kane. Superconducting Proximity Effect and Majorana Fermions at the Surface of a Topological Insulator. *Physical Review Letters*, 100(9):96407, March 2008. doi:10.1103/PhysRevLett.100.096407.

[104] Y. Xia, D. Qian, D. Hsieh, L. A. Wray, A. Pal, Hsin Lin, A. Bansil, D. Grauer, Yew San Hor, R. J. Cava, and M. Zahid Hasan. Observation of a large-gap topological-insulator class with a single Dirac cone on the surface. *Nature Physics*, 5(6):398–402, May 2009. doi:10.1038/nphys1274.

[105] H. J. Zhang, Chao-Xing Liu, Xiao-Liang Qi, Xi Dai, Zhong Fang, and Shou-Cheng Zhang. Topological insulators in Bi_2Se_3, Bi_2Te_3 and Sb_2Te_3 with a single Dirac cone on the surface. *Nature Physics*, 5(6): 438–442, June 2009. doi:10.1038/nphys1270.

[106] Y. L. Chen, James G. Analytis, J.-H. Chu, Z. K. Liu, S.-K. Mo, Xiao-Liang Qi, H. J. Zhang, D. H. Lu, Xi Dai, Zhong Fang, S.-C. Zhang, Ian R. Fisher, Z. Hussain, and Z.-X. Shen. Experimental realization of a three-dimensional topological insulator, Bi_2Te_3. *Science*, 325(5937):178–81, July 2009. doi:10.1126/science.1173034.

[107] D. Hsieh, Y. Xia, D. Qian, L. A. Wray, F. Meier, J. H. Dil, J. Osterwalder, L. Patthey, A. V. Fedorov, Hsin Lin, A. Bansil, D. Grauer, Yew San Hor, R. J. Cava, and M. Zahid Hasan. Observation of Time-Reversal-Protected Single-Dirac-Cone Topological-Insulator States in Bi_2Te_3 and Sb_2Te_3. *Physical Review Letters*, 103(14):146401, September 2009. doi:10.1103/PhysRevLett.103.146401.

[108] Zhanybek Alpichshev, James G. Analytis, J.-H. Chu, Ian R. Fisher, Y. L. Chen, Z.-X. Shen, A. Fang, and A. Kapitulnik. STM Imaging of Electronic Waves on the Surface of Bi_2Te_3: Topologically Protected Surface States and Hexagonal Warping Effects. *Physical Review Letters*, 104(1):016401, January 2010. doi:10.1103/PhysRevLett.104.016401.

[109] S. Y. Zhou, G.-H. Gweon, J. Graf, A. V. Fedorov, C. D. Spataru, R. D. Diehl, Y. Kopelevich, D.-H. Lee, Steven G. Louie, and A. Lanzara. First direct observation of Dirac fermions in graphite. *Nature Physics*, 2(9):595–599, August 2006. doi:10.1038/nphys393.

[110] Liang Fu. Hexagonal Warping Effects in the Surface States of the Topological Insulator Bi_2Te_3. *Physical Review Letters*, 103(26):266801, December 2009. doi:10.1103/PhysRevLett.103.266801.

[111] Y. Wang, D. Hsieh, D. Pilon, L. Fu, D. R. Gardner, Y. S. Lee, and N. Gedik. Observation of a Warped Helical Spin Texture in Bi_2Se_3 from Circular Dichroism Angle-Resolved Photoemission Spectroscopy. *Physical Review Letters*, 107(20):207602, November 2011. doi:10.1103/PhysRevLett.107.207602.

[112] K. Kuroda, M. Arita, K. Miyamoto, M. Ye, J. Jiang, A. Kimura, E. Krasovskii, E. Chulkov, H. Iwasawa, T. Okuda, K. Shimada, Y. Ueda, H. Namatame, and M. Taniguchi. Hexagonally Deformed Fermi Surface of the 3D Topological Insulator Bi_2Se_3. *Physical Review Letters*, 105(7):076802, August 2010. doi:10.1103/PhysRevLett.105.076802.

[113] Emmanuel I. Rashba. Properties of semiconductors with an extremum loop: 1. Cyclotron and combinational resonance in a magnetic field perpendicular to the plane of the loop. *Soviet Physics, Solid State*, 2(6):1109–1122, 1960.

[114] S. LaShell, B. A. McDougall, and E. Jensen. Spin Splitting of an Au(111) Surface State Band Observed with Angle Resolved Photoelectron Spectroscopy. *Physical Review Letters*, 77(16):3419–3422, October 1996.

[115] David Hsieh. *Spin-resolved spectroscopic studies of topologically ordered materials*. Phd, Princeton University, 2009.

[116] James G. Analytis, Ross D. McDonald, Scott C. Riggs, Jiun-Haw Chu, G. S. Boebinger, and Ian R. Fisher. Two-dimensional surface state in the quantum limit of a topological insulator. *Nature Physics*, 6(12):960–964, November 2010. doi:10.1038/nphys1861.

[117] Dong-Xia Qu, Y. S. Hor, Jun Xiong, R. J. Cava, and N. P. Ong. Quantum Oscillations and Hall Anomaly of Surface States in the Topological Insulator Bi_2Te_3. *Science*, 821(5993):821–824, July 2010. doi:10.1126/science.1189792.

[118] J. G. Checkelsky, Y. S. Hor, R. J. Cava, and N. P. Ong. Bulk Band Gap and Surface State Conduction Observed in Voltage-Tuned Crystals of the Topological Insulator Bi_2Se_3. *Physical Review Letters*, 106 (19):196801, May 2011. doi:10.1103/PhysRevLett.106.196801.

[119] J. G. Checkelsky, Y. S. Hor, M.-H. Liu, D.-X. Qu, R. J. Cava, and N. P. Ong. Quantum Interference in Macroscopic Crystals of Nonmetallic Bi_2Se_3. *Physical Review Letters*, 103(24):246601, December 2009. doi:10.1103/PhysRevLett.103.246601.

[120] J. W. McIver, D. Hsieh, H. Steinberg, P. Jarillo-Herrero, and N. Gedik. Control over topological insulator photocurrents with light polarization. *Nature Nanotechnology*, 7(2):96–100, January 2011. doi:10.1038/nnano.2011.214.

[121] Chris Jozwiak, Cheol-hwan Park, Kenneth Gotlieb, Choongyu Hwang, Dung-hai Lee, Steven G. Louie, Jonathan D. Denlinger, Costel R. Rotundu, Robert J. Birgeneau, Zahid Hussain, and Alessandra Lanzara. Photoelectron spin-flipping and texture manipulation in a topological insulator. *Nature Physics*, (Advanced Online Publication):1–6, March 2013. doi:10.1038/nphys2572.

[122] Ke He, Yi Zhang, Cui-Zu Chang, Can-Li Song, Li-li Wang, Xi Chen, Jin-Feng Jia, Zhong Fang, Xi Dai, Wen-Yu Shan, Shun-Qing Shen, Qian Niu, Xiao-Liang Qi, Shou-Cheng Zhang, Xu-Cun Ma, and Qi-Kun Xue. Crossover of the three-dimensional topological insulator Bi_2Se_3 to the two-dimensional limit. *Nature Physics*, 6(8):584–588, June 2010. doi:10.1038/nphys1689.

[123] Yeping Jiang, Yilin Wang, Mu Chen, Zhi Li, Canli Song, Ke He, Li-Li Wang, Xi Chen, Xu-Cun Ma, and Qi-Kun Xue. Landau Quantization and the Thickness Limit of Topological Insulator Thin Films of Sb_2Te_3. *Physical Review Letters*, 108(1):016401, January 2012. doi:10.1103/PhysRevLett.108.016401.

[124] Minhao Liu, Jinsong Zhang, Cui-zu Chang, Zuocheng Zhang, Xiao Feng, Kang Li, Ke He, Li-li Wang, Xi Chen, Xi Dai, Zhong Fang, Qi-kun Xue, Xucun Ma, and Yayu Wang. Crossover between Weak Antilocalization and Weak Localization in a Magnetically Doped Topological Insulator. *Physical Review Letters*, 108(3):1–5, January 2012. ISSN 0031-9007. doi:10.1103/PhysRevLett.108.036805.

[125] J. Zhang, C.-Z. Chang, P. Tang, Z. Zhang, X. Feng, K. Li, L.-l. Wang, X. Chen, C. Liu, W. Duan, K. He, Q.-K. Xue, X. Ma, and Y. Wang. Topology-Driven Magnetic Quantum Phase Transition in Topological Insulators. *Science*, 339(6127):1582–1586, March 2013. doi:10.1126/science.1230905.

[126] Cui-Zu Chang, Jinsong Zhang, Xiao Feng, Jie Shen, Zuocheng Zhang, Minghua Guo, Kang Li, Yunbo Ou, Pang Wei, Li-Li Wang, Zhong-Qing Ji, Yang Feng, Shuaihua Ji, Xi Chen, Jinfeng Jia, Xi Dai, Zhong Fang, Shou-Cheng Zhang, Ke He, Yayu Wang, Li Lu, Xu-Cun Ma, and Qi-Kun Xue. Experimental observation of the quantum anomalous Hall effect in a magnetic topological insulator. *Science*, 340 (6129):167–70, April 2013. doi:10.1126/science.1234414.

[127] P. D. C. King, R. Hatch, M. Bianchi, R. Ovsyannikov, C. Lupulescu, G. Landolt, B. Slomski, J. Dil, D. Guan, J. Mi, E. Rienks, J. Fink, A. Lindblad, S. Svensson, S. Bao, G. Balakrishnan, B. Iversen, J. Osterwalder, W. Eberhardt, F. Baumberger, and Ph. Hofmann. Large Tunable Rashba Spin Splitting of a Two-Dimensional Electron Gas in Bi_2Se_3. *Physical Review Letters*, 107(9):096802, August 2011. doi:10.1103/PhysRevLett.107.096802.

[128] Z.-H. Zhu, G Levy, B Ludbrook, C. Veenstra, J. Rosen, R. Comin, D Wong, P Dosanjh, A Ubaldini, P Syers, N. P. Butch, J Paglione, I. Elfimov, and A Damascelli. Rashba Spin-Splitting Control at

the Surface of the Topological Insulator Bi_2Se_3. *Physical Review Letters*, 107(18):1–5, October 2011. doi:10.1103/PhysRevLett.107.186405.

[129] Marco Bianchi, Dandan Guan, Shining Bao, Jianli Mi, Bo Brummerstedt Iversen, Philip D. C. King, and Philip Hofmann. Coexistence of the topological state and a two-dimensional electron gas on the surface of Bi_2Se_3. *Nature Communications*, 1(8):128, January 2010. doi:10.1038/ncomms1131.

[130] M. S. Bahramy, P. D. C King, A. de la Torre, J. Chang, M. Shi, L. Patthey, G. Balakrishnan, Ph. Hofmann, R. Arita, N. Nagaosa, and F. Baumberger. Emergent quantum confinement at topological insulator surfaces. *Nature Communications*, 3:1159, October 2012. doi:10.1038/ncomms2162.

[131] Shuang Jia, Haim Beidenkopf, Ilya Drozdov, M. Fuccillo, Jungpil Seo, Jun Xiong, N. Ong, Ali Yazdani, and R. Cava. Defects and high bulk resistivities in the Bi-rich tetradymite topological insulator $Bi_{2+x}Te_{2-x}Se$. *Physical Review B*, 86(16):165119, October 2012. doi:10.1103/PhysRevB.86.165119.

[132] T. Arakane, T. Sato, S. Souma, K. Kosaka, K. Nakayama, M. Komatsu, T. Takahashi, Zhi Ren, Kouji Segawa, and Yoichi Ando. Tunable Dirac cone in the topological insulator $Bi_{2-x}Sb_xTe_{3-y}Se_y$. *Nature Communications*, 3:636, January 2012. doi:10.1038/ncomms1639.

[133] Sunghun Kim, M. Ye, K. Kuroda, Y. Yamada, E. Krasovskii, E. Chulkov, K. Miyamoto, M. Nakatake, T. Okuda, Y. Ueda, K. Shimada, H. Namatame, M. Taniguchi, and A. Kimura. Surface Scattering via Bulk Continuum States in the 3D Topological Insulator Bi_2Se_3. *Physical Review Letters*, 107(5):056803, July 2011. doi:10.1103/PhysRevLett.107.056803.

[134] Yeping Jiang, Y. Sun, Mu Chen, Yilin Wang, Zhi Li, Canli Song, Ke He, Lili Wang, Xi Chen, Qi-Kun Xue, Xucun Ma, and S. Zhang. Fermi-Level Tuning of Epitaxial Sb_2Te_3 Thin Films on Graphene by Regulating Intrinsic Defects and Substrate Transfer Doping. *Physical Review Letters*, 108(6):066809, February 2012. doi:10.1103/PhysRevLett.108.066809.

[135] Jungpil Seo, Pedram Roushan, Haim Beidenkopf, Yew San Hor, R. J. Cava, and Ali Yazdani. Transmission of topological surface states through surface barriers. *Nature*, 466(7304):343–346, July 2010. doi:10.1038/nature09189.

[136] D. Hsieh, L. A. Wray, D. Qian, Y. Xia, J. H. Dil, F. Meier, L. Patthey, J. Osterwalder, G. Bihlmayer, Yew San Hor, R. J. Cava, and M. Zahid Hasan. Direct observation of spin-polarized surface states in the parent compound of a topological insulator using spin- and angle-resolved photoemission spectroscopy in a Mott-polarimetry mode. *New Journal of Physics*, 12(12):125001, December 2010. doi:10.1088/1367-2630/12/12/125001.

[137] Peng Cheng, Canli Song, Tong Zhang, Yanyi Zhang, Yilin Wang, Jin-Feng Jia, Jing Wang, Yayu Wang, Bang-Fen Zhu, Xi Chen, Xu-Cun Ma, Ke He, Li-Li Wang, Xi Dai, Zhong Fang, Xincheng Xie, Xiao-Liang Qi, Chao-Xing Liu, Shou-Cheng Zhang, and Qi-Kun Xue. Landau Quantization of Topological Surface States in Bi_2Se_3. *Physical Review Letters*, 105(7):076801, August 2010. doi:10.1103/PhysRevLett.105.076801.

[138] K. K. Gomes, Wonhee Ko, Warren Mar, Y. L. Chen, Z.-X. Shen, and H. C. Manoharan. Quantum Imaging of Topologically Unpaired Spin-Polarized Dirac Fermions. *Arxiv Preprint*, arXiv:0909.0921, September 2009.

[139] Rudro R. Biswas and Alexander V. Balatsky. Quasiparticle interference and Landau level spectroscopy in graphene in the presence of a strong magnetic field. *Physical Review B*, 80(8):081412, August 2009. doi:10.1103/PhysRevB.80.081412.

[140] John Schliemann, J. Carlos Egues, and Daniel Loss. Variational study of the ν=1 quantum Hall ferromagnet in the presence of spin-orbit interaction. *Physical Review B*, 67(8):085302, February 2003. doi:10.1103/PhysRevB.67.085302.

[141] M. Zarea and S. E. Ulloa. Landau level mixing by full spin-orbit interactions. *Physical Review B*, 72(8): 085342, August 2005. doi:10.1103/PhysRevB.72.085342.

[142] T. Sato, Kouji Segawa, K. Kosaka, S. Souma, K. Nakayama, K. Eto, T. Minami, Yoichi Ando, and T. Takahashi. Unexpected mass acquisition of Dirac fermions at the quantum phase transition of a topological insulator. *Nature Physics*, 7(8):840–844, August 2011. doi:10.1038/nphys2058.

[143] Lin Miao, Z. F. Wang, Wenmei Ming, Meng-yu Yao, Meixiao Wang, Fang Yang, Y. R. Song, Fengfeng Zhu, Alexei V. Fedorov, Z. Sun, C. L. Gao, Canhua Liu, Qi-Kun Xue, Chao-Xing Liu, Feng Liu, Dong Qian, and Jin-Feng Jia. Quasiparticle dynamics in reshaped helical Dirac cone of topological insulators. *Proceedings of the National Academy of Sciences*, 110(8):2758–62, February 2013. doi:10.1073/pnas.1218104110.

[144] Subir Sachdev. Quantum Criticality: Competing Ground States in Low Dimensions. *Science*, 288 (5465):475–480, April 2000. doi:10.1126/science.288.5465.475.

[145] M. R. Norman, D. Pines, and C. Kallin. The pseudogap: friend or foe of high T_c? *Advances in Physics*, 54(8):715–733, December 2005. doi:10.1080/00018730500459906.

[146] David C. Johnston. The puzzle of high temperature superconductivity in layered iron pnictides and chalcogenides. *Advances in Physics*, 59(6):803–1061, November 2010. doi:10.1080/00018732.2010.513480.

[147] D. Jérome and H. J. Schulz. Organic conductors and superconductors. *Advances in Physics*, 51(1): 293–479, January 2002. doi:10.1080/00018730110116362.

[148] S. A. Kivelson, I. P. Bindloss, V. Oganesyan, J. M. Tranquada, A. Kapitulnik, and C. Howald. How to detect fluctuating stripes in the high-temperature superconductors. *Reviews of Modern Physics*, 75(4): 1201–1241, October 2003. doi:10.1103/RevModPhys.75.1201.

[149] M. D. Johannes, I. I. Mazin, and C. A. Howells. Fermi-surface nesting and the origin of the charge-density wave in $NbSe_2$. *Physical Review B*, 73(20):205102, May 2006. doi:10.1103/PhysRevB.73.205102.

[150] Patrick A. Lee. *Lecture Notes on the Theory of Solids*. Massachusetts Institute of Technology, 2007-08.

[151] George Grüner. *Density Waves in Solids*. Westview Press, 2000. ISBN 0738203041.

[152] Charles Kittel. *Introduction to Solid State Physics*. Wiley, 8 edition, November 2004. ISBN 047141526X.

[153] G. Grüner. The dynamics of charge-density waves. *Reviews of Modern Physics*, 60(4):1129–1181, October 1988. ISSN 0034-6861. doi:10.1103/RevModPhys.60.1129.

[154] J. A. Wilson, F. J. Di Salvo, and S. Mahajan. Charge-density waves and superlattices in the metallic layered transition metal dichalcogenides. *Advances in Physics*, 50(8):1171–1248, December 2001. doi:10.1080/00018730110102718.

[155] N. Ru, C. L. Condron, G. Y. Margulis, K. Y. Shin, J. Laverock, S. B. Dugdale, M. F. Toney, and I. R. Fisher. Effect of chemical pressure on the charge density wave transition in rare-earth tritellurides RTe$_3$. *Physical Review B*, 77(3):035114, January 2008. doi:10.1103/PhysRevB.77.035114.

[156] W. D. Wise, M. C. Boyer, Kamalesh Chatterjee, Takeshi Kondo, T. Takeuchi, H. Ikuta, Yayu Wang, and E. W. Hudson. Charge-density-wave origin of cuprate checkerboard visualized by scanning tunnelling microscopy. *Nature Physics*, 4(9):696–699, July 2008. doi:10.1038/nphys1021.

[157] F. Weber, S. Rosenkranz, J.-P. Castellan, R. Osborn, R. Hott, R. Heid, K.-P. Bohnen, T. Egami, A. Said, and D. Reznik. Extended Phonon Collapse and the Origin of the Charge-Density Wave in 2H-NbSe$_2$. *Physical Review Letters*, 107(10):107403, September 2011. doi:10.1103/PhysRevLett.107.107403.

[158] S.-K. Chan and V. Heine. Spin density wave and soft phonon mode from nesting Fermi surfaces. *Journal of Physics F: Metal Physics*, 3(4):795–809, April 1973. doi:10.1088/0305-4608/3/4/022.

[159] D. E. Moncton, J. D. Axe, and F. J. DiSalvo. Study of Superlattice Formation in 2H-NbSe$_2$ and 2H-TaSe$_2$ by Neutron Scattering. *Physical Review Letters*, 34(12):734–737, March 1975. doi:10.1103/PhysRevLett.34.734.

[160] H. Suderow, V. G. Tissen, J. P. Brison, J. L. Martínez, and S. Vieira. Pressure Induced Effects on the Fermi Surface of Superconducting 2H-NbSe$_2$. *Physical Review Letters*, 95(11):117006, September 2005. doi:10.1103/PhysRevLett.95.117006.

[161] T. Kiss, T. Yokoya, A. Chainani, S. Shin, T. Hanaguri, M. Nohara, and H. Takagi. Charge-order-maximized momentum-dependent superconductivity. *Nature Physics*, 3(10):720–725, August 2007. doi:10.1038/nphys699.

[162] Yejun Feng, Jiyang Wang, R. Jaramillo, Jasper van Wezel, S. Haravifard, G. Srajer, Y. Liu, Z. A. Xu, P. B. Littlewood, and T. F. Rosenbaum. Order parameter fluctuations at a buried quantum critical point. *Proceedings of the National Academy of Sciences*, 109(19):7224, April 2012. doi:10.1073/pnas.1202434109.

[163] Eric W. Hudson. *Investigating High-T_c Superconductivity on the Atomic Scale by Scanning Tunneling Microscopy*. Phd, University of California at Berkeley, 1999.

[164] T. Yokoya, T. Kiss, A. Chainani, S. Shin, M. Nohara, and H. Takagi. Fermi surface sheet-dependent superconductivity in 2H-NbSe$_2$. *Science*, 294(5551):2518–20, December 2001. doi:10.1126/science.1065068.

[165] D. J. Rahn, S. Hellmann, M. Kalläne, C. Sohrt, T. K. Kim, L. Kipp, and K. Rossnagel. Gaps and kinks in the electronic structure of the superconductor 2H-NbSe$_2$ from angle-resolved photoemission at 1 K. *Physical Review B*, 85(22):224532, June 2012. doi:10.1103/PhysRevB.85.224532.

[166] J.M.E. Harper, T.H. Geballe, and F.J. Di Salvo. Heat capacity of 2H-NbSe$_2$ at the charge density wave transition. *Physics Letters A*, 54(1):27–28, August 1975. doi:10.1016/0375-9601(75)90592-7.

[167] T. M. Rice and G. K. Scott. New Mechanism for a Charge-Density-Wave Instability. *Physical Review Letters*, 35(2):120–123, July 1975. doi:10.1103/PhysRevLett.35.120.

[168] C. M. Varma and A. L. Simons. Strong-Coupling Theory of Charge-Density-Wave Transitions. *Physical Review Letters*, 51(2):138–141, July 1983. doi:10.1103/PhysRevLett.51.138.

[169] Michael Tinkham. *Introduction to Superconductivity*. Dover Publications, 2 edition, June 2004. ISBN 0486435032.

[170] S. V. Borisenko, A. A. Kordyuk, V. B. Zabolotnyy, D. S. Inosov, D. V. Evtushinsky, B. Büchner, A. N. Yaresko, A. Varykhalov, R. Follath, W. Eberhardt, L. Patthey, and H. Berger. Two Energy Gaps and Fermi-Surface "Arcs" in NbSe$_2$. *Physical Review Letters*, 102(16):166402, April 2009. doi:10.1103/PhysRevLett.102.166402.

[171] Aleksej Mialitsin. *Raman scattering from layered superconductors: Effects of charge ordering, two-band superconductivity, and structural disorder*. Phd, Rutgers University, 2010.

[172] Th. Straub, Th. Finteis, R. Claessen, P. Steiner, S. Hüfner, P. Blaha, C. S. Oglesby, and E. Bucher. Charge-Density-Wave Mechanism in $2H$-NbSe$_2$: Photoemission Results. *Physical Review Letters*, 82 (22):4504–4507, May 1999. doi:10.1103/PhysRevLett.82.4504.

[173] D. W. Shen, Y. Zhang, L. X. Yang, J. Wei, H. W. Ou, J. K. Dong, B. P. Xie, C. He, J. F. Zhao, B. Zhou, M. Arita, K. Shimada, H. Namatame, M. Taniguchi, J. Shi, and D.-L. Feng. Primary Role of the Barely Occupied States in the Charge Density Wave Formation of NbSe$_2$. *Physical Review Letters*, 101(22): 226406, November 2008. doi:10.1103/PhysRevLett.101.226406.

[174] W. L. McMillan. Theory of discommensurations and the commensurate-incommensurate charge-density-wave phase transition. *Physical Review B*, 14(4):1496–1502, August 1976. doi:10.1103/PhysRevB.14.1496.

[175] R. V. Coleman, B. Giambattista, P. K. Hansma, A. Johnson, W. W. McNairy, and C. G. Slough. Scanning tunnelling microscopy of charge-density waves in transition metal chalcogenides. *Advances in Physics*, 37(6):559–644, December 1988. ISSN 0001-8732.

[176] Hongjie Dai, Huifen Chen, and Charles M. Lieber. Weak pinning and hexatic order in a doped two-dimensional charge-density-wave system. *Physical Review Letters*, 66(24):3183–3186, June 1991. doi:10.1103/PhysRevLett.66.3183.

[177] Mehran Kardar. *Statistical Physics of Fields*. Cambridge University Press, 1st edition, June 2007. ISBN 052187341X.

[178] Xian-Liang Wu, Peng Zhou, and Charles M. Lieber. Determination of the Local Effect of Impurities on the Charge-Density-Wave Phase in TaS$_2$ by Scanning Tunneling Microscopy. *Physical Review Letters*, 61(22):2604–2607, November 1988. doi:10.1103/PhysRevLett.61.2604.

[179] H. Bando, Y. Miyahara, H. Enomoto, and H. Ozaki. Scanning tunneling microscopy investigations of single-q charge density wave state in hafnium-doped tantalum disulfide. *Surface Science*, 381(2-3): L609–L613, June 1997. doi:10.1016/S0039-6028(97)00082-4.

[180] J. Ishioka, Y. Liu, K. Shimatake, T. Kurosawa, K. Ichimura, Y. Toda, M. Oda, and S. Tanda. Chiral Charge-Density Waves. *Physical Review Letters*, 105(17):176401, October 2010. doi:10.1103/PhysRevLett.105.176401.

[181] I. Guillamón, H. Suderow, J. G. Rodrigo, S. Vieira, P. Rodière, L. Cario, E. Navarro-Moratalla, C. Martí-Gastaldo, and E. Coronado. Chiral charge order in the superconductor $2H$-TaS$_2$. *New Journal of Physics*, 13(10):103020, October 2011. doi:10.1088/1367-2630/13/10/103020.

[182] Hui Wang, Jonghee Lee, Michael Dreyer, and Barry I. Barker. A scanning tunneling microscopy study of a new superstructure around defects created by tip-sample interaction on $2H$-NbSe$_2$. *Journal of Physics: Condensed Matter*, 21(26):265005, July 2009. ISSN 0953-8984.

[183] M. J. Lawler, K. Fujita, Jhinhwan Lee, A. R. Schmidt, Y. Kohsaka, Chung Koo Kim, H. Eisaki, S. Uchida, J. C. Davis, J. P. Sethna, and Eun-Ah Kim. Intra-unit-cell electronic nematicity of the high-T_c copper-oxide pseudogap states. *Nature*, 466(7304):347, July 2010. doi:10.1038/nature09169.

[184] M. H. Hamidian, I. A. Firmo, K. Fujita, S. Mukhopadhyay, J. W. Orenstein, H. Eisaki, S. Uchida, M. J. Lawler, E.-A. Kim, and J. C. Davis. Picometer registration of zinc impurity states in Bi$_2$Sr$_2$CaCu$_2$O$_{8+\delta}$ for phase determination in intra-unit-cell Fourier transform STM. *New Journal of Physics*, 14(5):053017, May 2012. doi:10.1088/1367-2630/14/5/053017.

[185] Tess L. Williams. *Nanoscale Electronic Structure of Cuprate Superconductors Investigated with Scanning Tunneling Spectroscopy*. Phd, Harvard University, 2011.

[186] J. A. Slezak, Jinho Lee, M. Wang, K. McElroy, K. Fujita, B. M. Andersen, P. J. Hirschfeld, H. Eisaki, S. Uchida, and J. C. Davis. Imaging the impact on cuprate superconductivity of varying the inter-atomic distances within individual crystal unit cells. *Proceedings of the National Academy of Sciences*, 105(9):3203, March 2008. doi:10.1073/pnas.0706795105.

[187] Jiun-Haw Chu, James G. Analytis, Kristiaan De Greve, Peter L. McMahon, Zahirul Islam, Yoshihisa Yamamoto, and Ian R. Fisher. In-plane resistivity anisotropy in an underdoped iron arsenide super-conductor. *Science*, 329(5993):824, August 2010. doi:10.1126/science.1190482.

[188] W. L. McMillan. Landau theory of charge-density waves in transition-metal dichalcogenides. *Physical Review B*, 12(4):1187–1196, August 1975. doi:10.1103/PhysRevB.12.1187.

[189] Hong Yao, John A. Robertson, Eun-Ah Kim, and Steven A. Kivelson. Theory of stripes in quasi-two-dimensional rare-earth tellurides. *Physical Review B*, 74(24):245126, December 2006. doi:10.1103/PhysRevB.74.245126.

[190] John A. Robertson, Steven A. Kivelson, Eduardo Fradkin, Alan C. Fang, and Aharon Kapitulnik. Distinguishing patterns of charge order: Stripes or checkerboards. *Physical Review B*, 74(13):134507, October 2006. doi:10.1103/PhysRevB.74.134507.

[191] Adrian Del Maestro, Bernd Rosenow, and Subir Sachdev. From stripe to checkerboard ordering of charge-density waves on the square lattice in the presence of quenched disorder. *Physical Review B*, 74(2):024520, July 2006. doi:10.1103/PhysRevB.74.024520.

[192] Colin V. Parker, Pegor Aynajian, Eduardo H. da Silva Neto, Aakash Pushp, Shimpei Ono, Jinsheng Wen, Zhijun Xu, Genda Gu, and Ali Yazdani. Fluctuating stripes at the onset of the pseudo-gap in the high-T_c superconductor $Bi_2Sr_2CaCu_2O_{8+x}$. *Nature*, 468(7324):677–680, December 2010. doi:10.1038/nature09597.

[193] Ilija Zeljkovic, Zhijun Xu, Jinsheng Wen, Genda Gu, Robert S. Markiewicz, and Jennifer E. Hoffman. Imaging the Impact of Single Oxygen Atoms on Superconducting $Bi_{2+y}Sr_{2-y}CaCu_2O_{8+x}$. *Science*, 337(6092):320–323, July 2012. doi:10.1126/science.1218648.

[194] S. R. Saha, N. P. Butch, T. Drye, J. Magill, S. Ziemak, K. Kirshenbaum, P. Y. Zavalij, J. W. Lynn, and J. Paglione. Structural collapse and superconductivity in rare-earth-doped $CaFe_2As_2$. *Physical Review B*, 85(2):024525, January 2012. ISSN 1098-0121. doi:10.1103/PhysRevB.85.024525.

[195] Qing-Yan Wang, Zhi Li, Wen-Hao Zhang, Zuo-Cheng Zhang, Jin-Song Zhang, Wei Li, Hao Ding, Yun-Bo Ou, Peng Deng, Kai Chang, Jing Wen, Can-Li Song, Ke He, Jin-Feng Jia, Shuai-Hua Ji, Ya-Yu Wang, Li-Li Wang, Xi Chen, Xu-Cun Ma, and Qi-Kun Xue. Interface-Induced High-Temperature Superconductivity in Single Unit-Cell FeSe Films on $SrTiO_3$. *Chinese Physics Letters*, 29(3):037402, March 2012. doi:10.1088/0256-307X/29/3/037402.

[196] K. Rossnagel, O. Seifarth, L. Kipp, M. Skibowski, D. Voß, P. Krüger, A. Mazur, and J. Pollmann. Fermi surface of $2H$-$NbSe_2$ and its implications on the charge-density-wave mechanism. *Physical Review B*, 64(23):235119, November 2001.

[197] M. R. Norman, A. Kanigel, M. Randeria, U. Chatterjee, and J. C. Campuzano. Modeling the Fermi arc in underdoped cuprates. *Physical Review B*, 76(17):174501, November 2007. doi:10.1103/PhysRevB.76.174501.

[198] J. R. Kirtley, S. Washburn, and D. J. Scalapino. Origin of the linear tunneling conductance background. *Physical Review B*, 45(1):336, January 1992. doi:10.1103/PhysRevB.45.336.

[199] T. Valla, A. V. Fedorov, P. D. Johnson, P.-A. Glans, C. McGuinness, K. Smith, Eva Y. Andrei, and H. Berger. Quasiparticle Spectra, Charge-Density Waves, Superconductivity, and Electron-Phonon Coupling in $2H$-$NbSe_2$. *Physical Review Letters*, 92(8):086401, February 2004. doi:10.1103/PhysRevLett.92.086401.

[200] J. R. Kirtley and D. J. Scalapino. Inelastic-tunneling model for the linear conductance background in the high-T_c superconductors. *Physical Review Letters*, 65(6):798, August 1990. doi:10.1103/PhysRevLett.65.798.

[201] F. C. Niestemski, S. Kunwar, S. Zhou, Shiliang Li, H. Ding, Ziqiang Wang, Pengcheng Dai, and V. Madhavan. A distinct bosonic mode in an electron-doped high-transition-temperature superconductor. *Nature*, 450(7172):1058, December 2007. ISSN 1476-4687. doi:10.1038/nature06430.

[202] I. Fridman, K.-W. Yeh, M.-K. Wu, and J. Y. T. Wei. STM spectroscopy on superconducting $FeSe_{1-x}Te_x$ single crystals at 300 mK. *Journal of Physics and Chemistry of Solids*, 72(5):483, May 2011. doi:10.1016/j.jpcs.2010.10.002.

[203] T. Arai, K. Ichimura, K. Nomura, S. Takasaki, J. Yamada, S. Nakatsuji, and H. Anzai. Tunneling spectroscopy on the organic superconductor κ-$(BEDT$-$TTF)_2Cu(NCS)_2$ using STM. *Physical Review B*, 63(10):104518, February 2001. doi:10.1103/PhysRevB.63.104518.

[204] R. T. Collins, J. Lambe, T. C. McGill, and R. D. Burnham. Inelastic tunneling characteristics of AlAs/GaAs heterojunctions. *Applied Physics Letters*, 44(5):532, 1984. doi:10.1063/1.94828.

[205] W. McMillan and Jack Mochel. Electron Tunneling Experiments on Amorphous $Ge_{1-x}Au_x$. *Physical Review Letters*, 46(8):556, February 1981. doi:10.1103/PhysRevLett.46.556.